Image Enhancement with
Two-Photon Laser Scanning Microscopy

Thesis by

Chun-Ming Wang

In Partial Fulfillment of the Requirements
for the Degree of
Doctor of Philosophy

California Institute of Technology
Pasadena, California

1998
(Submitted May 18, 1998)

ACKNOWLEDGMENTS

These five years at Tech have been the golden years of my life. Not only did I enjoy my time learning science and advanced technology, but also I had a lot of fun investigating new phenomena with knowledgable professionals. Dr. Fraser, my advisor, offered me this great opportunity to work in the Biological Imaging Center and provided numerous suggestions for the investigation methods of my research. His passion for teaching and research were so inspiring that I learned to enjoy the process of scientific investigation. Dr. Wayland, an Emeritus professor in Engineering science, taught me much about tissue optics and brain physiology. Not only did he show me the impact of microscopic investigation, but he also showed me the spirit of scientific persuit and macroscopic concern for science policy.

Dr. S. Potter, a postdoc at the Imaging Center, helped me set up and discussed the means of maintaining our TPLSM. Michael Zeineh, an MD-PhD student at UCLA, wrote the image deconvolution program and helped acquire part of the CLSM images. Dr. M. Kennedy and Dr. Schuman generously provided rat hippocampus double-stained specimens for the experiments of image deconvolution and image degradation. Dr. McGill, Dr. Scherer, and Dr. Quake read the thesis and gave many valuable suggestions. Folks at the biological imaging center provided me many opinions and help. M. Linden-Martiin read my thesis and gave me suggestions about the writing style and grammar. I want to thank all of them for their kind assistance to my thesis work.

Life at Tech would have been much tougher without the support from my family. I want to thank Tseng-Cheng, Tsin-Tsau, May-Hsieh, and Jim-Zen, who always backed me up when I encountered difficulties. And finally, I am grateful that many friends, Chuan-Cheng, Meina, Chao-Ping, Hou-Pu, Chi-Fang, Marina and Tai-Chen, helped me so much all these years in my life. I did enjoy my stay in beautiful Pasadena and hope my work can help improve the advance of science and technology.

ABSTRACT

Although confocal microscopy provides an efficient means of fluorescence imaging, many obstacles including extensive photobleaching and limited penetration depths limit its application. Emergence of two-photon laser scanning microscopy (TPLSM), with limited excitation volume, successfully overcomes those difficulties. Not only is TPLSM shown to have much less photobleaching and better penetration depths than CLSM, but also it is capable of doing UV imaging without using special UV optical elements.

Several different aspects of TPLSM are discussed in the dissertation. The progress of 3-D fluorescence microscopy, a historical retrospective of two-photon excitation, the physics of two-photon excitation and our instrument setupare is discussed in the first chapter. In chapter II, a qualitative and quantitative confirmation of two-photon excitation, optical transfer efficiency, point spread function and resolution, signal-to-noise ratio, and two-photon excitation spectrum are presented. Chapter III shows the comparison between TPLSM and CLSM. Although CLSM has slightly better resolution than TPLSM, TPLSM has much less photobleaching and toxicity, greater penetration depth, less signal cross talk, and better signal collecting efficiency.

Image deconvolution techniques with CLSM and TPLSM are discussed in chapter IV. Using this image processing methods and acquired PSF, we improved the resolution of CLSM and TPLSM dramatically. These deblurring techniques were applied to study the positions of proteins in the pre- and postsynaptic compartments of rat hippocampal culture cells. The improved resolution enabled us to distinguish the positions of Synapsin I, CaM Kinase II, and PSD-95, which could only be done with electron microscopy before.

In chapter V, image degradation due to brain tissue scattering is discussed. Emission signals with long wavelengths were shown to have better resolution and image contrast because of less tissue scattering. This result shows the necessity of designing fluorophores with low emission wavelengths for deep tissue imaging.

TPLSM already provides many insightful images to the study of the dynamics and structures of biological systems. With the advance of technology, applications of TPLSM will be further developed to help understand biological or physical mechanism.

CONTENTS

Acknowledgments

Abstract

CHAPTER I INTRODUCTION

CHAPTER II QUANTITATIVE ANALYSIS OF TWO-PHOTON LASER SCANNING MICROSCOPY

CHAPTER III COMPARISON OF CONFOCAL AND TWO-PHOTON LASER SCANNING MICROSCOPY

CHAPTER IV IMAGE ENHANCEMENT IN CONFOCAL AND TWO-PHOTON MICROSCOPY

CHAPTER VI CONCLUSION

LIST OF FIGURES

LIST OF TABLES

CHAPTER I

INTRODUCTION OF TWO-PHOTON MICROSCOPY

1.1 PROGRESS OF 3-D FLUORESCENCE IMAGING

Optical microscopy, due to its efficient and precise nature, continues to play an important role in biological research. Its importance has been greatly increased with the recent advances of fluorescence microscopy and probes, which can give non-invasive detection of tiny variation or movement of molecules and ions in cells with high resolution. With micro-injection and other loading techniques, researchers can therefore explore dynamic mechanisms of biological systems with minimal damage.

Three-dimensional (3-D) fluorescence imaging, which can provide insight into biological structures and mechanisms with high contrast, is one of the most rapidly growing research fields in the applications of optical imaging. To obtain a good 3-D image reconstruction, a series of 2-D images with minimal out-of-focus signals must be acquired precisely. Wide-field microscopy (WFM) (combined with deconvolution techniques), confocal microscopy, and two-photon microscopy are three 3-D fluorescence imaging methods that are widely used in modern biological research.

Wide field microscopy

WFM uses a conventional epifluorescence microscope to acquire a series of images of adjacent focal planes throughout the volume of interest. When the signals from different focal planes are collected, the in-focus information becomes blurred. By acquiring the point spread function (PSF) of the microscope, most out-of-focus signals can be removed using image deconvolution techniques. One advantage of WFM is that it can utilize dyes whose excitation spectrum lies in the ultraviolet (UV) range. Moreover, it can incorporate a cooled CCD detector to obtain images with high signal-to-noise ratio (SNR). Among the drawbacks is that image deconvolution is a very time-consuming computational technique that greatly slows the biological observation and may limit its application; and the use of extended exposure to UV light may damage the tissue.

Confocal microscopy

In 1957, Marvin Minsky applied for a patent for a stage-scanning confocal microscope, which was far sighted and remarkable for the development of confocal microscopy. In his design the conventional condenser is replaced by a lens identical to to the objective lens, and the field of illumination is limited by a pinhole positioned on the microscope axis. The field of view is restricted by a second pinhole in the image plane set confocally to the illumination spot in the specimen and to the first pinhole. It provides a means of reducing blurring of images from light scattering and improving image resolution and signal-to-noise ratio.

During the early 1970s, Egger and his colleagues developed a laser-illuminated confocal microscope in which the objective lens was oscillated in order to scan the beam over the specimen. In the late 1970s, Sheppard et al. and Wilson et al. described an epi-illuminating confocal microscope of the stage-scanning type, equipped with a laser source and a photomultiplier (PMT) as the detector. Carlsson et al. (1985), Amos et al. (1987) and White et al. (1987) introduced the confocal laser scanning microscope (CLSM) which could acquire images of thin optical-sections in seconds. With its high efficiency and convenience, CLSM has become one of the most powerful optical microscopes in investigating biological structure and systems.

In CLSM, a continuous-wave (CW) laser beam is raster scanned across stained specimens by vibrational mirrors to excite dye molecules, and the fluorescence signals that are generated by the single-photon excitation are focused and collected by a PMT. The small aperture, placed confocally to the illumination spot in the specimen, can reject most of the out-of-focus signals (see Figure 1.1). By moving the stage in the axial direction between the 2-D images, researchers can acquire a series of images and reconstruct 3-D fluorescence images precisely.

Although CLSM has advantages of fast acquisition rates and thin optical sectioning, CLSM has some inherent problems such as photo-bleaching and -toxicity which need to be solved. When continuously illuminated by a laser source, dye molecules may react with oxygen and lose the ability of generating fluorescence, resulting in significant photobleaching. Photo-toxicity, caused by toxic chemicals produced by the interaction between the dye and laser light, can change a cell's vitality or even kill cells and direct exposure to the UV light may damage the cells. Although the confocal pinhole eliminates out-of-focus signals, dye molecules in the out-of-focus regions still absorb laser light and suffer from photobleaching and phototoxicity. When a time-lapse imaging proceeds, images may fade out or cells may be killed and valuable information related to development can be lost.

Good resolution and photo-bleaching are trade-offs in CLSM. Although the aperture in CLSM can improve the image resolution, a high-power laser beam, necessary for obtaining a clear 3-D image with a small aperture (a small pinhole reduces the signal amount), speeds up the photo-bleaching. Like photo-bleaching, photo-toxicity becomes more serious with the high intensity radiation required with a small aperture. Therefore, it is difficult to observe the details of the end of a scanning stack in CLSM.

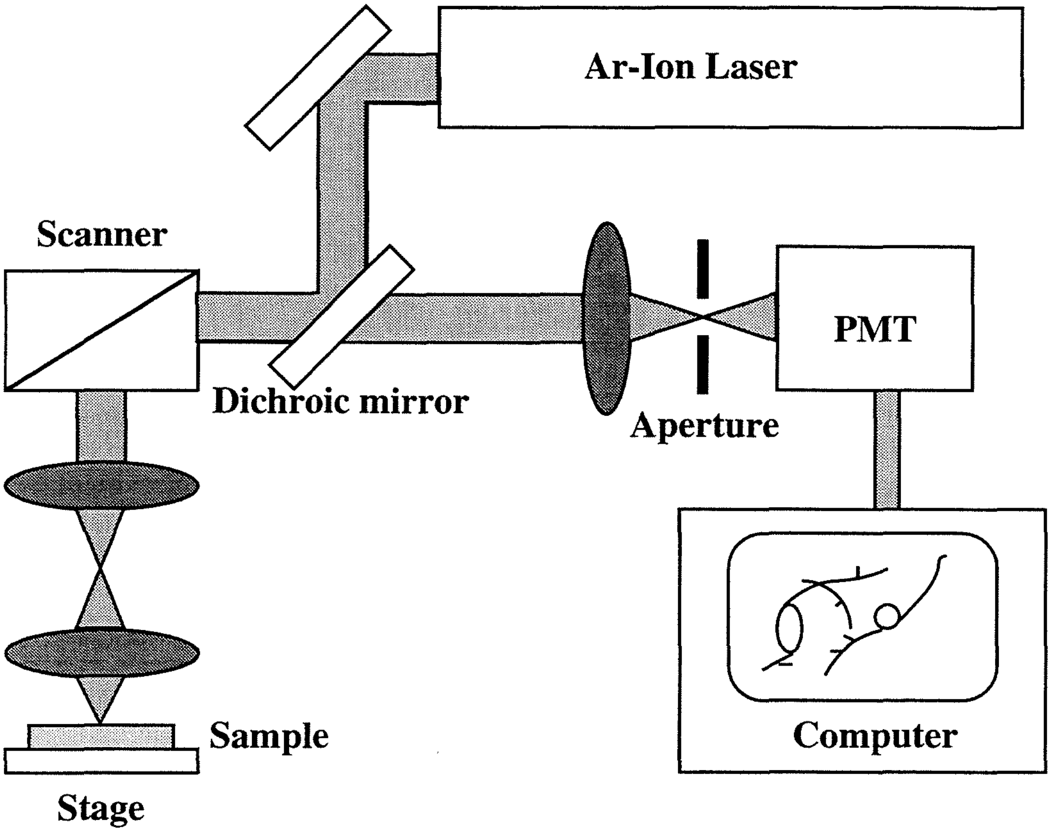

Fig. 1.1 Light path of a CLSM. Most of out-of focus signals are blocked by the aperture, confocal with the objective, and form a thin optical-sectioning image.

Photo-bleaching and -toxicity, which are a significant problem of both WFM and CLSM, can be partially minimized by the addition of free-radical scavengers (Giloh and Sedat, 1982); however, the difference in the image intensity at the beginning and the end of the series is still significant. In 1990, W. Denk et al. used a pumped-dye laser to produce two-photon absorption in a laser scanning microscope. Two-photon laser scanning microscopy (TPLSM), which successfully reduced photo-bleaching and -toxicity problems in CLSM, holds great promises for non-invasive 3-D fluorescence imaging.

1.2 PHYSICS OF TWO-PHOTON EXCITATION

Historical retrospect

In 1931, Maria Goppert-Mayer predicted two-photon excitation as a single quantum event. Simultaneous absorption of two photons causes transition to an excited state of a fluorophore. Since the reaction requires simultaneous absorption of two photons (within nanoseconds), the reaction rate is proportional to the square of the instantaneous intensity of the light source. Because two-photon absorption requires high excitation intensity, it was not observed until 30 years later when the laser was invented.

Mechanism of one-photon and two-photon excitation

A fluorophore can be stimulated to an excited state in three ways. In CLSM, it may absorb one photon and transit to an excited state, relax to a lower state, emit fluorescence, and then relax to the ground state. Another way to reach an excited state is to absorb several photons sequentially, gradually going through a series of intermediate states. On the other hand, A dye molecule may absorb photons simultaneously and jump to a higher state in a single step without going through the intermediate states (See Fig. 1.2). For example, a fluorescein molecule can absorb one Ar laser 488 nm photon and emit fluorescence. Or it can absorb two infrared photons to reach the excited state. Sequential absorption requires a resonance match of the light frequencies and state lifetime in each absorption process, while simultaneous absorption does not. In TPLSM, the simultaneous absorption mechanism is utilized because it can be achieved with an ultrashort pulse laser regardless of the band structure of the dye molecules.

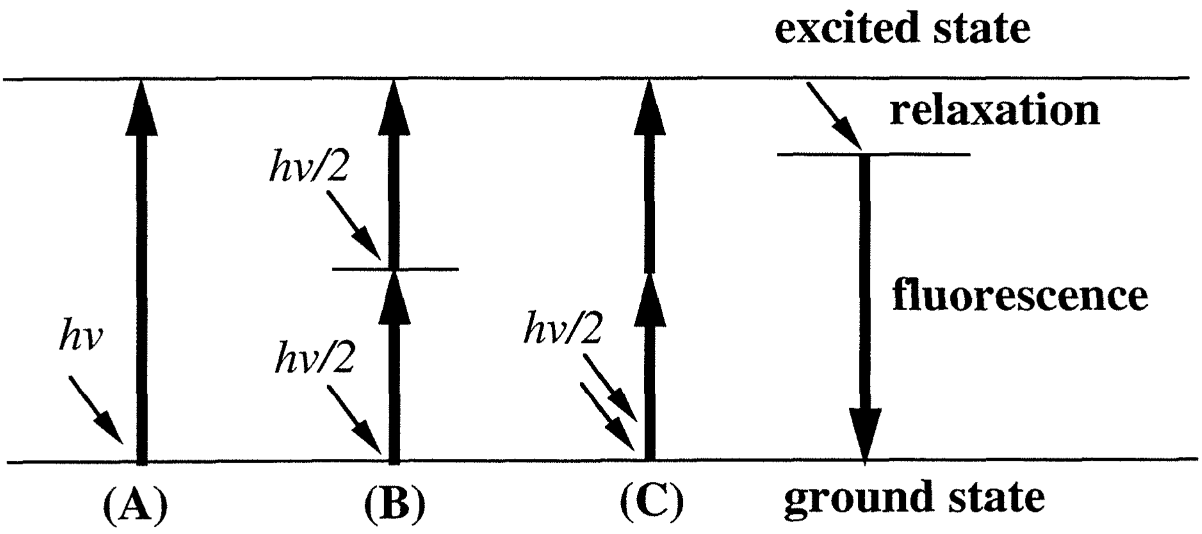

Fig. 1.2 Three ways of optical absorption. (A) One-photon absorption, used in CLSM. (B) Sequential two-photon absorption, where there is a state in the middle. (C) Simultaneous two-photon absorption, used in TPLSM.

The two-photon excitation used in TPLSM is the simultaneous absorption of two identical photons with wavelength λ, resulting in the transition to the excited state with energy 2hc/λ. Most of the dyes that are used as biological probes have either a visible or UV absorption spectrum, so they can be excited by the simultaneous absorption of two infrared photons. However, simultaneous two-photon absorption requires a laser beam with high spatial and temporal intensity. A high spatial intensity can be obtained by focusing a laser beam to a diffraction-limited spot with a high-NA objective. To achieve a high instantaneous intensity, an ultra-short pulse laser is necessary in TPLSM because the low cross section of two-photon excitation. Research indicates that maximum fluorescence generation requires a pulse laser with pulse duration in the magnitude of the lifetime of the excited state, which is about a few nanoseconds for many of the biological fluorophores. Repetition rates of about 100 MHz (one pulse every 10 ns), as are common in the available mode-lock lasers that provide ultrashort pulses, are almost perfect for TPLSM.

For a fluorophore at the center of the focus, the probability n_a of two-photon absorption during a single pulse using a pulse laser with wavelength λ, average power P, repetition rate f, pulse width τ, and an objective with numerical aperture A (Denk et al., 1990) can, using the paraxial approximation, be estimated as:

$$n_a \approx \frac{\delta P^2}{\tau f^2}\left(\frac{\pi A^2}{hc\lambda}\right)^2$$

which depends on the two-photon cross section δ, typically of the order of 10^{-50} to 10^{-49} cm^4 s/photon/molecule, and quadratically on the laser average power p.

The formula is, however, only correct for a low excitation probability n_i. The reason is that during the pulse, 100 fs pulse length for a typical excited-state lifetime in the nanosecond range, the molecules don't have sufficient time to relax to the ground state. Then the saturation effect starts to occur when n_i approaches unity. Several tens of miliwatts in a strongly focused beam with 100 fs pulse length can result in saturation.

1.3 INSTRUMENTATION

Illumination sources of two-photon imaging

The first two-photon laser scanning microscope (Denk et al., 1990) was set up with a colliding-pulse mode-lock laser, which provides 15 mW average power of 630 nm light in 100 fs pulses at 100 MHz (Valdemanis and Fork, 1986). This instrument suffers from limited tunability and poor photochemical stability of the absorber dye solution. One other method to produce two-photon excitation is to use a hybrid mode-lock dye laser, which uses an active mode-locked argon-ion or a frequency-doubled neodymium:YAG laser to pump a dye laser. Unfortunately, this system is very expensive and hard to operate.

Modification of Sarastro 2000

In our system, an 8W argon laser (Innova 310, Coherent) pumps a Titanium-Sapphire laser (Mira 900, Coherent) to produce an infrared laser beam (See Fig. 1.3). Via passive mode-locking, the output laser beam becomes a 200-femtosecond pulse train with fifty kW peak power and 500 mW average power, and enters a modified confocal microscope (Sarastro 2000, Molecular Dynamics). With such ultra-high peak-power illumination, this microscope has strong dual-photon excitation and clear fluorescence images. A 690-nm short-pass dichroic mirror replaced the original dichroic mirror in Sarastro 2000 to reflect the infrared laser beam and pass the visible fluorescence, thus generating images with the best SNR. A short pass filter (BG39, Omega) was placed in front of the PMT to block scattered laser beams and possible one-photon fluorescence.

Because TPLSM uses an ultrashort pulse laser source which spans quite a range of wavelengths, it is important to discuss the group velocity dispersion (GVD), a phenomena in which different wavelengths travel at different velocities. For a Gaussian pulses, the relationship between the pulse width τ and the wavelength spread $\Delta\lambda$ is:

$$\Delta\lambda = \frac{2(\ln\ 2)\lambda_c^2}{\pi c \tau}$$

where c is the speed of light and λ_c is the laser center wavelength. For example, a 200 fs pulse at 850 nm will have 5.3 nm wavelength spread. GVD results in a various arrival time for different wavelengths in one pulse in most optical material, namely group delay dispersion (GDD). GDD reduces the peak intensity of the pulse, which decreases the probability of two-photon excitation. GDD can be partially compensated by "pre-chirping" the pulse, which is achieved using a prism in the Mira 900, so as to bring blue and red ends of a pulse on the focal plane.

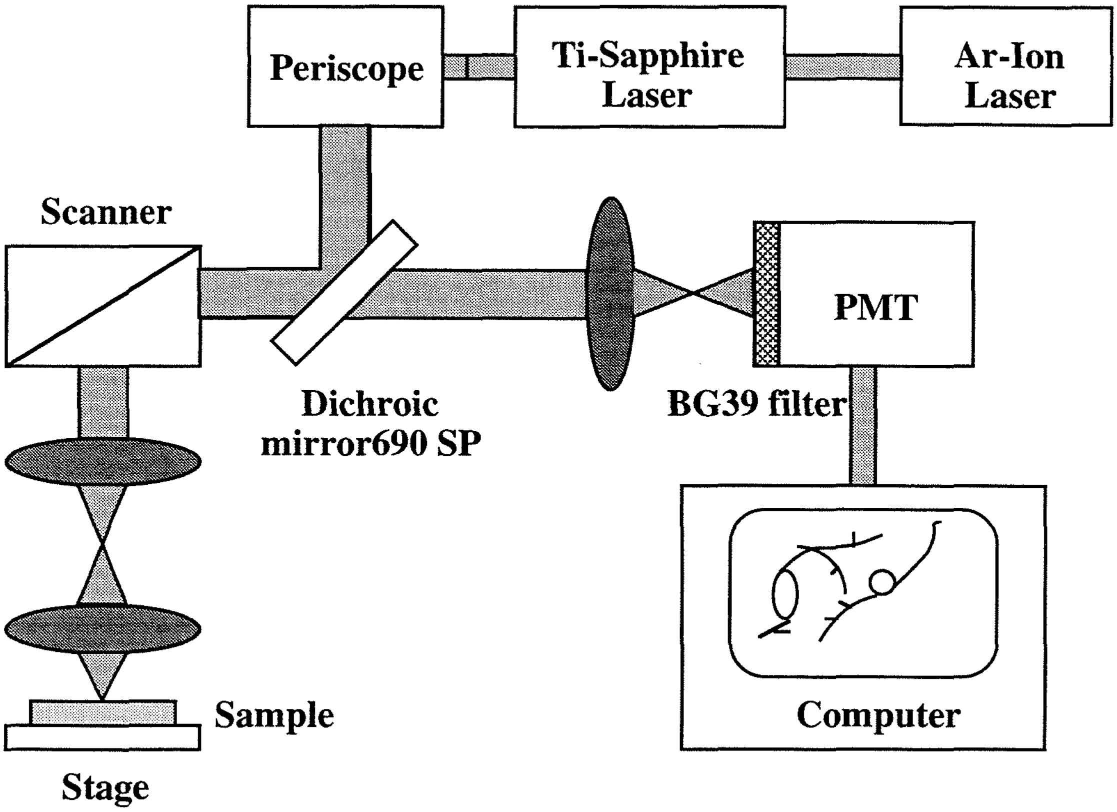

Fig. 1.3 A schematic plot of our two-photon laser scanning microscope. PMT denotes photomultiplier. The BG39 filter is a short pass filter from Omega. The 690 SP is a custom-made short-pass dichroic mirror.

Because two-photon absorption depends quadratically on excitation intensity, which is proportional to the peak power of the pulse and thus inverse proportional to the pulse duration, the measurements of the pulse widths become crucial in determining the excitation intensity in TPLSM. To measure the pulse width of our Ti-Sapphire output beam, a fraction of the output was directed into an autocorrelator (Inrad 5-14). A femto-delay glass block and a second-harmonic-generation (SHG) crystal were put in the autocorrelator to produce an autocorrelation trace. To acquire a correct pulse width, two reflected beams were centered at the PMT pinhole and had about a 3 mm separation. The autocorrelation trace was measured with an oscilloscope. (Fig. 1.4 and Fig. 1.5)

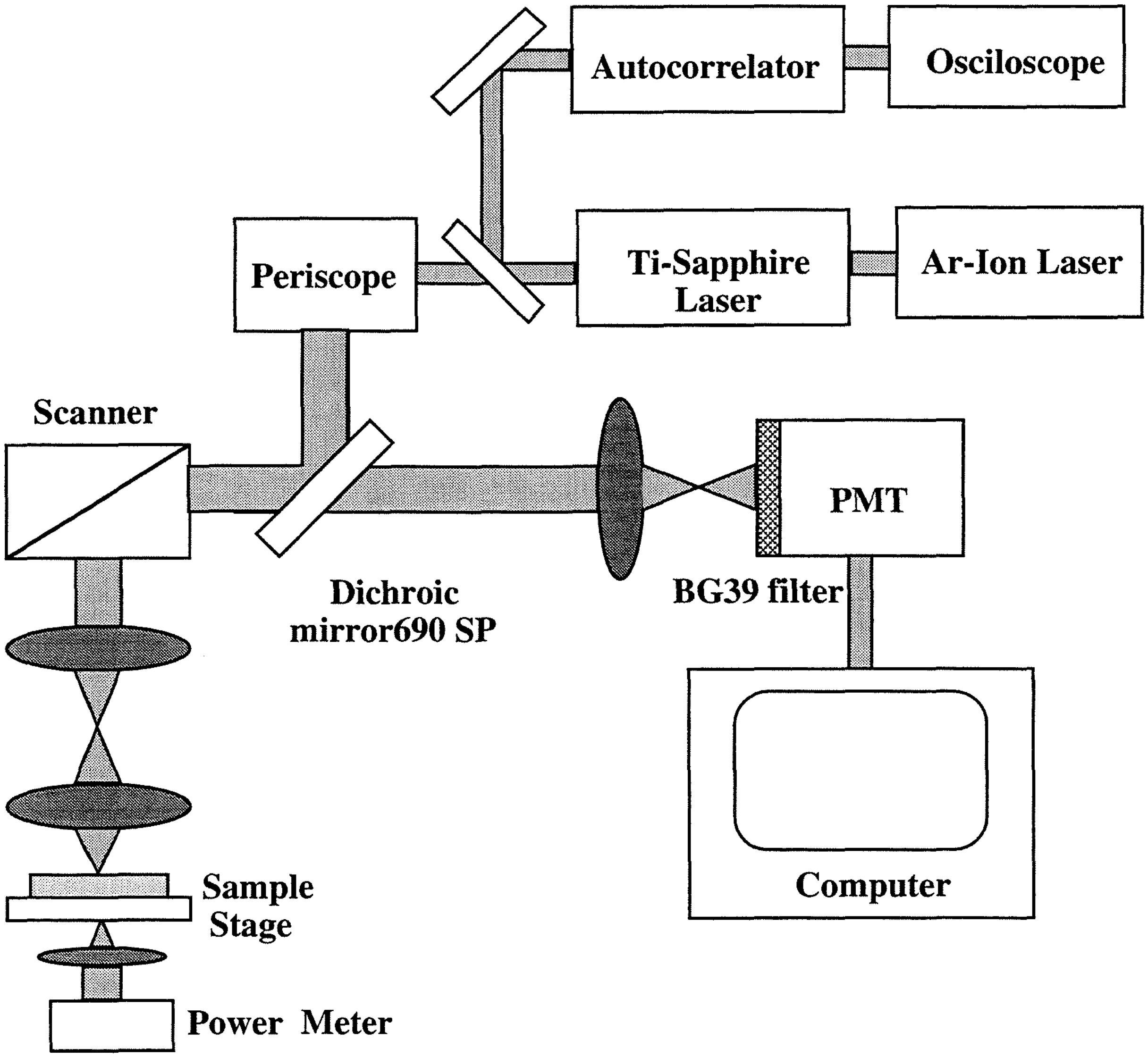

Fig. 1.4 Schematic drawing of the setup of pulse width measurement of two-photon excitation.

SCHEMATIC DRAWING OF 5-14 AUTOCORRELATOR

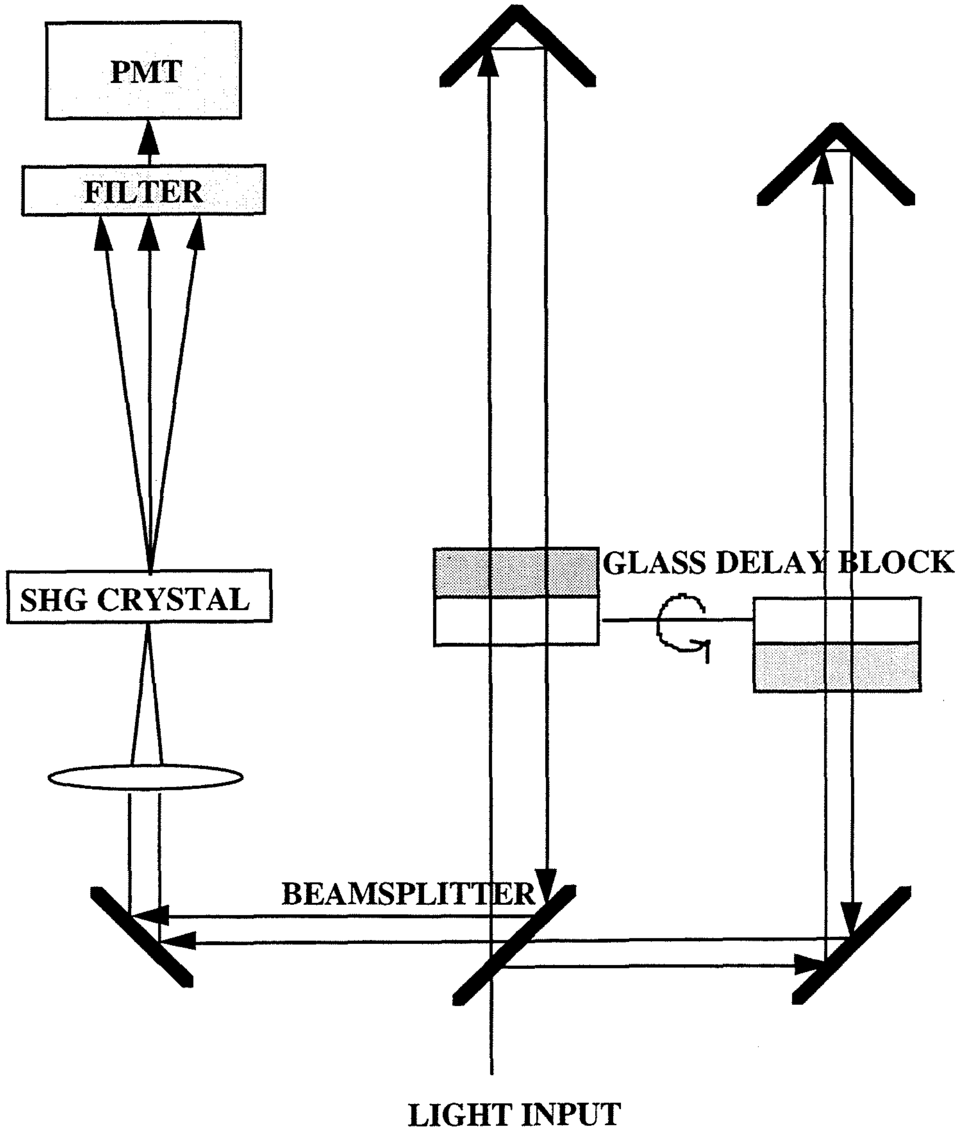

Fig 1.5 Schematic drawing of the 5-14B autocorrelator.

REFERENCES

Amos, W.B., White, J.G., and Fordham, M., 1987, "Use of confocal imaging in the study of biological structures," *Appl.Opt.* **26**:3239-3242

Birge, R.R.,1986, "Two-photon spectroscopy of protein-bound chromophores," *Acc. Chem. Res.*, **19,**138-146

Carlsson, K., Danielsson, P., Lenz, R., Liljeborg, A., Majlof, L., and Aslund, N., 1985, "Three-dimensional microscopy using a confocal laser scanning microscope," *Opt. Lett.* **10**:53-55

Denk, W., Piston, D.W., and Webb, W.W.,1995, "Two-photon molecular excitation in laser-scanning microscopy," in *Handbook of biological confocal microscopy* 2nd edition, Plenum Press, New York. 445-458

Denk, W., Strickler, J.H., and Webb, W.W., 1990, "Two-photon laser scanning fluorescence microscopy," *Science* 248-73

Donald, M. Friedrich, 1982, "Two-photon molecular spectroscopy," *J. of Chemical Education* 472-481

Egger, M.D., 1989, "The development of confocal microscopy," *Trends Neurosci.* 12:11

Giloh, H., and Sedat, J.W., 1982, "Fluorescence microscopy: Reduced photobleaching of rhodamine and fluorescein protein conjugates by n-propy1 gallate,"*Science* **217**:1252-1255

Goppert-Mayer, M., 1931, "Ueber Elementarakte mit zwei Quantenspruengen," *Ann. Phys.* **9**:273

Minsky, M , 1957, U.S. Patent #3013467 Microscopy Apparatus

Sheppard, C.J.R., and Kompfner, R., 1978, "Resonant scanning optical microscope," *Appl. Opt.* **17**(18):2879

So, P.T.C., French, T., Yu, W.M., Berland, K.M., Dong, C.Y., and Gratton E., 1995, "Time-resolved fluorescence microscopy using two-photon excitation," *Bioimaging* **3** 49-63

Valdemanis, J.A., and Fork, R.L., 1986, IEEE J. *Quantum Electron* QE-22:112

White, J.G., Amos. W.B., and Fordham, M., 1987, "An evaluation of confocal versus conventional imaging of biological structures by fluorescence light microscopy," *J. Cell Biol.* **105**:41-48

Wilson, T., and Sheppard, C., 1984, Theory and Practice of Scanning Optical Microscopy, Academic Press, New York

CHAPTER II

QUANTITATIVE ANALYSIS OF TWO-PHOTON LASER SCANNING MICROSCOPY

2.1 INTRODUCTION

The emergence of TPLSM has made possible many biological observations which require low phototoxicity over a long time period. However, the two-photon excitation mechanism, the image quality, and the optimal imaging condition of TPLSM are yet to be fully defined. This chapter presents the quantitative analysis of our two-photon laser scanning microscope (TPLSM). This chapter also presents qualitative and quantitative confirmation of two-photon excitation, optical transfer efficiency, point spread function and resolution, signal-to-noise ratio, and two-photon excitation spectrum. These characteristics were acquired to help understand the two-photon excitation mechanism in biological tissues and to optimize the image quality of our TPLSM.

In section 2.2, Drosophila chromosomes stained with DAPI (4', 6-diamidino 2-phenylindole) were imaged with TPLSM, thus verifying the UV capability of our system. The quantitative mechanism of two-photon excitation was confirmed by plotting the relationship between the excitation and emission intensities of TPLSM. The emission intensity of TPLSM showed quadratic dependence of the excitation intensity indicating that one chromophore needs to simultaneously absorb two near-IR photons to reach excited states.

To minimize saturation, photobleaching and phototoxicity, we found it more effective to optimize the efficiency of detection than that of illumination. In section 2.3, the optical transfer efficiency (OTE) of the detection path is discussed. Some losses are unavoidable losses such as the collection angle and the transmission of the objective lens; other losses, such as the quantum efficiency of the detector, can be improved upon. The overall optical efficiency of our TPLSM is provided and the optimization methods are discussed.

In TPLSM, the probability of two-photon excitation for the in-focus fluorophores is much larger than those of the out-of-focus fluorophores, so it does not require an aperture to achieve optical sectioning for 3-D imaging. Unlike CLSM, the resolution of TPLSM depends only on the illumination wavelengths and the excitation volume, not on the aperture size. Two-photon excitation utilizes double illumination wavelengths and is expected to have a radius of an Airy disc of twice the radius of one-photon excitation. However, the quadratic dependence of two-photon excitation decreases the excitation volume and therefore improves the resolution. The point spread function, a 3-D image of a sub-resolution point source, is an effective representation of the image characteristics of an optical imaging system. Section 2.4 discusses the acquisition of the point spread function of our TPLSM and its resolution.

The overall image quality is usually determined not only by the resolution, but also by the signal-to-noise ratio (SNR) of the images. The bulk of the noise in TPLSM, under real conditions, is shot noise. The electronic noise is shown to be much less than shot noise in the images of TPLSM, so the SNR of TPLSM images is, when the dye molecules are not saturated, approximately proportional to the square root of detected photons. In section 2.5, the measurement of background noise shows averaging can reduce the fluctuation of background but not its mean value. Also the pixel value of the background noise at various PMT voltages (700V-1056V) provides the expected value of electronic noise in our TPLSM images.

2.2 CONFIRMATION OF TWO-PHOTON EXCITATION

QUALITATIVE CONFIRMATION

3-D IMAGES OF DROSOPHILA CHROMOSOMES

A UV-CLSM has many advantages over visible-light CLSM. It is capable of uncaging many fluorophores to observe ion dynamics such as calcium activities. It utilizes a shorter wavelength and therefore provides better resolution. However, UV light is, in general, more harmful to cells and tissue and causes difficulties in imaging biological systems *in vivo* over a long time period. In addition, most glass has strong absorption in the UV light range, so delivering UV illumination is usually less efficient and requires customized optical elements including objectives and beamsplitters.

One of our earliest attempts at using our two-photon fluorescence microscope was to take images of Drosophila chromosomes. DAPI (4', 6-diamidino 2-phenylindole), a commonly used DNA dye, requires excitation at a shorter wavelength (near UV) than is available on an argon or Ar-K laser, which is the most used lasers in confocal laser scanning microscopy (CLSM). Therefore, chromosomes stained with DAPI are, conventionally, imaged with a wide-field fluorescence microscope (WFM) instead of a CLSM. However, a WFM alone lacks the ability to distinguish image depth requiring computational approaches to define the 3-D biological images and to understand the structure. Therefore, TPLSM provides a perfect means of taking 3-D images of chromosomes stained with DAPI. In our system, the wavelength of the Ti-sapphire laser was tuned to 730 nm so that it could be used to excite UV dye molecules like DAPI.

Moreover, many 3-D digital images can be taken because of the optical sectioning capability of TPLSM.

To prepare the specimen for observation, several Drosophila were immersed in a saline solution and then their saliva glands were dissected. The glands were fixed with acetic acid/ETOH (1:3) for five minutes and then rinsed with water. After that they were stained with DAPI (0.1 mg/ml diluted 1:200 with pH 7.5 buffer) and rinsed with water again. The specimen was then immersed in glycerol and mounted on a slide. The images were taken with our TPLSM with a Zeiss 100x objective (oil immersion, NA 1.4).

Fig. 2.1 shows an image of the polytene chromosomes in the Drosophila saliva gland, and reveals the DNA bands of the chromosomes. Because one-photon excitation of DAPI molecules requires an ultraviolet illumination while the image was taken with an infrared illumination, this image shows both the validity of the two-photon excitation of our system and the possible UV application of TPLSM. This result shows that TPLSM can provide an effective means of observing cell chromosomes at various stages. Other UV-excitation observations, such as 3-D imaging of calcium-ion activities (Piston, D.W. et al., 1994) were also made possible with TPLSM without using UV optics.

Fig. 2.1 DAPI-stained chromosome images of Drosophila saliva glands with TPLSM. (A) Overview of gland cells. The arrows point to 3 cell nuclei. (B) The zoom-in view of the nucleus. The arrows point to DNA banding pattern in the polytene chromosomes. This image was taken with a Zeiss 100x objective (oil immersion, NA 1.4).

Fig. 2.1 Two-Photon Images of Chromosome of Drosophila Saliva Gland stained with DAPI

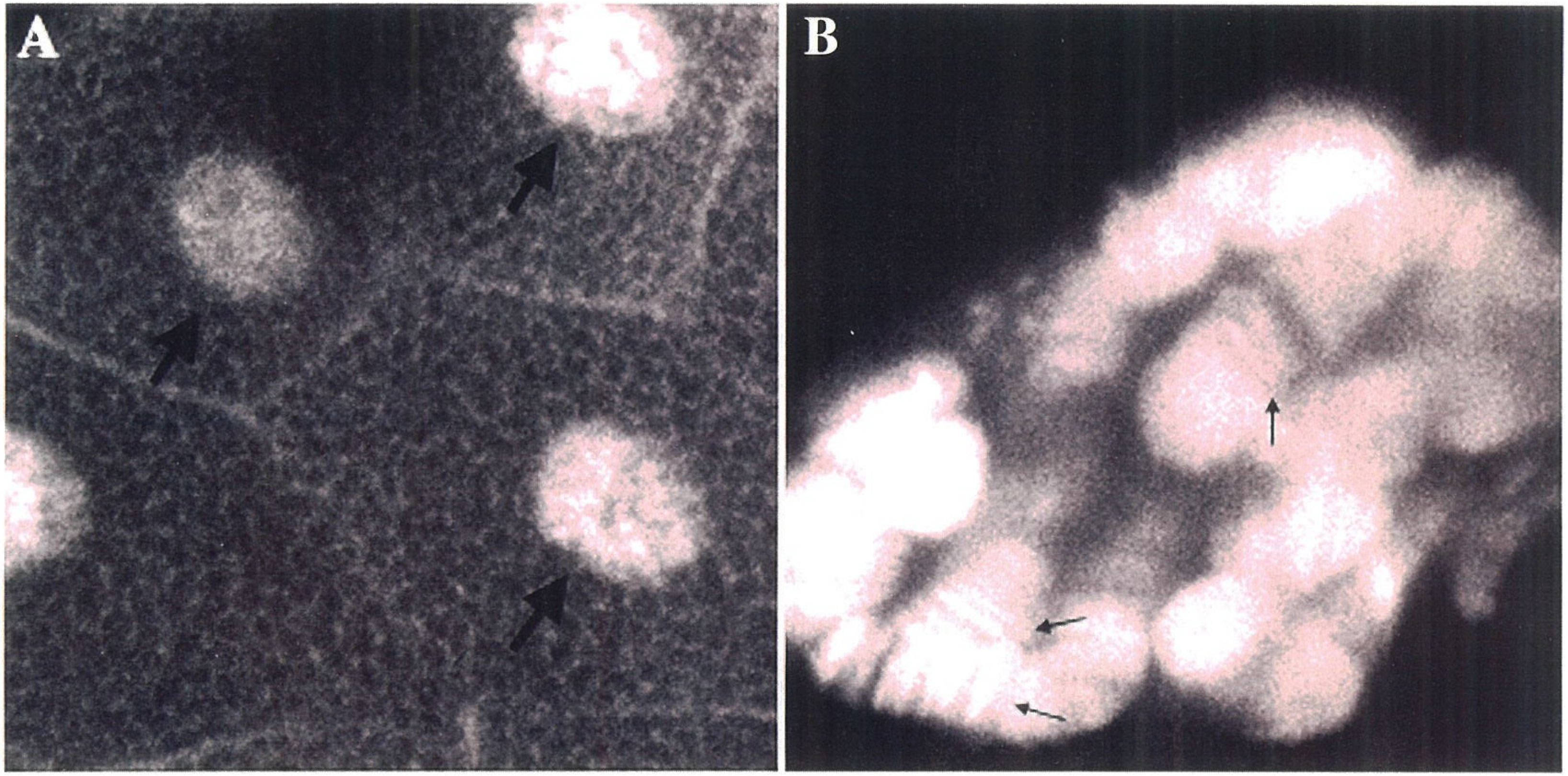

QUANTITATIVE CONFIRMATION

In TPLSM, a chromophore needs to absorb two IR photons simultaneously to reach an excited state, so the fluorescence emission intensity should depend quadratically on the excitation intensity. Therefore, if the logarithm of emission intensity is plotted as a function of the logarithm of the excitation intensities, the slope for two-photon excitation would be two and that for one-photon excitation (CLSM) would be unity. The simple derivation is as follows:

$$f(x) = cg(x)^p$$

$$\log[f(x)] = p\log[g(x)] + \log c$$

where f(x) and g(x) represent emission and excitation intensity, respectively. p is the power dependence. If p is found to be two, the emission intensity has quadratic dependence on excitation intensity, as expected of two-photon excitation.

To find out the relationship between excitation intensity and emission intensity experimentally, we used a homogeneous FITC-albumin gel as a fluorescent specimen. The excitation intensity was measured with an optical power meter (Newport model 835) under the stage, and the emission intensity was measured with the PMT in the TPLSM. The logarithm value of the emission intensity and the excitation intensity was plotted, and the slope of the plot was obtained by a Cricket software package.

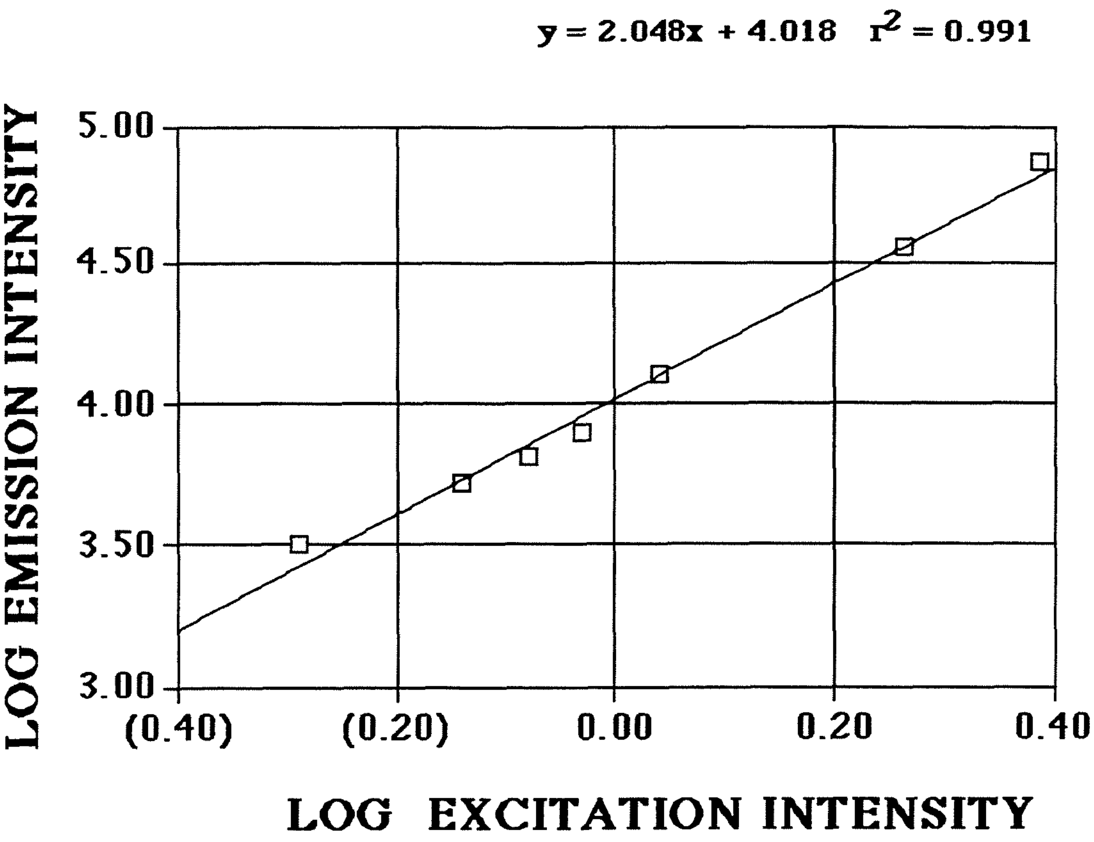

Fig. 2.2 Confirmation of two photon excitation. The slope shows that the emission intensity depends quadratically on the excitation intensity, thus validating the two-photon excitation. The parentheses denote negative values.

Fig. 2.2 shows the experimental data of the relationship. We fitted the curve and obtained the slope and deviation. Since the slope is very close to 2 while the deviation is small, this then confirms that the majority of the fluorescence came from two-photon excitation.

Fig. 2.3 Photobleaching Depth Comparison of Two-Photon Microscopy

Fig. 2.3. A vertical scanned image of an albumin-FITC gel after photobleaching the sample with two different laser intensities (1:2). The arrows indicate the photobleaching regions where double laser intensities induce photobleaching as much as four times.

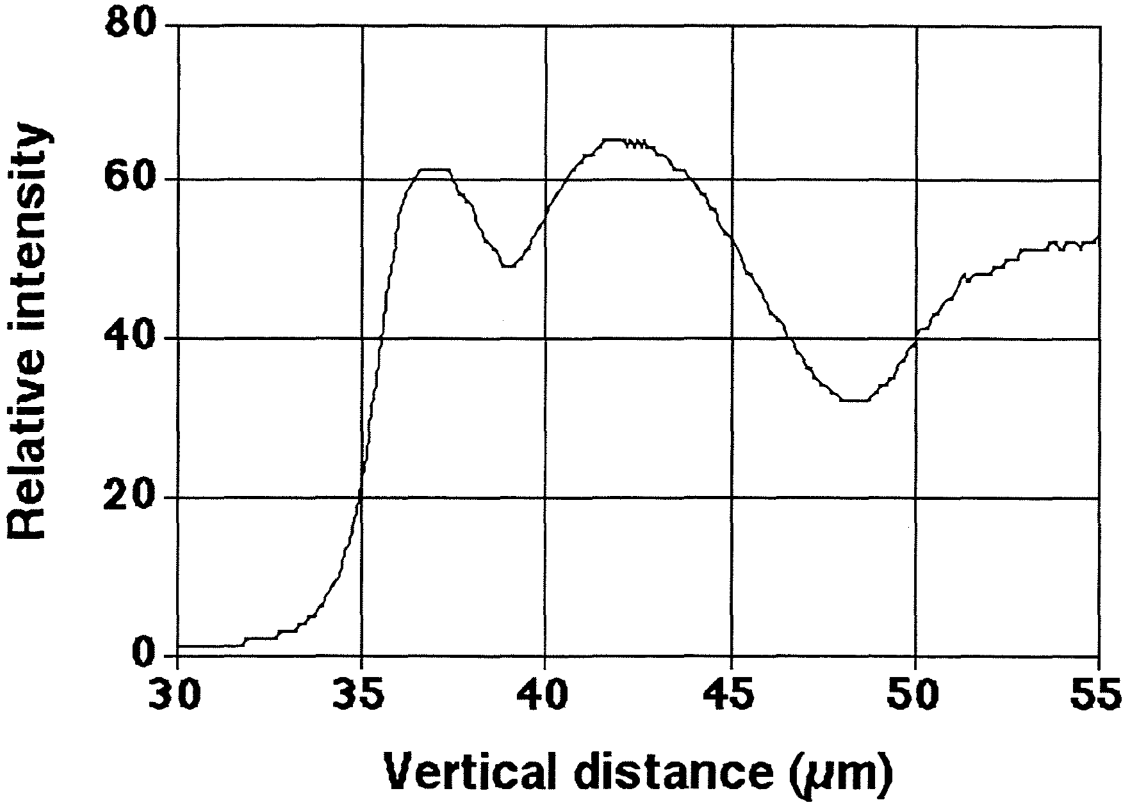

Fig. 2.4. Photobleach profile of albumin-FITC at one-to-two illumination. The left dip, 1.1 μm wide, resulted from 50% illumination and the right dip, 4.2 μm, was from 100% illumination. Note that the ratio of widths of the two dips is about 1:4, the square of the power ratio is 1:2.

Fig. 2.3 and 2.4 show the comparison of photobleaching regions at different excitation intensities. FITC-albumin gel was scanned 32 times at two focal planes with a Zeiss objective lens (20X, NA 0.4). The laser power for the top photobleached layer was 83 mW (50% attenuation) while that for the bottom one was 160 mW (measured under the microscope stage) The power was adjusted with a neutral density filter so the beam profile of the Ti-Sapphire laser was unchanged. Fig. 2.3 is the vertical scanned image of the specimen while Fig. 2.4 shows its intensity profile of the specimen through the depth of the scanned region.

Fig. 2.4 shows the quantitative depth measurements of the photobleaching . The top photobleaching depth, resulted from 50% illumination, is 1.1 μm (FWHM) while the bottom one, resulted from 100% illumination, is 4.2 μm. Therefore, double the excitation power increases two-photo-bleaching area by four times. This image reveals not only that the two-photon excitation was localized in the focal plane, but also that two-photon absorption depends quadratically on excitation intensity.

2.3. OPTICAL TRANSFER EFFICIENCY OF TPLSM

The optical transfer efficiency (OTE), defined as the detected signal throughput of an element from within the illumination volume, can help us optimize the signal collecting efficiency of our TPLSM. Although the aperture of CLSM is not necessary for TPLSM which leads to a reduction of the signal loss from the aperture, the OTE of TPLSM still suffers from the loss of limited collecting angle, scanning instrumentation, and low PMT quantum efficiency.

Table 2.1 shows the optical transfer efficiency for each component of our Sarastro 2000 in the signal collection path at λ=600 nm. The overall fluorescence detection efficiency is the product of the OTE of each element. The OTE measurement was done with a halogen lamp with a monochromator (Oriel, 77250) and a fiber bundle placed on the stage. The wavelength was set at 600 nm by the monochromator.

Table 2.1 also shows the overall optical transfer efficiency for a 63X (NA 1.4) oil-immersion objective lens. For λ= 600 nm, the overall OTE is less than 2%; that is, about two out of one hundred fluorescence photons from the specimen can be detected by our TPLSM.

COMPONENT	SPECIFICATION	OTE
Solid angle of collection	(NA 0.25-1.4)	0.015-0.3 (0.3)
Objective lens transmission		0.5-0.95 (0.75)
Nikon eyepiece	(λ=500-1000nm)	0.96-0.49 (0.96)
Scanning mirror		0.52
Primary dichroic mirror	680SP	0.94
PMT Quantum efficiency	(λ=185-800nm)	0.04-0.24 (0.16)
Overall fluorescence detection efficiency		0.017

Tab. 2.1 Optical transfer efficiency of each component of Sarastro 2000. Note that the measurement was done with a Zeiss 63X (NA 1.4) objective and λ=600 nm. The overall detection efficiency was determined with the numbers in the parenthesis, which are the OTE values at 600 nm.

Objective lens collection efficiency, one major unavoidable loss in TPLSM and other optical microscopy, is $\frac{1}{2}[1-\sqrt{1-\left(\frac{NA}{n}\right)^2}]$. Even with a high NA objective (NA 1.4), only about 30% (0.307) can be collected in a suitable medium. However, collecting signals from both sides of the specimen using two high NA objectives (4-Pi microscopy) can double the angle of collection (Hell and Stelzer, 1992).

The PMT used in Sarastro 2000 is a multi-alkali photocathode surface (Hamamatsu, R1447) with a QE of 24% to 4% from 185 nm to 800 nm. Matching photocathode material to the fluorescence wavelength can improve QE by a factor of nearly two (Art, 1995). Charge-coupled device (CCD) cameras commonly used in WFM usually have more than 50% QE. Therefore, improving the OTE of our TPLSM may be possible with a suitable detector.

2.4. POINT SPREAD FUNCTION AND RESOLUTION

The resolution of an optical microscope is limited by the Airy disc, which is the image of an infinitely small luminous object point. The radius r_{Airy} of the first dark ring around the central disk of the Airy diffraction image depends on the illumination wavelength λ_0 and the numerical aperture NA of the objective:

$$r_{Airy} = 0.61\frac{\lambda_0}{NA_{obj}}$$

Long illumination wavelengths and low NA increase the radius of the Airy disc and degrade the resolution.

Point spread function of WFM, CLSM and TPLSM

In 3-D optical microscopy, the point spread function (PSF), a 3-D image of an infinitely small luminous object point, can present the resolution and optical properties. For a wide field microscope, the PSF has the form of two concentric cones diverging on either side of the focal plane. The cross section of a PSF at the focal plane gives the Airy disc.

In an ideal CLSM or TPLSM, an illuminating aperture is raster-scanned across on a series of diffraction-limited spots in the specimen. However, the focused spots from CLSM or TPLSM are different from those from a conventional light source because of the gaussian profile of the laser sources. In addition, the confocal pinhole in CLSM and two-photon excitation of TPLSM change their PSFs dramatically. Therefore, the intensity distribution of the PSF of CLSM or TPLSM would differ from that of WFM.

In a CLSM system, the light emerging from the specimen is spatially filtered by the detection aperture, which is in a conjugate plane to the focal plane and confocal with the illumination aperture. The effect of this aperture is to apply another PSF; therefore, the combined PSF is the product of illumination and detection PSFs. If the illumination aperture is similar to the detection aperture, the CLSM PSF would be close to the square of the PSF of W.F. microscopy. This results in the reduction of the intensity of the subsidiary maximum; that is, the out-of-focus flare.

TPLSM, utilizing two-photon absorption to limit the excitation volume, does not require the detection aperture to achieve optical sectioning. Due to the simultaneous absorption of two photons, the PSF of TPLSM is, therefore, the square of illumination PSF and therefore is much smaller than that of WFM. Compared to CLSM, for the same chromophore, TPLSM requires a longer illumination wavelength and might have a greater

PSF. Table 2.2 shows the calculation of the PSFs from WFM, CLSM, and TPLSM, where $\sin\alpha$ is the numerical aperture of the lens. *u, v* are axial and radial normalized optical coordinates (Born M. and Wolf E. 1975).

Radial coordinate	$v = \frac{2\pi r \sin\alpha}{\lambda}$
Axial coordinate	$u = \frac{8\pi z \sin^2 \alpha / 2}{\lambda}$
Intensity PSF	$I(v,u) = \left\| 2\int J_0(v\rho)\exp(iu\rho^2/2)\rho d\rho \right\|^2$
Illumination PSF	$I_{ill}(v,u)$
Detection PSF	$I_{\mathrm{det}}(v,u)$
WFM PSF	$I_{WFM}(v,u) = I_{ill}(v,u)$
CLSM PSF	$I_{CLSM}(v,u) = I_{ill}(v,u) I_{\mathrm{det}}(v,u)$
TPLSM PSF	$I_{TPLSM}(v,u) = I_{ill}^2(v/2, u/2)$

Tab 2.2 The theoretical calculation of PSFs of WFM, CLSM and TPLSM.

Measure point spread function of TPLSM and resolution

Experimentally, for a 3-D fluorescence microscope, PSF is usually acquired by taking the 3-D images of sub-resolution fluorescent beads. The point spread function shown in Fig. 2.4 and Fig. 2.5 was the average image of three bead images acquired with our TPLSM. The diameter of the fluorescent beads (Molecule Probe) is 0.1 µm. The objective is a Zeiss 63x oil (NA 1.4). The pixel spacing was 0.08 µm and the step size, the distance between two adjacent scanning focal planes, was set to 0.18 µm.

Optical Sections and Vertical Projection of Point Spread Function of our TPLSM

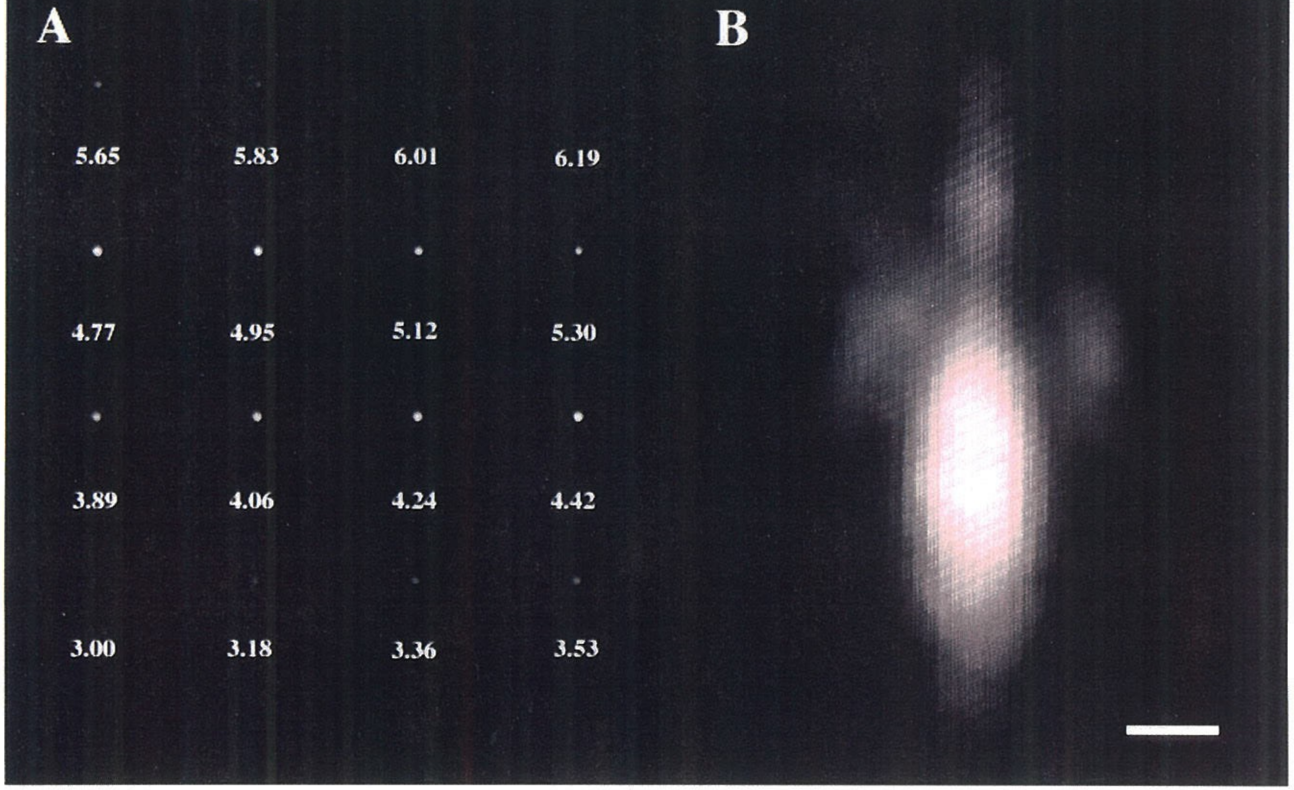

Fig. 2.5 (A) Optical sections of PSF of our TPLSM with a Zeiss 63x objective (NA 1.4). The images represent a series of 2-D scanned image of a 0.1 μm-diameter fluorescent bead at different focuses. The distance between two adjacent scanning planes is 0.18 μm. (B) The vertical projection of a 3-D PSF of our TPLSM. The scale bar is 0.5 μm.

Conventionally, the resolution is defined as the full width of half-maximum (FWHM) of the PSF. From this definition the lateral resolution of our TPLSM is 500 nm and its axial resolution is 1440 nm. The PSF images of TPLSM show that the resolution in the axial direction is still about three times worse than that in the focal plane. In chapter four the resolution of both CLSM and TPLSM were shown to be greatly improved using image deconvolution techniques.

2.5. SIGNAL-TO-NOISE RATIO

Noise sources of our TPLSM

The overall image quality can be expressed in terms of signal-to-noise ratio. The noise in TPLSM contain shot noise, electronic noise, and background noise. The shot noise comes from the statistical variation in the number of detected photons, which obeys a Poisson distribution. Electronic noise results from the amplification of the PMT's photo current, so it depends on the dark current and characteristics of the PMT. The background noise is due to the reflected/scattered light in the detection path.

Because TPLSM requires that one chromophore absorbs two photons simultaneously (within the fluorophore lifetime; nanosecond order), the cross section of two-photon excitation is very small (about 10^{-49} cm^4 sec/photon), thus resulting in weak fluorescence signal level. Moreover, photobleaching occurs on the chromophore after laser illumination and then limits the laser exposure time and total number of detected photons. These factors result in the significance of shot noise in the images of TPLSM and degrade the image quality.

The photomultiplier tube (PMT) that is used in our TPLSM is a Hamamatsu R1477, which has a quantum efficiency of 16% at 600 nm and a dark current of 3nA at 1000V. The electronic noise output of this PMT is only 1.7×10^{-16}W, which was determined by the following equation:

$$ENI = \frac{\sqrt{2qI_{adc}G\Delta f}}{S}$$

where q = charge of one electron

I_{adc}= anode dark current

G = current amplification

Δf= bandwidth of the system in hertz

S = anode radiant sensitivity in amperes per watt at the wavelength of peak response

If the electronic noise is much less than the shot noise, the signal-to-noise ratio can be expressed as

$$SNR = \frac{Q_e n_p}{\sqrt{Q_e n_p + n_n{}^2}} \approx \sqrt{Q_e n_p}$$

where n_p denotes the number of detected photons and n_n denotes the noise from the sensor.

Methods of increasing signal-to-noise ratio

To observe the behavior of the background and electronic noise of this PMT, we measured the background intensities of the average image of different frames (1,2,4,8,16,32) and its standard deviation at two cases: laser on and laser off. The power of the Ti-Sapphire laser was set to 136 mW and the PMT voltage was set to 1050 V. As no specimen were on the stage, all the signals were from dark current or reflecting/scattering light from mirrors and filters.

Fig. 2.6 shows the image pixel value of the mean background at various counts of the averaged frames. The background, while the laser beam was blocked (laser-off), came from electronic noise; the background, while the laser was not blocked (laser-on), resulted from electronic noise as well as the stray photons that entered the PMT. The background noise did not change much (less than 10%) over the average while the standard deviation of the background was greatly reduced (over 70%). The laser-on background was more than five times that of the laser-off background, indicating that the reflecting/scattering light dominated the dark current at a high PMT voltage when the laser was on. Assuming the image intensity is about 250, the electronic noise accounts for only less than 1% of the image intensity and the reflecting/scattering light less than 5% (Fig. 2.6). Therefore, the shot noise is the dominant noise source in our imaging system.

Fig. 2.7 shows the image pixel value of the dark current at various PMT voltages. This measurement is similar to the previous laser-on experiment. The results indicate that the background noise and its standard deviation have a non-linear increment when the PMT voltage increased from 700 V to 1056 V.

Because the software of our TPLSM acquires 8-bit images, the pixel value of the brightest pixel, without saturation, is about 250 and therefore its shot noise is about 16. These two experiments reveal that the pixel value of the combined noise of our TPLSM, even at the greatest PMT voltage, is only about five. Therefore, the best SNR that can be obtained with our TPLSM is about 15; the lowest signal that be distinguished from the noise (SNR=1) is about 6.

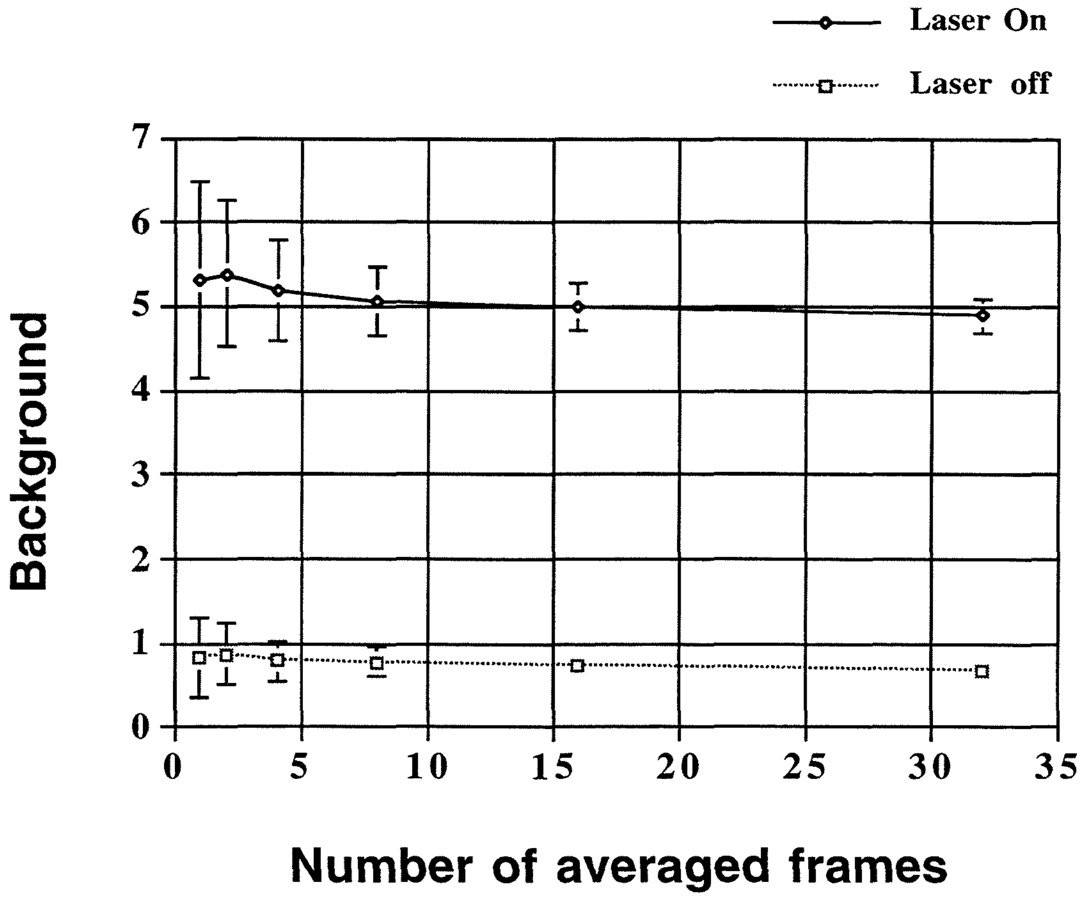

Fig. 2.6 The background and noise at the averaged image of different number of frames (1, 2,4,8,16,32). The PMT voltage was set to 1050V. The error bar indicates the standard deviation of the dark current. The dash curve was measured while the Ti-Sapphire laser beam was blocked while the solid curve was measured while the laser beam not blocked.

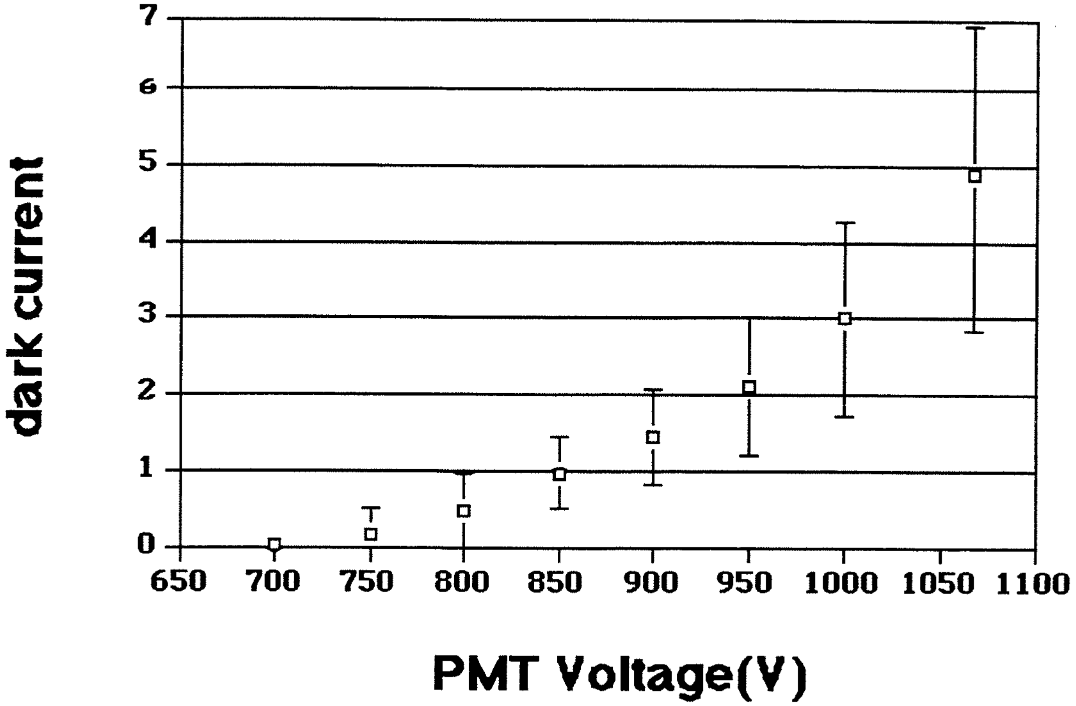

Fig. 2.7 The dark current of the detector at different PMT voltage. The error bar indicates the standard deviation of the dark current. This data was measured while the Ti-Sapphire laser was on with an average power 103 mW on the stage without a specimen.

REFERENCES

Born, M., and Wolf, E., 1975, Principles of optics, 5th Ed. Pergamon Press, Oxford

Denk, W., Piston, D.W., and Webb, W.W. 1995 "Two-photon molecular excitation in laser-scanning microscopy," in *Handbook of biological confocal microscopy* 2nd edition, Plenum Press, New York. 445-458

Friedrich D.M.,1982, "Two-Photon Molecular Spectroscopy," *J Chemical Education* **59** (6) 472-481

Gu, M., and Sheppard, C.J.R., 1995, "Comparison of three-dimensional imaging properties between two-photon and single-photon fluorescence microscopy," *J. of Microscopy* Vol **177** 128-137

Hell, S., and Stekzer, E.H.K., 1992, "Fundamental improvement of resolution with a 4Pi-confocal fluorescence microscope using two-photon excitation," *Opt. Comm.* **93** 277-282

Hell, S.W., Soukka, J., and Hanninen, P.E., 1995, "Two- and multiphoton detection as an imaging mode and means of increasing the resolution in far-field light microscopy: a study base on photon-optics," *Bioimaging* **3** 64-69

Piston, D.W., Kirby, M.S., Cheng, H., Lederer, W.J., and Webb, W.W., 1994, "Two-photon-excitation fluorescence imaging of three-dimensional calcium-ion activity," *Applied Optics* **33** (4) 662-669

Roy, M., and Sheppard, C.J.R., 1993. "Effects of Images Processing on the Noise properties of Confocal Images," *Micron* Vol **24** (6) 623-635

Sandison, D. R., Williams, R.M., Wells, K.S., Strickler, J., Webb, W. W., "Quantitative Fluorescence Confocal Laser Scanning Microscopy," in *Handbook of Biological Confocal Microscopy* 2nd ed. Pawley J.B. Plenum Press, New York. 39-53

Shaw, P., Highett, M., and Railings, D., 1992. "Confocal microscopy and image processing in the study of plant nuclear structure," *Journal of Microscopy, The Royal Microscope Society.* **166**: 87-97

Shaw, P.J. 1995. "Comparison of Wide-Field/Deconvolution and Confocal Microscopy for 3D Imaging," in *Handbook of Biological Confocal Microscopy* 2nd ed. J. B. Pawley, Ed., Plenum Press, New York pp. 373-387

Sheppard, C.J.R., Gan, X., Gu, M., and Roy, M., 1995 "Signal-to-Noise in Confocal Microscopes," in *Handbook of Biological Confocal Microscopy* 2nd ed. Pawley J.B. Plenum Press, New York. 363-371

van der Voort, H.T.M., and Strasters, K.C. 1995. "Restoration of confocal images for quantitative image analysis," *Journal of Microscopy* **178** (2): 165-181

Xu, C., Zipfel, W., Shear, J. B., Williams, R. M., and Webb, W. W., 1996, "Multiphoton fluorescence excitation: New spectral windows for biological nonlinear microscopy," *Proc. Natl. Acad. Sci. USA* **93** 10763-10768

Xu, C., and Webb, W.W., 1996, "Measurement of two-photon excitation cross sections of molecular fluorophores with data from 690 to 1050 nm," *J Opt. Soc. Am. B***13**(3) 481-491

CHAPTER III

COMPARISON OF CONFOCAL AND TWO-PHOTON LASER SCANNING MICROSCOPY

3.1 INTRODUCTION

Two-photon laser scanning microscopy (TPLSM) offers many new opportunities for biological research. However, many aspects of TPLSM are yet to be explored to realize its potentials and limitations. For example, because TPLSM utilizes twice the excitation wavelengths as CLSM does, the overlap between the emission and excitation spectra for TPLSM is much less than CLSM. Therefore, signal loss of TPLSM from cross talk is less than CLSM and it is worthwhile to compare their optical transfer efficiency. On the other hand, the longer excitation wavelengths of TPLSM present intrinsic restrictions on both the lateral and axial resolutions, which depend directly on excitation wavelengths (Inoue, 1995)

Lateral resolution

$$r_{Airy} = 0.61\frac{\lambda_0}{NA_{obj}}$$

Axial resolution

$$z_{\min} = \frac{2\lambda\eta}{(NA_{obj})^2}$$

where $Z_{\min}$ denotes the distance between the first minimum of PSF in the axial direction. This restriction may limit application of TPLSM when imaging fine biological structures but can be overcome by image deconvolution techniques (See chapter IV).

As was mentioned in the previous chapter, the resolution of CLSM and TPLSM could be determined by the FWHM of PSF. It was calculated and observed that both the lateral and axial resolution of CLSM improved with a smaller pinhole (Wilson, T. 1995) and that the lateral resolution seemed more sensitive to finite detector size than axial resolution. However, signal-to-noise ratio (SNR) of images might be further deteriorated with an extremely small pinhole, thus, the "optimal" aperture size is about 50%-75% the diameter of the first minimum in the Airy disk. Therefore, it is worthwhile to study the resolution and SNR with apertures of different sizes to obtain the optimal aperture size for our CLSM.

The effect of the refractive index mismatch on the image quality in TPLSM was investigated by Jacobsen (1994). The results showed a greater decrease in the image intensity using a high NA objective when the focus was moved deeper into the specimen. However, the image brightness decrease as a function of depth is yet to be studied. We explored the brightness decay both as a function of the illumination intensity and excitation mechanism (one photon vs. two-photon). We also examined the effect of refractive index mismatch to compare the intensity decrease as a function of depth with objectives at various NA.

The depth of field of a microscope, defined as the depth of the image that appears to be sharply in focus at one setting of the fine-focus adjustment, plays an important role in imaging, especially for 3-D imaging rendering. It determines the depth of information contained in a 2-D scanning image. The larger the depth of field, the greater step size it requires to prevent overlapping signals. Many factors, including NA and magnification of objective, illumination wavelength, and confocal pinhole size affects the depth of field of the microscope.

A quantitative comparison of the Sarastro 2000 CLSM and our TPLSM is presented to show the advantages and disadvantages of our TPLSM system after the modification described in this chapter. Signal-to-noise ratio and resolution are shown to depend on excitation intensity and confocal pinhole size in section 3.2. In section 3.3, the effects of NA and pinhole size on the depth of field of TPLSM were investigated. In section 3.4, 3.5, photo-bleaching and deep tissue imaging of TPLSM and CLSM are compared respectively. This information will lead to other research that helps optimize our TPLSM and establish criteria for optimal image quality for biological research.

3.2 SIGNAL-TO-NOISE RATIO AND RESOLUTION

Resolution and SNR of CLSM

The resolution and SNR were obtained and compared using the PSFs of a Zeiss confocal microscope 310 at different pinhole sizes. The PSFs were acquired, as stated in the previous chapter, by imaging 0.1 μm fluorescent beads with a Zeiss 63x oil (NA 1.4) objective at 488 nm illumination. SNR here is defined as the peak pixel value of the PSF images divided by the noise of the image background; the resolution here is the full width of half maximum (FWHM) of the PSF images.

Table 3.1 shows that both lateral and axial resolution degrade by 40% but the SNR improves by 200% when the aperture size increases from 17.5μm to 70μm. Therefore, a 17.5μm aperture provides better resolution but a further degraded SNR than a 70μm aperture. However, the resolution degrades by about 33%, but the SNR improves by 333% when the aperture size increases from 17.5μm to 35μm. Considering both resolution and SNR, the overall image quality is optimal at a 35 μm pinhole size. Fig. 3.1 shows the relative SNR and resolution of a Zeiss confocal microscope 310 with a Zeiss oil 63X (NA 1.4) objective.

Resolution and SNR of TPLSM

The PSF size in TPLSM depends on excitation intensities. That is, varying illumination laser power affects not only the image SNR but also their resolution. The excitation intensity of our TPLSM was changed using a neutral density filter before scanning the specimen and was measured with a power meter (Newport, 835) beneath the specimen stage. Again the resolution and SNR were measured as stated previously.

Table 3.2 shows the resolution and SNR at different excitation intensities from our TPLSM. 100%, 50%, and 10% excitation intensities correspond to a measured power 192 mW, 99 mW, and 21 mW. These results show that lateral and axial resolutions degrade 10% and 30%, respectively, while excitation intensities increase by five and ten times. However, the SNRs improve by 50% and 360%, respectively, when excitation intensities increase by five and ten times. From Fig. 3.2, the relative SNR and resolution of TPLSM as a function of excitation intensity suggested that 192 mW provides the best overall image quality although the resolution is a little degraded.

However, because emission intensity of fluorescence of a chromophore depends on the quantum efficiency and two-photon absorption cross section of the chromophore, the laser power measured here should be treated as a reference but not an absolute value. Although SNR may increase with higher laser power, saturation of fluorescence occurs and reduces the image SNR when most fluorophore molecules are in the excited states and have no capability of absorbing photons (Sandison et al., 1995)

Pinhole Size	FWHM (x-y)	FWHM (x-z)	SNR
17.5 μm	271 nm	1010 nm	48
35.0 μm	364 nm	1400 nm	208
70.0 μm	390 nm	1430 nm	156

Tab. 3.1 Lateral (x-y) and axial (x-z) resolution and SNR of Zeiss 310 at different pinhole sizes.

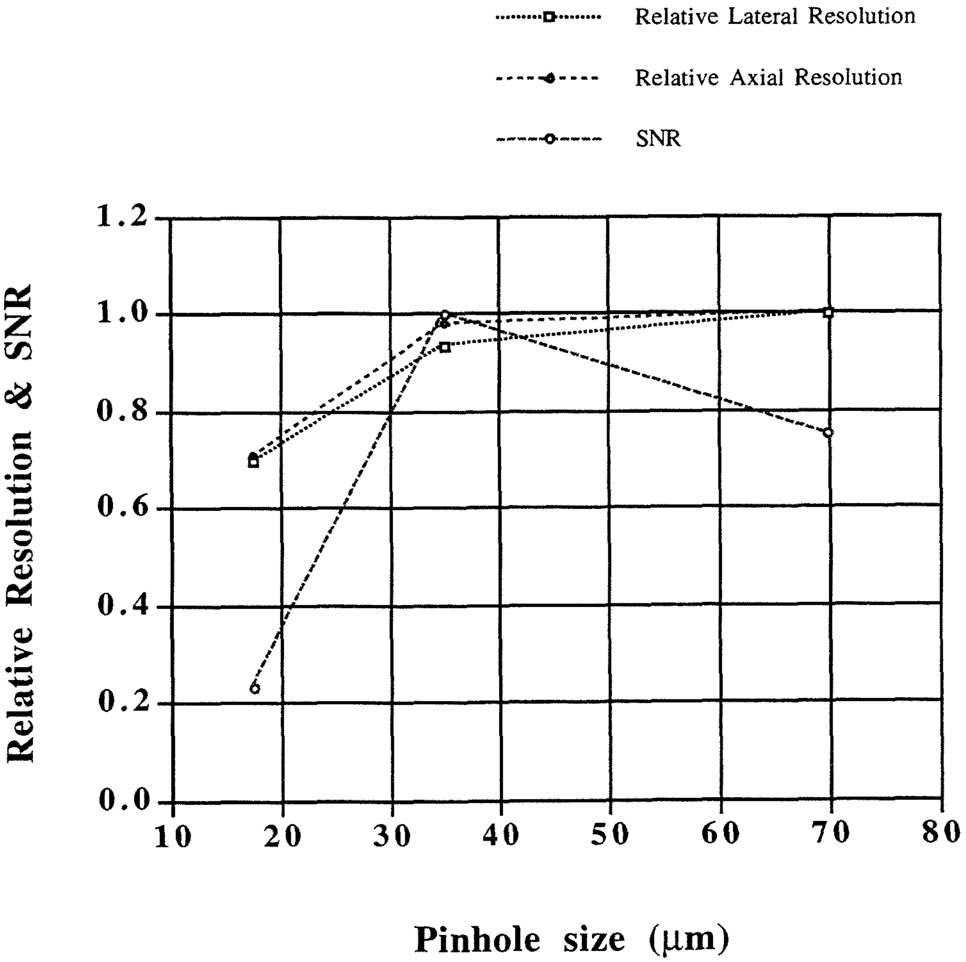

Fig. 3.1 The relative lateral and axial resolution and SNR of Zeiss 310 with 63X (NA 1.4) at pinhole size 17.5 μm, 35 μm, and 70μm. The FWHM of PSF with 70 μm pinhole was set to unity. The SNR of PSF with 35 μm was also set to unity.

Comparison

As discussed in the previous chapter, Optical transfer efficiency (OTE) of the signal collection path of CLSM or TPLSM plays an important role in image quality. Low OTE not only degrades the signal-to-noise ratio of images, but also might mislead a user to set the microscope incorrectly and result in saturation of the fluorophores or photo damage to the specimen. Because the collecting paths of the Sarastro 2000 and our TPLSM are the same, the OTE difference is the pinhole and the dichroic mirror. The Sarastro 2000 uses a 510 DRLP long-pass dichroic mirror and a 50-200 μm aperture while our TPLSM uses a 670 DCSP (Chroma) short-pass dichroic mirror but no aperture. To detect fluorescence emission at 600 nm, both dichroic mirrors have about a 95% optical transmission. In this case, the only OTE difference comes from the aperture, so the OTE of TPLSM is five times larger than that of CLSM. TPLSM, in our case, utilizes fluorescent signals more efficiently than CLSM.

In Fig. 3.4, the PSFs of CLSM and TPLSM are compared and show that resolution of TPLSM, due to long excitation wavelength, is not superior to that of CLSM. This result agrees with the prediction of PSF theory (See chapter II); however, it only holds for surface imaging. For deep tissue imaging, since TPLSM suffers less from tissue scattering than CLSM, thus has a better image quality (See chapter V).

Fig. 3.2 PSF of TPLSM with various excitation intensities. The top row is the horizontal cross section while the bottom row is the vertical cross section. 100, 50, and 10 correspond to measured powers 192 mW, 99 mW, and 21 mW. These images were presented in pseudo color (rainbow) mode where red denotes the brightest pixel value and blue the lowest pixel value. These images show that less excitation intensity results in a little smaller PSF with less out-focus flare, but is not proportional to the PSF size.

Fig. 3.2 Point Spread Functions of TPLSM at various excitation intensities

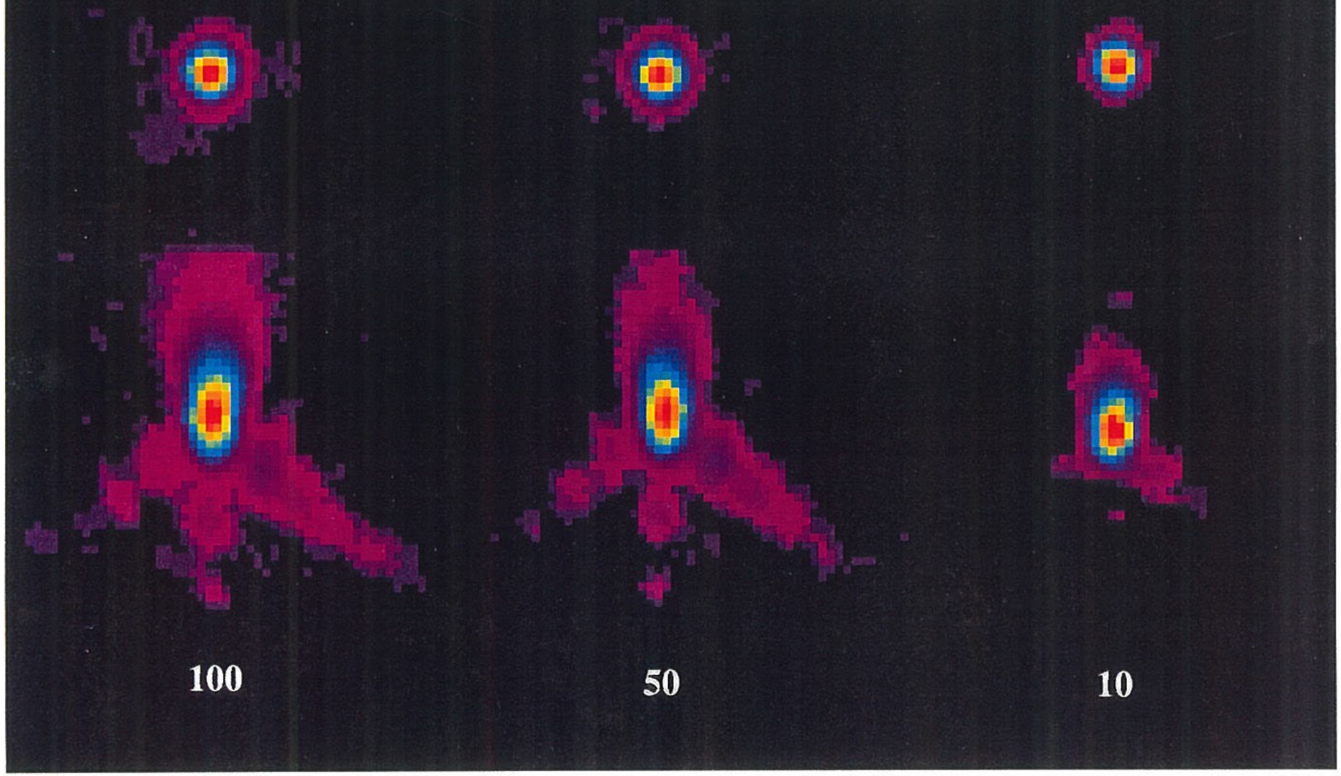

Excitation Intensity	FWHM (x-y)	FWHM (x-z)	SNR
10 %	330 nm	1160 nm	61.3
50 %	355 nm	1440 nm	97.7
100 %	368 nm	1510 nm	280

Tab. 3.2 Resolution and SNR of TPLSM at various excitation intensities.

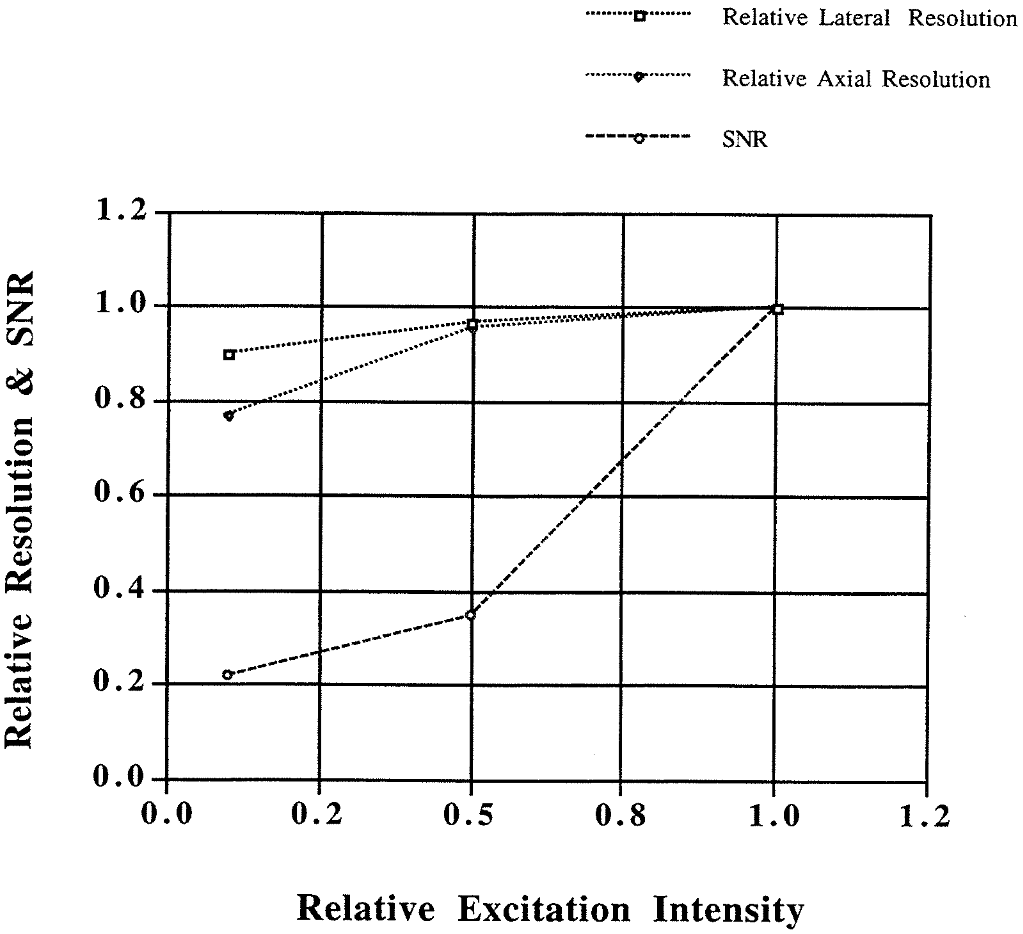

Fig. 3.3 The relative lateral and axial resolution and SNR of our TPLSM with 63X (NA 1.4) at different excitation intensities, shown by percentage. The FWHM and the SNR of PSF with 100% were set to unity.

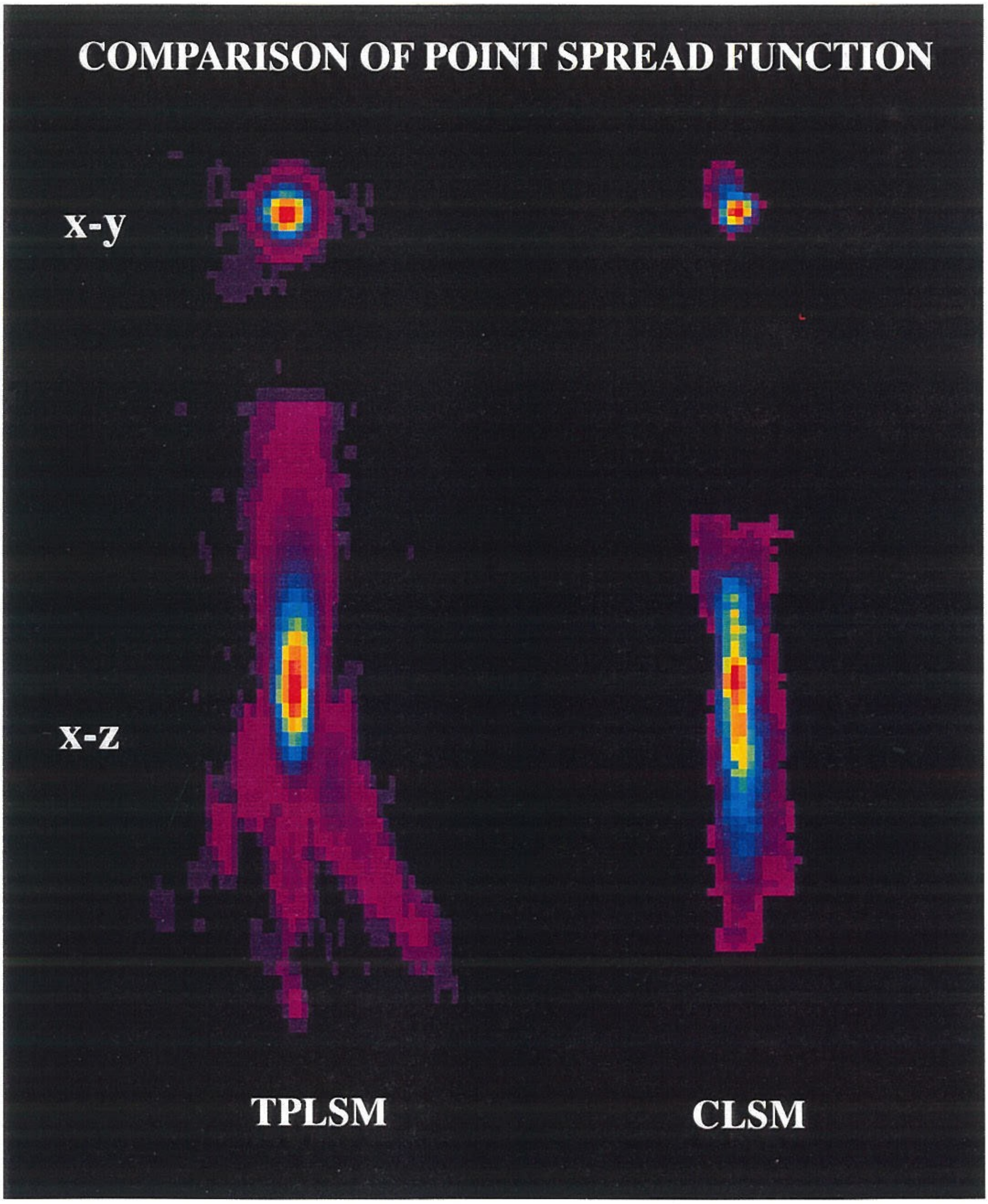
COMPARISON OF POINT SPREAD FUNCTION
x-y
x-z
TPLSM
CLSM

Fig. 3.4 Comparing the PSFs of CLSM and TPLSM at the same SNR. PSF of CLSM is a little bit less than that of TPLSM and has no out-of-focus flare.

3.3 DEPTH OF FIELD

The depth of field of a microscope is defined as the depth of the image that appears to be sharply in focus at one setting of the fine-focus adjustment. The depth of field depends on (1) the diffraction-limited spreading above and below the focus plane of the signals coming from a single-point source in the specimen, (2) the accommodation of the observer's eyes, and (3) the final magnification of the images (Berek, 1927). The second factor does not affect our results since our images were acquired with an electronic device like a PMT. The third factor is not important because the diffraction pattern is larger than the unit pixel size (0.08 μm with a Zeiss 63X oil objective).

When the detector is made up of resolution elements spaced sufficiently finer than the Airy disk radius, only the diffraction-limited depth of field needs to be considered. In this case, the depth of field can be taken as

$$\delta = \frac{1}{4}(z_{\min+} - z_{\min-})$$

That is, one quarter of the distance between the first axial minimum above ($z_{\min+}$) and below ($z_{\min-}$) the central maximum in the 3D Airy pattern converted to distances in specimen space. If the point spread function of the imaging system is axially symmetric, the depth of field is half of the axial resolution.

In our experiment the depth of field of TPLSM with various pinhole sizes were compared. An Olympus 10X DPlanApo(NA 0.4) and a Nikon 20X Fluor (NA 0.75) objective were utilized to image pollen grains at different pinhole sizes (open, 50 µm, 100 µm, and 200µm). Laser power and PMT voltage were adjusted so that the peak pixel values were about the same. Each image of the pollen grains was obtained by averaging ten frames of scanning to minimize noise.

Fig. 3.5 shows the comparison of depth of field of TPLSM with these two objectives at a pinhole size of 50 µm, 100µm, 200 µm and open. These images are presented in pseudo color (rainbow) mode where red denotes the brightest pixel value and blue the lowest pixel value. The red-yellow pollen grain in the center of the image is in focus while the blue pollen grain in the upper left corner was out of focus. The more out-of-focus residual images indicate a greater depth of field. These images reveal that a high NA/magnification objective and a smaller confocal pinhole have less depth of field.

In addition, two out-of-focus pollen grains were chosen to calculate the image contrast to give a quantitative measure of depth of field and image quality. Fig. 3.6 shows that the image contrast is greatest with 20X (NA 0.75) at 200 µm. It decreased by about 5% when the pinhole was switched open and decreased by almost 60% when a low NA objective was used and the pinhole was switched to 50 µm. Therefore, although a smaller pinhole decreases the depth of field, it may not render as good an image quality due to higher noise.

Fig. 3.5 Comparison of depth of field of TPLSM with two objectives (top row: Nikon Fluor NA 0.75; bottom row: Olympus 20X DPlanApo NA 0.4) at pinhole size 50 µm, 100 µm, 200 µm, and open. These images were presented in pseudo color (rainbow) mode where red denotes the brightest pixel value and blue the lowest pixel value. The pixel size was chosen to be 0.5 µm. Less out-of-focus signals appear with a higher NA objective and a smaller pinhole.

DEPTH OF FIELD OF TPLSM AT VARIOUS PINHOLE SIZES

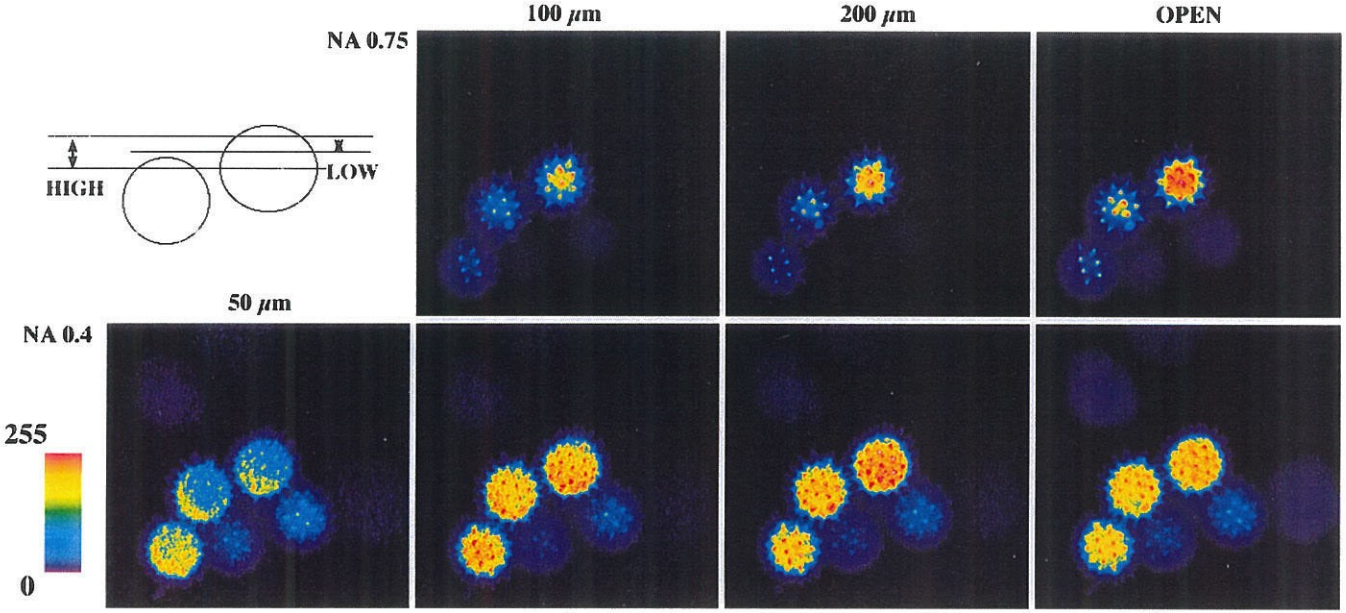

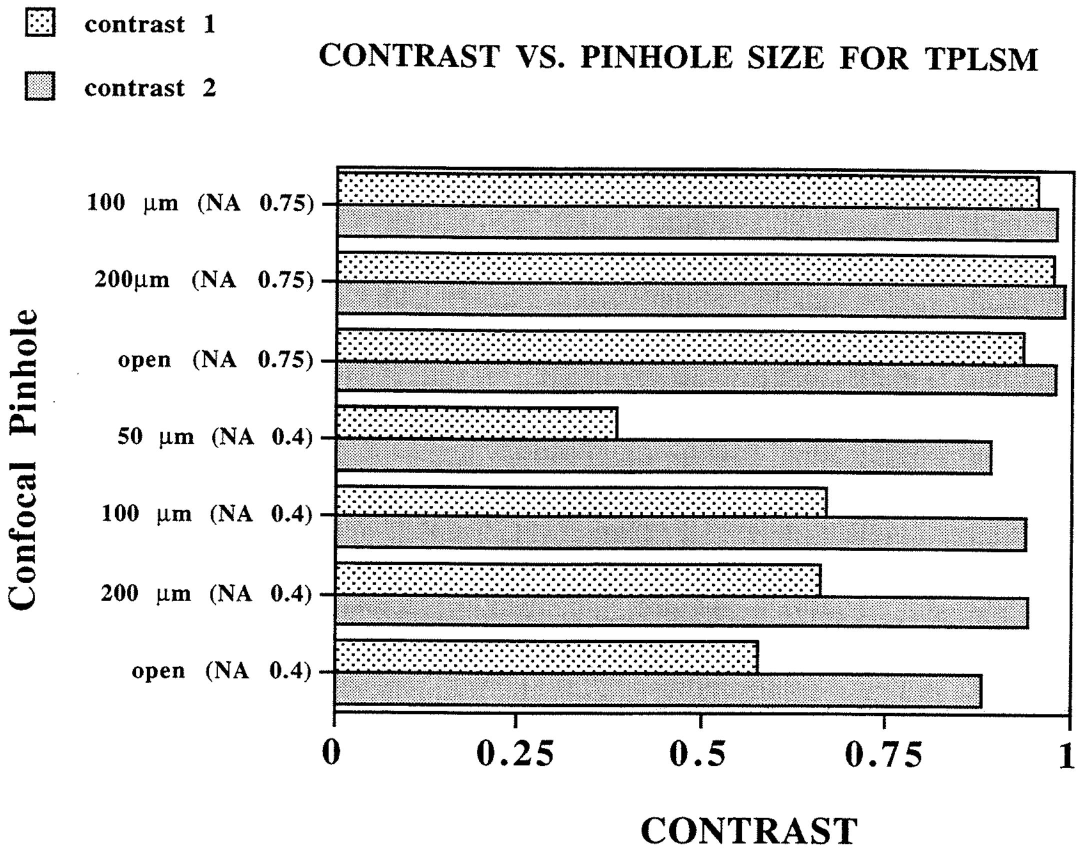

Fig. 3.6 Comparison of image contrast of TPLSM with two objectives (top row: Nikon Fluor NA 0.75; bottom row: Olympus 20X DPlanApo NA 0.4) at pinhole size 50 µm, 100 µm, 200 µm, and open. These contrast values show a quantitative comparison of depth of field in these cases.

3.4 PHOTOBLEACHING

Theory

Photobleaching, an irreversible process, transforms dye molecules into a non-fluorescent state and decreases the total amount of fluorescence. A chromophore is excited to a vibrational state within the first excited singlet band (S1) by absorbing one or multiphotons and then relaxes to the lowest vibrational level of S1 by a non-radiation process in about 10^{-12} sec. This relaxation causes Stoke's shift and thereby the red shift between the emission and excitation spectra of the organic fluorophore. At this lowest vibrational level, the fluorescence emission process (about 1-10 ns lifetime) competes with other decay processes, including intersystem crossing and photobleaching. Intersystem crossing occurs when an excited electron undergoes a spin flip, trapped in the long-lived T1 state (about 100 ns lifetime), thus reducing the effective fluorophore concentration. On the other hand, photobleaching occurs when fluorophores undergo an oxidation reaction and then lose the capability of emitting fluorescence (see Fig. 3.7).

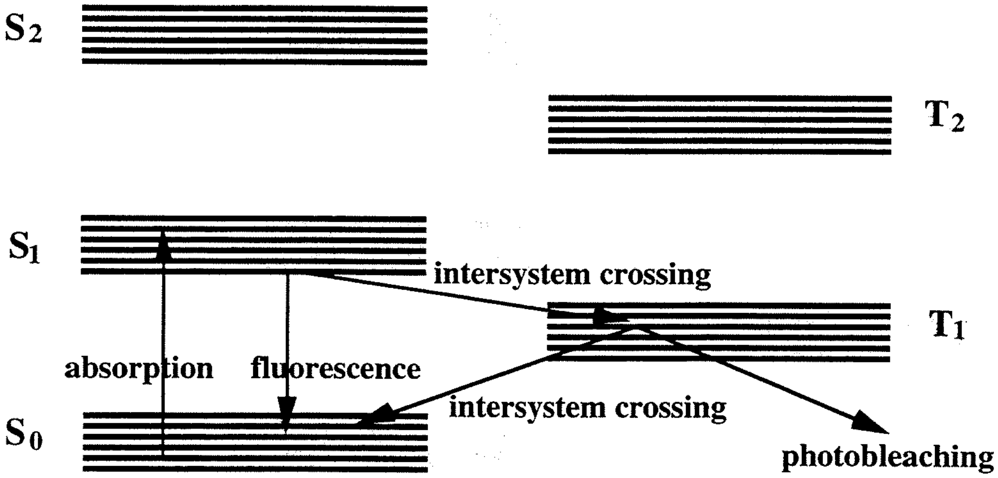

Fig. 3.7 Schematic diagram of photobleaching process of a dye molecule.

Experimental comparison of photobleaching

Photobleaching phenomena of TPLSM and CLSM were examined by imaging an FITC-albumin gel. First the relationship between the excitation and emission intensities of TPLSM and CLSM was compared (See Fig. 3.8). As was mentioned in the previous chapters, emission intensity of TPLSM depends quadratically on excitation intensity while that of CLSM depends linearly on excitation intensity. In Fig. 3.8, the slope of TPLSM is about two while that of CLSM is one.

Moreover, the cross section area of the illumination laser beam is proportional to the square of the axial distance to the focus (Z_i), so the illumination intensity decays quadratically as a function of Z_i. Therefore, instead of exciting all the dye molecules in the illumination path like CLSM (concentric cones diverging either side of the focal plane), TPLSM confines the excitation region to the focal spot. This mechanism greatly reduces the volume where photobleaching may occur, especially for 3-D imaging. Fig. 3.9 shows the photobleaching comparison between CLSM and TPLSM.

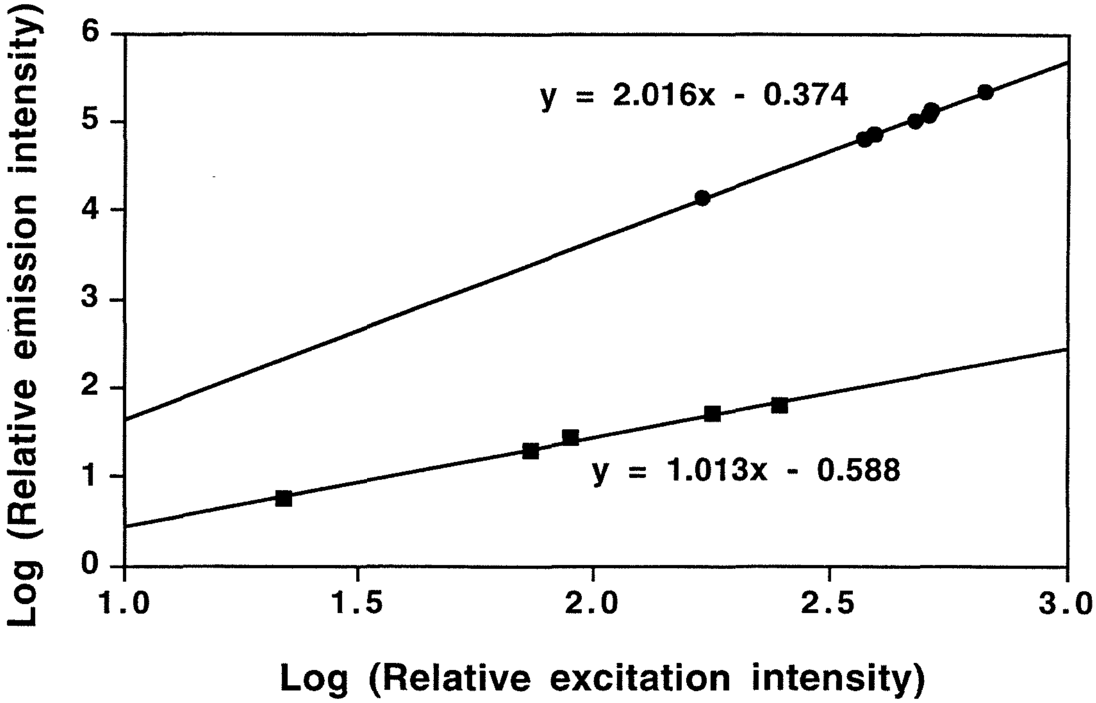

Fig. 3.8 Comparison of emission intensities of TPLSM and CLSM as a function of excitation intensities. The top line represents the data obtained from TPLSM while the bottom line was from CLSM. The results show the quadratic dependence of emission intensity and therefore confirm two-photon excitation.

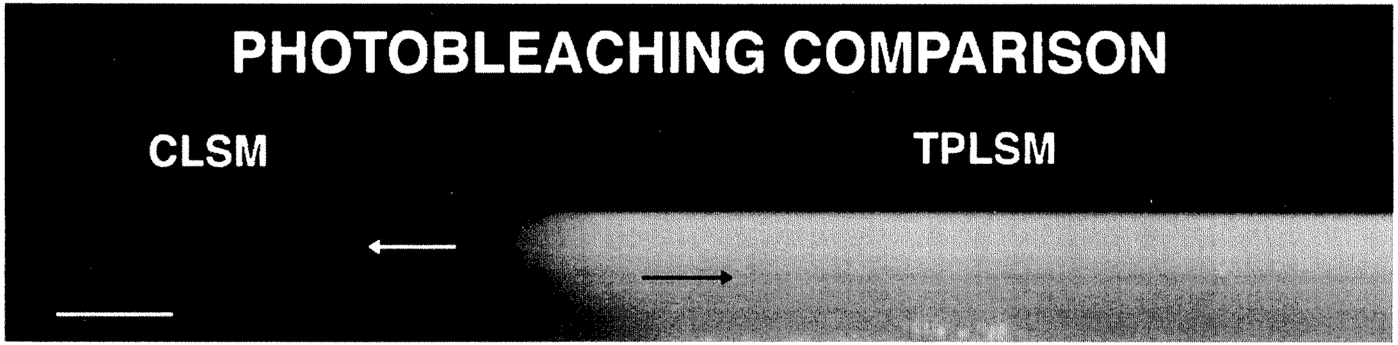
PHOTOBLEACHING COMPARISON
CLSM
TPLSM

Fig. 3.9 Vertical scanned image of FITC-albumin gel to show the photobleaching comparison of TPLSM (right) and CLSM (left) side by side. Arrows show the focus of TPLSM and CLSM. The gel on the left side was scanned 70 times with CLSM while the gel on the right side was scanned 630 times with TPLSM. To make a fair comparison, the power of the argon and the Ti-Sapphire laser was adjusted so as to have the same emission intensity at the same PMT voltage. In Fig. 3.9, compared to CLSM, TPLSM greatly reduced photobleaching, which occurs only at focus rather than out-of-focus regions.

3.5 DEEP TISSUE IMAGING

Although CLSM revolutionizes biological research by providing 3-D images with a non-invasive sectioning, it is difficult to acquire useful images deep within tissue because of heavy tissue scattering. Image degradation due to scattering at short wavelengths will be discussed in chapter five. However, it is interesting and useful to compare the penetration depth of CLSM and TPLSM. Moreover, it is important to examine the penetration depth with different NA and excitation intensities.

Excitation Intensity

An FITC-albumin gel was used to examine the penetration depth of CLSM and TPLSM because of its homogeneity. The scanning mode was set to vertical linear scanning so as to obtain the vertical intensity profile. Fig. 3.10 shows the fluorescence intensity as a function of depth at various intensities of TPLSM. Each vertical pixel represents 1.5 μm depth while a 100% curve has serious saturation with no apparent decay. In contrast, a 50% curve has a lower peak (start) intensity than CLSM (one-photon); however, it also has a lower decay rate (1.25/pixel) than CLSM (3.25/pixel) and therefore TPLSM is shown to penetrate deeper than CLSM. Compared to the 50% curve, the 10%, 3% and 1% curves

Comparison of Intensity Decay as a Function of Imaging Depth

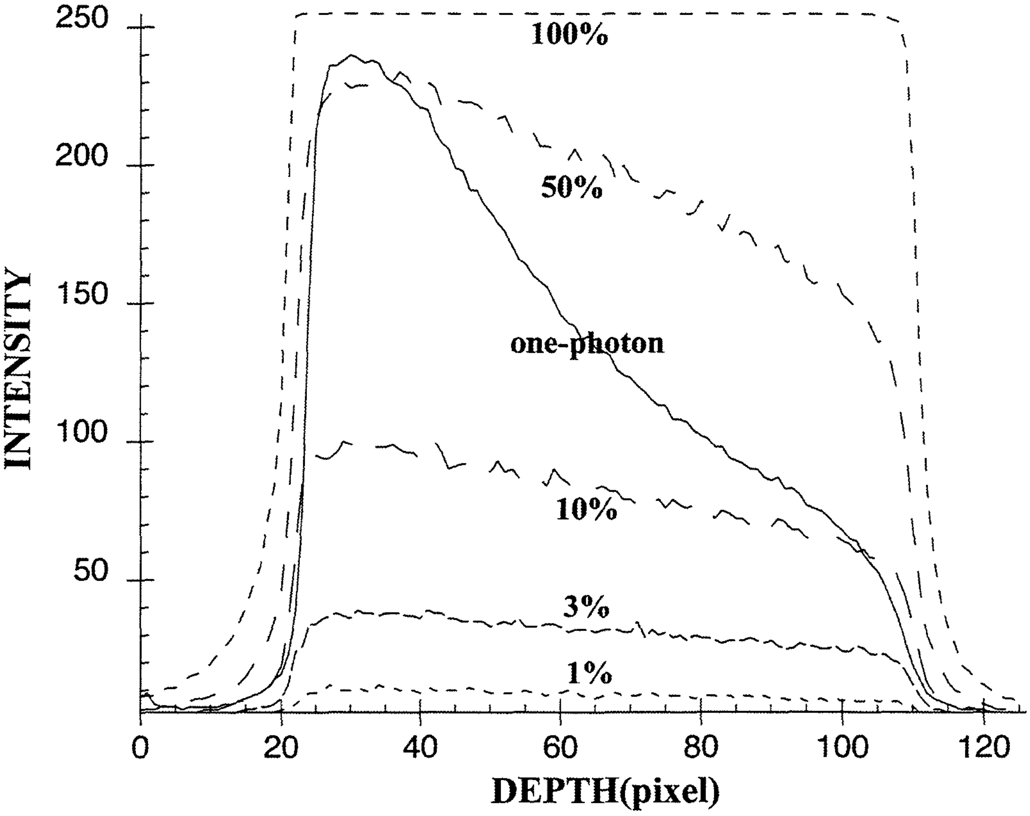

Fig 3.10 Comparison of intensity decay of TPLSM at various excitation intensity and CLSM as a function of imaging depth. TPLSM is shown to have better penetration depth than CLSM.

have even lower decay rates 0.43/pixel, 0.38/pixel, and 0.08/pixel, respectively. The results show that the fluorescence decrease is a linear function of depth per se and high excitation intensities have a higher decay rate. Therefore, low-power illumination, though reducing the image SNR, may result in more homogeneous fluorescence emission at deep tissue imaging around 150 μm deep.

Numerical Aperture

The loss of intensity and resolution in CLSM due to refractive index mismatch between the specimen and the immersion system has been reported (Carlsson, 1991). The mismatch results in spherical aberration and then limits the use of high-NA objectives of CLSM in deep tissue imaging. Because of the increasing interest of using TPLSM in deep tissue imaging, it is worthwhile to investigate this effect with TPLSM.

To study the effect of a refractive index mismatch on TPLSM images, we examined the penetration depth of TPLSM with different NA. Here we took vertical scanning images of an FITC-albumin gel with TPLSM using three objectives (NA 0.22, 0.4, 0.75, air) and plotted the intensity decay as a function of depth. The refractive index of the specimen is about 1.33. Fig. 3.11 shows that the fluorescence intensity is decreased by 38%, 52%, and 62% for NA 0.22, 0.4, 0.75, respectively at 200 μm deep. Therefore, high NA objectives may reduce the capability of deep tissue imaging of TPLSM.

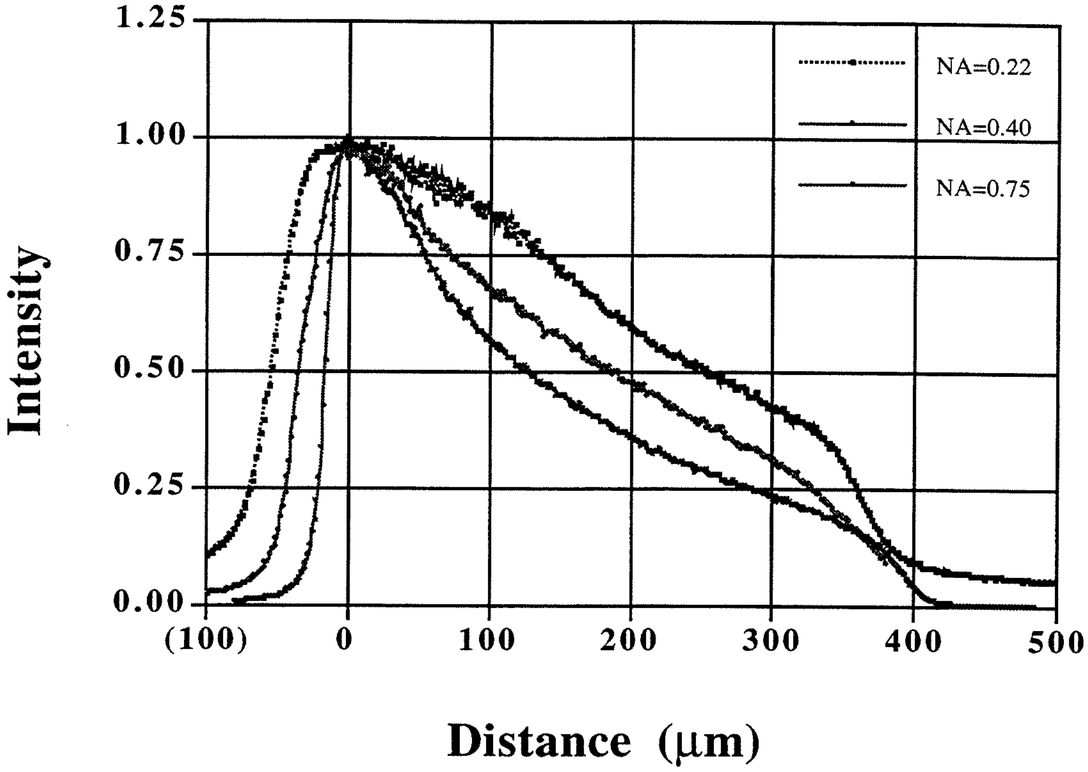

Fig. 3.11 Loss of image intensity as a function of depth with different objectives. A high NA objective results in greater intensity loss.

3.6 ADVANTAGES OF TPLSM OVER CLSM

Major advantages of TPLSM, including less photobleaching and UV imaging capability, have been demonstrated in previous sections. Some practical aspects of TPLSM, such as prices and alignment of the instrument, affect the popularity of TPLSM. Table 6.1 shows the advantages and disadvantages of TPLSM over CLSM.

Pro	Reduced phototoxicity Reduced photobleaching Less cross talk (510DRLP and 670 DCSP) Capable of exciting UV dyes without UV lasers and optics Capable of doing photo-uncaging and photo-bleaching in a diffraction-limit spot No pinhole to align No requirement for alignment of multi-labeled excitation Long penetration depth
Con	Expensive Complicated Scanning speed Not good for infrared-absorbing cells

Tab. 3.3 Advantages and disadvantages of TPLSM over CLSM.

In addition to the major advantages of TPLSM discussed in the previous chapters, the less cross talk is another advantage of TPLSM over CLSM. For CLSM, the excitation and emission spectra are usually overlapped, necessitating the use of a wavelength filter to prevent cross talk. In this way, the fluorescence signals are greatly cut, and the optical transmission efficiency decreases. However, for TPLSM, the excitation and emission spectra are further separated and hence the cross talk is greatly reduced. For example, peaks of one-photon excitation and emission spectra of Fluorescein are 488 nm and 540 nm, respectively. Around 510 nm a large signal loss occurs when using a 510DR long pass filter (Molecule Dynamics) to block the excitation laser beam. However, our TPLSM, using a 670 nm short pass filter, can obtain clear two-photon images at 850 nm and therefore the signal loss due to cross talk is greatly minimized.

In chapter IV, imaging a specimen stained with multiple fluorophores will be shown to provide useful information about 3-D structure and the dynamics of biological molecules. To image a multi-labeled specimen, CLSM usually utilizes multiple wavelengths for acquiring images from different fluorophore. Because refractive index differences depend on wavelength, an alignment is usually required for fluorescence imaging at different wavelengths.

High cost and complicated operations are among the major disadvantages of TPLSM. A Ti-Sapphire laser can cost $100-200K, which limits the widespread use of TPLSM. Although the introduction of single wavelength femto-pulse lasers made the TPLSM less expensive, those TPLSM with fixed wavelengths are, however, useful with a smaller range of fluorophores. In addition, the femto-pulse laser is still not user-friendly technology and TPLSM requires some laser operation skills. The development of technology is expected to overcome these obstacles and make TPLSM more user-friendly in the future.

REFERENCES

Berek, M., 1927, "Grundlagen der Tiefenwahrnehmung im Mikroskop," *Marburg Sitzungs Ber.* **62** 189-223

Carlsson, K., 1991, "The influence of specimen refractive index, detector signal integration, and non-uniform scan speed on the imaging properties in confocal microscopy," *J. Microsc.* **163**: 167-178

Hell, S., Reiner, G., Cremer, C., and Stelzer, E.H.K., "Aberrations in confocal fluorescence microscopy induced by mismatches in the refractive index," *J. Microsc.* **169** 391-405

Inoue, S., 1995,"Foundations of Confocal Scanned Imaging in Light Microscopy," in *Handbook of Biological Confocal Microscopy* 2nd Ed. Pawley J.B. Plenum Press, New York 1-17

Jacobsen, H., Hanninen, P., Soini, E., and Hell, S.W., 1994, "Refractive-index-induced aberrations in two-photon confocal fluorescence microscopy," *J. of Microscopy* **176** (3) 226-230

Sandison, D.R., Piston, D.W., Williams, R.M., and Webb, W.W., 1995, "Quantitative comparsion of background rejection, signal-to-noise ratio, and resolution in confocal and full-field laser scanning microscopes," *Applied Optics* **34** (19) 3576-3588

Sandison, D.R., Williams, R.M., Wells, K.S., Strickler, J., and Webb, W.W., 1995, "Quantitative Fluorescence Confocal Laser Scanning Microscopy (CLSM)," in *Handbook of Biological Confocal Microscopy* 2nd Ed. Pawley J.B. Plenum Press, New York 39-53

Sheppard, C.J.R., and Gu, M., "Image formation in two-photon fluorescence microscopy," *Optik* **86** 104-106

Soeller, C., and Cannell, M.B., 1996, "Construction of a two-photon microscope and optimisation of illumination pulse duration," *Pflugers Archive European J. of Physiology* **432** 555-561

Visser, T.D.,Oud, J.L., and Brakenhoff, G.J., 1992, "Refractive index and axial distance measurements in 3-D microscopy," *Optik,* **90** 17-19

White, N.S., Errington, R.J., Fricker, M.D., and Wood, J.L., "Aberration control in quantitative imaging of botanical specimens by multidimensional fluorescence microscopy," *J. of Microscopy* **181** (2) 99-116

Wilson, T., 1995,"The Role of the Pinhole in Confocal Imaging System," in *Handbook of Biological Confocal Microscopy* 2nd Ed. Pawley J.B. Plenum Press, New York 167-182

CHAPTER IV

IMAGE ENHANCEMENT IN CONFOCAL AND TWO-PHOTON MICROSCOPY

As shown in previous chapters, CLSM and TPLSM can provide great insight into the intricate, three-dimensional (3-D) structure of biological systems by optical sectioning. However, the optical sectioning made possible by CLSM is not without cost; while the confocal aperture (pinhole) is made smaller, the resolution increases, but the signal becomes weaker and shot noise becomes more apparent and consequently the signal-to-noise ratio (SNR) decreases (chapter two). Hence, the resolution and the SNR are two antagonistic and limiting factors in CLSM. Compared to CLSM, TPLSM uses longer excitation wavelengths, which then enlarge its PSF and degrade the resolution.

This limit makes the interpretation of double-stained samples especially difficult because any blurring obscures the distinction in protein localization. An entirely different approach to 3-D microscopy is a computational deblurring (image restoration) of serial sections from a CCD wide field microscope. This image restoration technique was successfully applied to CLSM and TPLSM to achieve improvements in image resolution and fidelity. This method, consistently testing accurately on synthetic and real control images, was used to image double-stained cell cultures from the rat hippocampus, looking at the distributions of PSD-95, Synapsin I, and CaM Kinase II. These enhanced images provide insight into the localization of proteins possibly involved in the regulation of synaptic plasticity.

4.1 MOTIVATION

The mammalian CNS is but one very large field with much to be learned from its intricate microscopic structure. One area of particular interest is that of the hippocampus, a structure thought to be essential for formation of memory, involving neurons that exhibit a form of synaptic plasticity called long-term potentiation, or LTP (see Kennedy, 1989 for a summary). Because of the large number of specific antibodies raised against neuronal proteins, 3-D fluorescent microscopy could be ideal for examining synaptic protein distributions in the hippocampus, but current resolution is inadequate to distinguish between the proteins in the pre- and postsynaptic compartments within individual synaptic contacts. With the motivation to enhance viewing the fine structures of the hippocampus, we sought a means of increasing image resolution and quality. Because point spread function (PSF) plays an important role in the image deconvolution techniques discussed in this chapter, it is worthwhile to review the PSF of WFM, CLSM, and TPLSM briefly.

Wide-field microscopy with a high-resolution CCD camera offers a high signal-to-noise (SNR) ratio. However, its axial resolution is poor because it does not filter out light from out-of-focus planes; therefore, its direct applications in 3-D imaging are limited. CLSM is ideal for 3-D fluorescence imaging because it utilizes optical sectioning to eliminate out-of-focus signals so that clean optical sections are accessible. Hence, by raster scanning the specimen with sequential planes, a detailed 3-D image can be obtained.

Theoretically, the lateral resolution for any light microscope is dictated by the Airy radius:

$$r_{Airy} = 0.61 \frac{\lambda_0}{NA_{obj}}$$

which depends on the wavelength, λ_0, and the numerical aperture of the objective, NA. The theoretical Airy radius is 213 nm with a 63X NA 1.4 oil immersion objective and 488 nm Argon laser illumination. However, the resolution of most fluorescence microscopes is degraded by optical aberrations, non-diffraction-limit illumination, and specimen scattering.

Experimentally, the standard way of characterizing any 3-D microscope's performance is by measuring its point-spread function (PSF), which is equivalent to the impulse response of the microscope. A microscope's PSF is the 3-D image that is obtained if a point-source of light, for example, an extremely small fluorescent bead, is imaged by serial scanning. The ideal PSF of a conventional wide-field microscope is shaped like an hourglass with concentric rings: (1) when focused on the bead, the 2-D image will be that of a point, and (2) as the plane of focus is changed, the bead will blur, at first into a ring, and then into concentric rings (Hiraoka *et al.*, 1990, and Carrington *et al.* 1990). The PSF for a confocal microscope exhibits the same hourglass appearance if the pinhole is left open. As the pinhole is closed, however, the outer edges of the hourglass decrease in brightness, and the PSF becomes a 3-D elliptical solid with its brightest point at the center (Fig. 4.3, and Shaw, 1995). The PSF has a greater extent in the Z-direction than in the X and Y directions, resulting in worse resolution in the axial direction.

TPLSM, utilizing two-photon absorption to limit the excitation volume, does not require the detection aperture to achieve optical sectioning. Due to the simultaneous absorption of two photons, the PSF of TPLSM is, therefore, the square of illumination PSF and does not contain detection PSF (chapter two). Compared to CLSM, for the same chromophore, TPLSM requires a longer illumination wavelength and might have a more extensive PSF (see Fig. 3.4).

With the PSF, a useful model of 3-D imaging can be reconstructed. The assumption is that the PSF is both linear and shift-invariant (this is a fair assumption within a reasonable field of view, see Shaw *et al.*, 1991); therefore, the observed image is the convolution of the true image of the biological sample with the PSF of the microscope. If one could imagine how the ideal, unblurred image looks, replacing the ideal image at each pixel with a PSF of the same intensity would produce the blurred image observed with a microscope. Hence, the smaller a microscope's PSF, the better the resolution will be, because less blurring will occur in the imaging process.

For CLSM, even at its smallest settings, the confocal pinhole cannot entirely remove all of the blur from out-of-focus planes. In other words, the confocal PSF cannot be made infinitesimal. (The most desirable PSF would just be a single voxel, a single volume element in a digital computer.) Furthermore, closing the pinhole reduces the amount of light reaching the detector, resulting in a decreased SNR. Although increasing the number of averaged images might reduce image noise, it is of limited help because it results in increased photobleaching. In addition to photobleaching, saturation of the fluorescent dyes, in which fluorescence emission stops increasing with higher illumination intensity because most dye molecules are in the excited states, limits the total signal that can be acquired. Although high resolution and high SNR are both desirable, in confocal microscopy achieving one compromises the other (Conchello *et al.*, 1994).

Many methods were used to increase the resolution of CLSM and TPLSM. 4-Pi microscopy, utilizing one objective above and one below the stage to collect fluorescent signals, manages to increase the axial resolution by 2-3 fold (Hell et al., 1995). However, this technique requires a very precise alignment which makes imaging tedious and difficult and therefore is not utilized in many biological laboratories.

Image deconvolution of CLSM and TPLSM offers an alternative approach for high resolution 3-D fluorescence imaging by computationally correcting for the microscope's PSF (Carrington, 1990a, Carrington *et al.*, 1990b, and Agard *et al.*, 1989). The goal of the method is to reverse the image forming process; that is, to deconvolve the observed image with the PSF to produce the real image. The fundamental principal is the following: the ideal, unblurred dye-density distribution, when blurred with the PSF, should produce the observed image. Hence, this ideal image can be estimated by iteratively minimizing the difference between the estimated image convolved with the PSF and the observed image. This method has generated images with resolution that rivals or exceeds those from confocal microscopy (Carrington *et al.*, 1995).

Application of the technique of computational image restoration to confocal microscopy has the potential of producing high-quality images by improving images that are already of good quality. The promise of this method has been demonstrated in a variety of applications (Shaw, 1995, van der Voort *et al.*, 1995, Hosokawa *et al.*, 1994). In this chapter, we will reveal its usefulness when applied to double-stained confocal images of rat hippocampal tissue. We examined double-stained tissues because the approach should improve not only the image of each protein's localization, but also the superimposition of the images, offering greater insight into their relative locations. Here, we concentrated on the proteins Synapsin I, Ca^{2+}/calmodulin-dependent Kinase II (CaM Kinase II), and PSD-95 in cultures of rat hippocampal neurons to learn more about their localization, and hence their potential function in synaptic function.

4.2 THEORY OF DECONVOLUTION TECHNIQUES

Image Formation and Point Spread Function

All 3-D images can be described as n-dimensional vectors, where n is the number of data points in the images. For example, an image of size 100 x 80 x 50 (*width* x *height* x *depth*) would be a vector of dimension 100 x 80 x 50 = 400000, where each dimension would correspond to the intensity of a voxel.

Let f = the unblurred "real" image of the biological specimen

g = the observation of the image via CLSM or TPLSM

k = the PSF

$\otimes$ = image convolution

Our imaging model, in the absence of noise, is then:

$$g = k \otimes f \tag{1}$$

This simply states that the observed image will be the unblurred image of the biological specimen convolved with the PSF (Shaw, 1995). This model assumes shift-invariance and linearity. However, additive shot-noise is present in confocal imaging, which takes on the Poisson distribution, or the normal distribution if averaging of frames is performed. Hence, the model becomes:

$$g = k \otimes f + n \tag{2}$$

Therefore, the noise component introduces further image degradation that our restoration procedure must take into account, or else inappropriate deconvolution results will be obtained. One can minimize the contribution of noise by filtering the images with a median filter before performing image restoration. To minimize distortion from noise inherent in image acquisition, we used a nonlinear 3 x 3 x 3 median filter which does the sorting of itself and the neighboring 26 voxels and then replaces the voxel value by the median value of the 27 voxels for each voxel. Other filters, such as a Gaussian or a mean filter, still include noise in the resulting image so do not work as well as a median filter.

Image Deconvolution

We chose to use a constrained version of the Van Crittert iterative technique (Schafer *et al.*, 1981). A short derivation follows.

Let us call our image estimate f '. Our goal is for:

$$f' = f \qquad (3)$$

If we convolve both sides of the equation with the PSF, we get:

$$f' \otimes k = f \otimes k \qquad (4)$$

Substituting equation (1) into (4) (assuming the absence of noise), we get:

$$f' \otimes k = g \qquad (5)$$

This is a system of n equations, where there are n data points in g, that could theoretically be used to solve for f '. However, we must pose the constraint that our estimate f ' must be non-negative because negative intensity would indicate a negative dye concentration, something which is obviously impossible. Hence, we cannot proceed by a direct deconvolution, but must instead seek an iterative solution which minimizes the difference between the left and right hand members of the equation, that is:

$$\text{Minimize } \| f' \otimes k - g \|^2 \qquad (6)$$

Image formation and Deconvolution

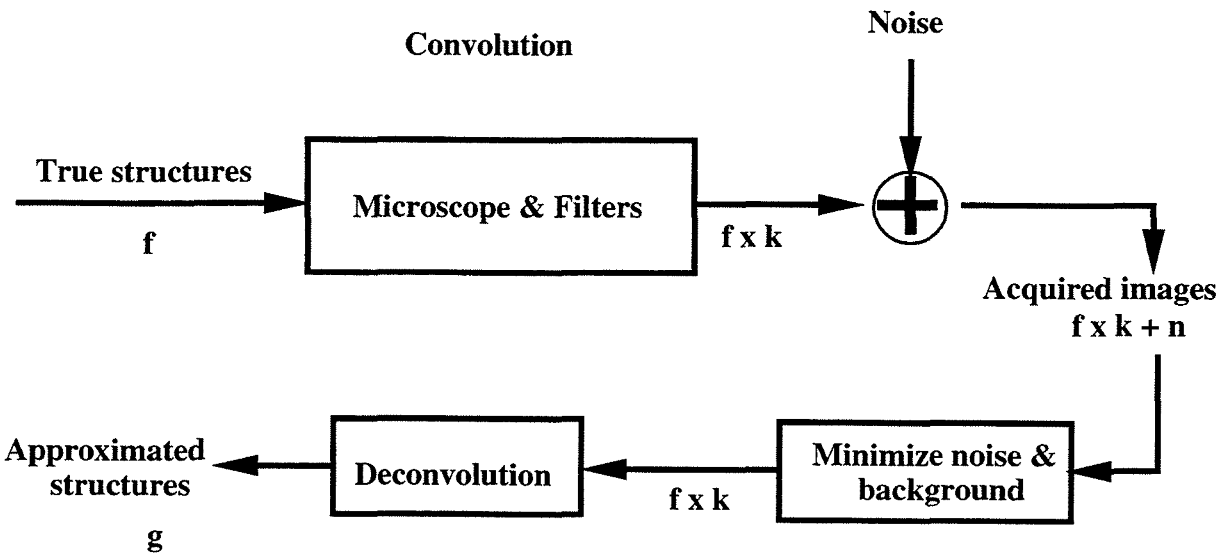

f : true structures
g : approximated structures
k : point spread function
n : noise
x : convolution

Deconvolution:

Minimize $\| f \, x \, k - g \, x \, k \|$

Fig. 4.1 The process of image acquired and image deconvolution. Images are blurred by the imaging system and then deconvolved with the point spread function of the system. A 3x3x3 median filter was used to minimize the image noise.

The iterative procedure by which this equation is minimized is the following:

Start: $$f_0' = g \qquad (7)$$

Iterate: $$f_{k+1}' = f_k' + \lambda\, k^T \otimes (g - k \otimes f_k') \qquad (8)$$

$$= f_k' + \lambda\, k^T \otimes g - \lambda\, k^T \otimes k \otimes f_k'$$

$$f_{k+1}' = T\, P\, (f_{k+1}') \qquad (9)$$

The operator P constrains the estimate at each step to be positive, and T is the boundary constraint which keeps the estimate to be within the original boundaries of the image. λ is a scalar convergence parameter with a range 0 - 2, with 2 offering the fastest convergence. k^T is the transpose of the PSF, which in 3-D space means that $k^T(x,y,z) = k(-x,-y,-z)$. Hence, $k^T * k$, on the right-hand side of (8), is an autocorrelation function, which satisfies the required convergence criteria (Schafer *et al.*, 1981). For speed considerations, all convolutions are performed in the Fourier domain.

After the images are processed with a median filter, the above deconvolution procedure can be carried out to obtain a deconvolved image assuming the noise is negligible. Our tests on synthetic and real control data (Fig. 4.4 and 4.5, respectively) show accurate and consistent performance, comparable to algorithms that account for noise by regularization.

Our approach was to obtain the PSF rather than to use a mathematical model (van der Voort *et al.*, 1995). To measure the PSF, fluorescent beads obtained from Molecular Probes were suspended in an acrylamide gel, with index of refraction 1.34, chosen to closely match the index of refraction of our specimens ($n \approx 1.33$). We took full 3-D images of several beads under identical scanning conditions (laser power, filters, and pinhole size). The individual bead images were median filtered and then aligned by correlation and added together with floating-point precision to construct a composite PSF (Fig. 4.3). Using a measured PSF in this manner gives the algorithm a better estimate of blurring than do mathematical models because it is difficult for models to take into account the subtle variations in the optics that affect the PSF on a daily basis. Adding several beads not only increases the accuracy but also better measures the outer axial tails of the PSF, which is crucial to avoiding artifacts in reconstruction.

4.3 PREPARATION OF TISSUE AND MATERIALS

To measure the PSF independently in the 488 nm and 543 nm channels, yellow-green (490/515) and orange (530/560) fluorescent beads (100 nm diameter; Molecular Probes) were suspended in a 15% acrylamide gel to make the beads stationary. We diluted the 2% solids solution of beads to 1:10000 and added them to 1.6 mL of 30% acrylamide 0.8% bis, 1.6 mL dH20, 10 μL APS 0.1g/mL (0.1 g Ammonium Per-Sulfate dissolved in 1 mL dH20), and 3 μL TEMED. The solution was vortexed, and before the acrylamide hardened we placed about 100 μL into a clean depression slide, and sealed it with a #1 40 mm coverslip.

Dissociated hippocampal cells from day 18 rat embryos, cultured on a glass coverslip for about 3 weeks, were fixed in methanol at -20 °C. The antibody incubation was done as previously described (Cho et al.,1992). The cultures were incubated with one of the following primary antibodies at 4 °C overnight in Triton buffer (0.02M phosphate {pH 7.4}, 0.45M NaCl, 0.05% triton X-100, 5% normal goat serum): a 1:1000 dilution of polyclonal anti-synapsin I from rabbit (Collette), a 1:1000 dilution of polyclonal anti-synapsin from mouse, 10 gm/mL of affinity purified polyclonal anti-PSD95 (Frances), or a 1:500 dilution of mouse monoclonal anti-CaM Kinase II (6G9). After rinsing (3 x 15 minutes), tissues were exposed to the appropriate secondary antibodies (Cappel fluorescein-conjugated anti-mouse or anti-rabbit IgG or Chemicon Cy3 conjugated anti-mouse or anti-rabbit IgG) for one hour at room temperature at a 1:100 dilution. They were then post-fixed with 2% formaldehyde in PBS, before being coverslipped. Samples were incubated with primary and secondary antibodies and then mounted in an osmotically-neutral buffer of sodium bicarbonate (pH 9) with an index of refraction compatible with the acrylamide.

All images were acquired from a Zeiss 310 confocal microscope. A 488 nm Argon laser beam was used for obtaining fluorescein fluorescence and 543 nm He-Ne laser beam for Cy3 fluorescence. The pinhole size was 35 μm. PSFs were obtained separately for each channel to account for the differences resulting from the different wavelength and filter sets. We sampled with 100 nm x 100 nm x 200 nm voxel size, with a larger z-voxel spacing because z-resolution should be unaffected while photobleaching should be halved. For 2-channel series acquisition, a macro was written so both the argon-laser-illuminated image and the He-Ne-laser-illuminated image were acquired before the stage was moved to the next focal plane. Contrast and brightness were adjusted to maintain a non-zero baseline and avoid saturation. All computation and image processing were done on Silicon Graphics 4D VGX and Indigo 2 computers. Programming of the algorithm was done in the C language. 3-D and 2-D renderings were performed with Voxel View 2.5, and images were transferred to a Photoshop 3.0 for printing. Statistical analyses were done using Microsoft Excel. P-values less than 0.05 were considered significant.

IMAGE RESTORATION OF DUAL-STAINED HIPPOCAMPAL CULTURE CELLS WITH LASER SCANNING MICROSCOPY

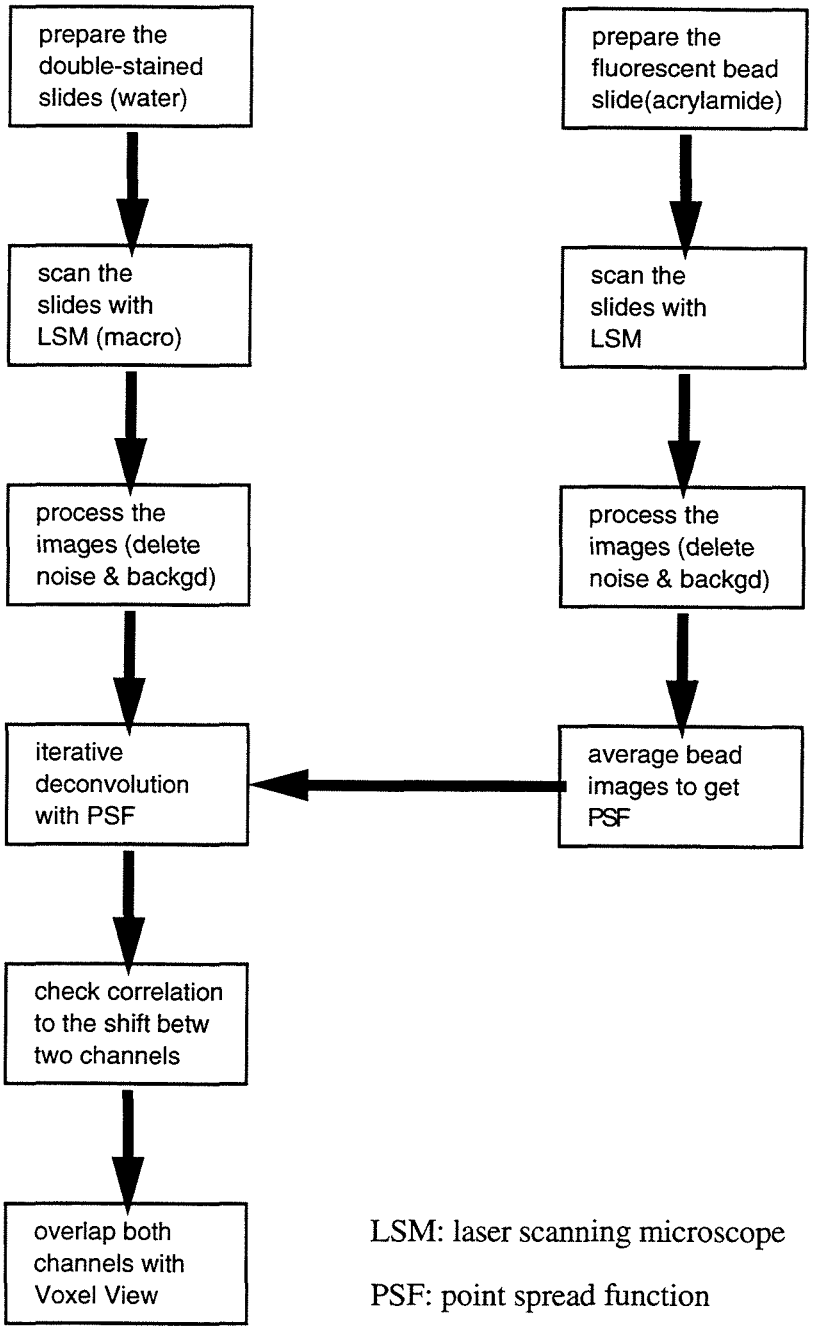

LSM: laser scanning microscope

PSF: point spread function

Fig. 4.2 The flow chart of image deconvolution process of imaging double stained hippocampal cells with laser scanning microscopy.

4.4 IMAGE DECONVOLUTION OF CONFOCAL MICROSCOPY

Dense beads

To determine the theoretically highest resolution that could be obtained and verify the accuracy of the algorithm, we processed synthetic images using the real PSF of the confocal microscope with a pinhole size of 35 μm. (See Fig. 4.3) To determine lateral and axial resolution, we created artificial images with a voxel size of 100 nm x 100 nm x 100 nm containing two point sources separated by varying distances in the lateral or axial planes. They were then convolved with the real PSF, and the algorithm was used to deconvolve the image to test its ability to resolve the two point sources (Fig. 4.5). We found that without image restoration, the smallest distances that could be clearly resolved were approximately 400 nm in the image (lateral) plane and 1400 nm along the optical axis. Obviously this is larger than what might be expected from the Raleigh criterion for confocal microscopes (213 nm laterally), but for our purposes it is much more relevant because it reveals the practical limits imposed by the real PSF. After image restoration, we could resolve 200 nm laterally and 400 nm axially, demonstrating a significant resolution increase, especially along the optical axis.

To further establish the validity of the procedure, we processed real images of 100 nm fluorescent beads suspended in acrylamide (Fig. 4.4). The procedure enhanced the separation and definition of all the beads in the image in a consistent manner, and no spurious image details were created. This verifies that our approach produces reliable improvement on real, high-resolution confocal data.

Fig. 4.3 PSF of a Zeiss 310 confocal microscope

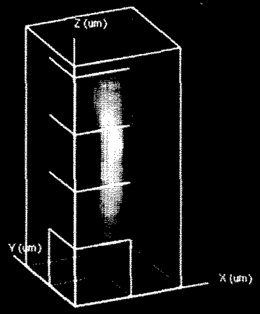

Fig. 4.4 Image Deconvolution of Dense Fluorescent Beads

Blurred

Restored

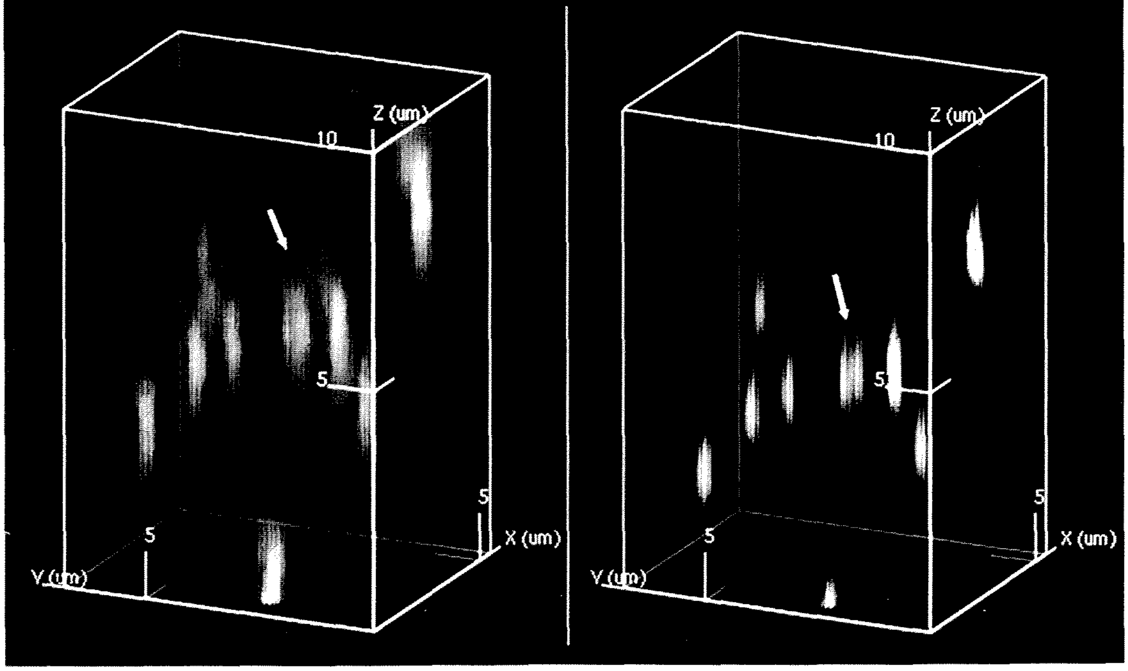

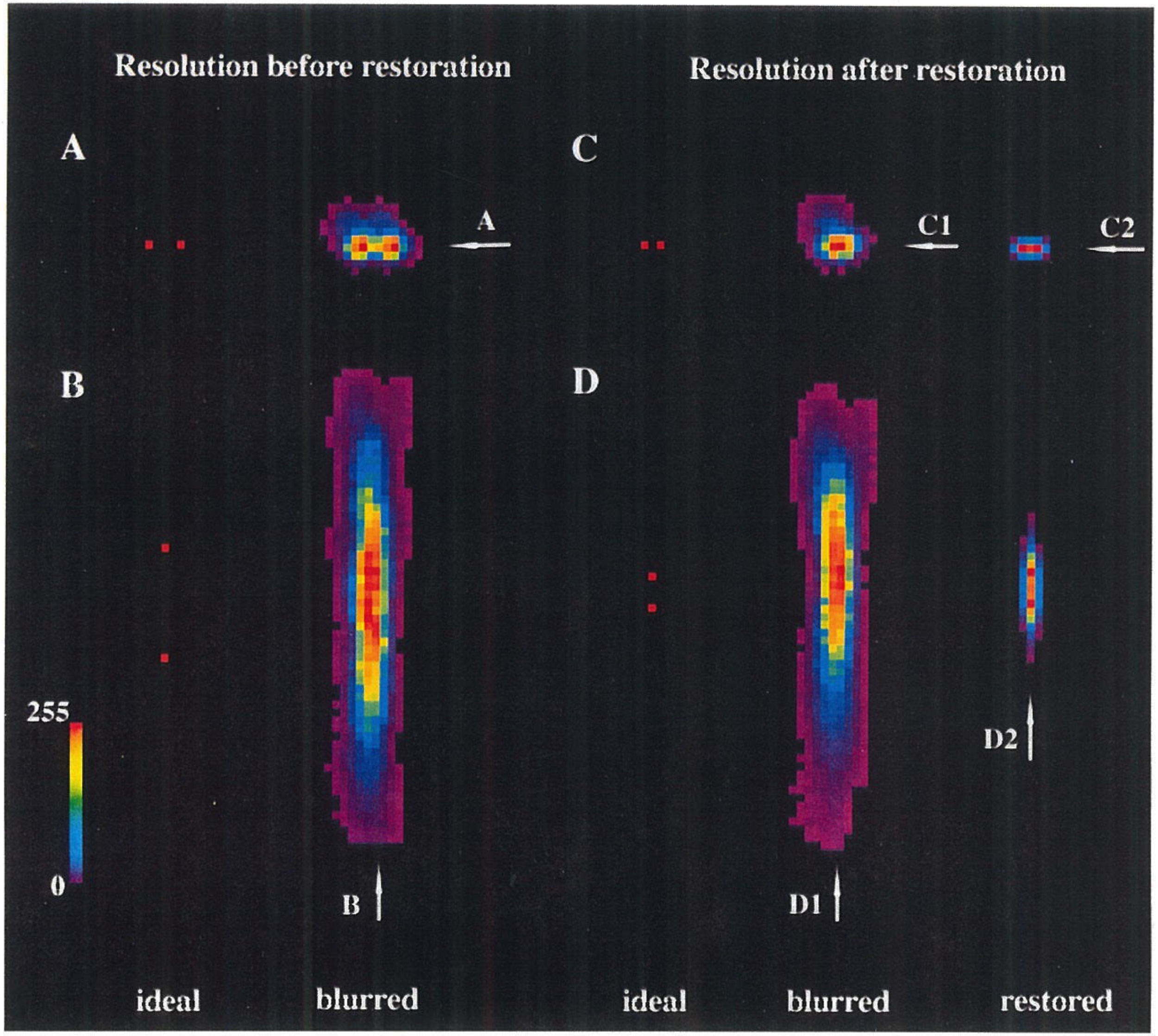
Resolution before restoration
Resolution after restoration
A
C
A
C1
C2
B
D
255
0
B
D1
D2
ideal
blurred
ideal
blurred
restored

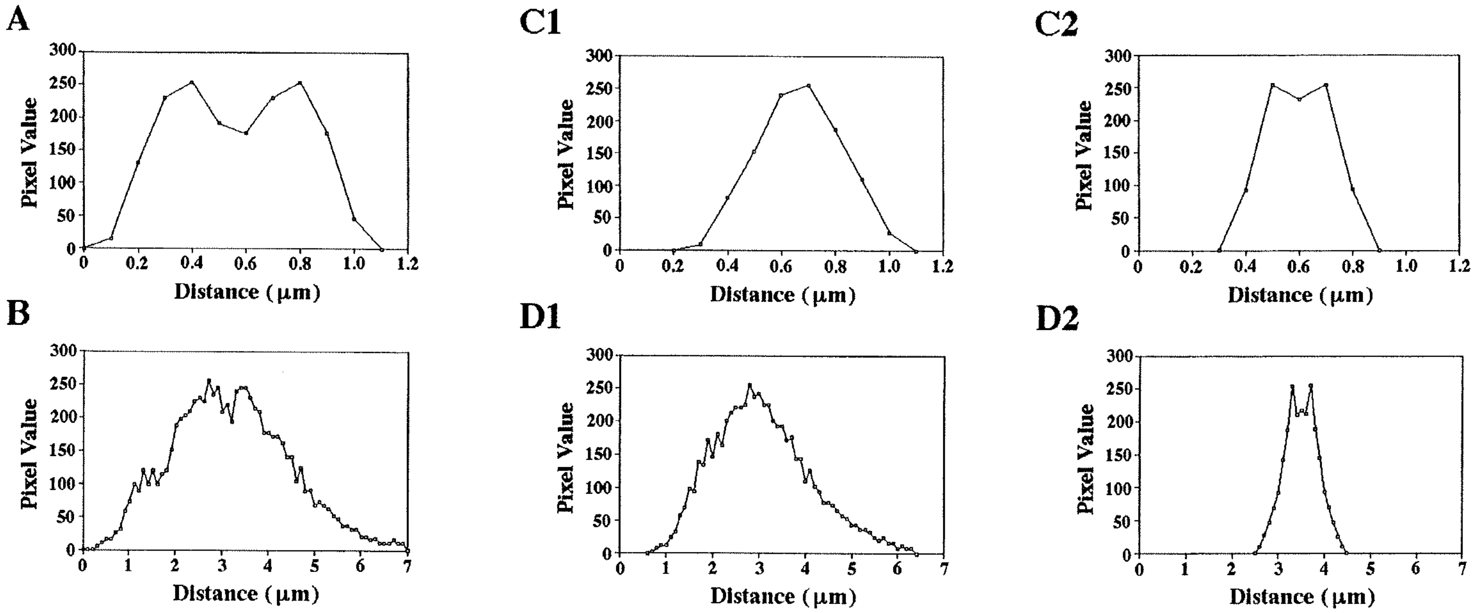
A
Pixel Value
300
250
200
150
100
50
0
0
0.2
0.4
0.6
0.8
1.0
1.2
Distance (µm)
B
Pixel Value
300
250
200
150
100
50
0
0
1
2
3
4
5
6
7
Distance (µm)
C1
Pixel Value
300
250
200
150
100
50
0
0
0.2
0.4
0.6
0.8
1.0
1.2
Distance (µm)
D1
Pixel Value
300
250
200
150
100
50
0
0
1
2
3
4
5
6
7
Distance (µm)
C2
Pixel Value
300
250
200
150
100
50
0
0
0.2
0.4
0.6
0.8
1.0
1.2
Distance (µm)
D2
Pixel Value
300
250
200
150
100
50
0
0
1
2
3
4
5
6
7
Distance (µm)

Fig. 4.3 PSF of a Zeiss Confocal Laser Scanning Microscope with a 63X oil-immersion NA 1.4 lens (Zeiss), rendered with Voxel View. The length of the PSF is larger than its diameter, indicating axial resolution is poorer than lateral resolution. Axes marks are 1 mm apart. Pinhole size is 35 μm.

Fig. 4.4 A 3-D rendered image of fluorescent beads, before (left) and after (right) 150 iterations of image restoration. The arrows show that this algorithm successfully resolved two beads of a real sample.

Fig. 4.5 Comparison and simulation of Images Before and After Restoration.
(A) The lateral resolution before restoration is about 400 nm, using the Raleigh criteria. The left image is a single horizontal 2-D slice of a 3-D image containing two point sources laterally separated by 400 nm with a voxel size of 100 nm. When convolved with the PSF from Fig. 4.3, this slice becomes blurry as depicted in the pseudo-color on the left image, and with the mid-point observable as a valley, the two points are still distinguishable. The profile is shown in graph A.
(B) The axial resolution is found to be 1400 nm in the same way as in (A).
(C) The left picture is a single horizontal 2-D slice of a 3-D image containing two point sources laterally separated by 200 nm. When convolved with the PSF from Fig. 4.3, this slice becomes blurry as depicted in the middle image, and distinction between the points is lost. Restoration of this middle 3-D image results in the slice at the right, and the points are again distinct. The profiles indicated by the arrows along the middle (blurred) and right (restored) slices are shown in graphs C1 and C2 figure, respectively. 1000 iterations were used.
(D) The same procedure applied axially yields an axial resolution of 400 nm.

Application to Double-Stained Cultures

Most studies of protein localization, specifically whether a protein is presynaptic or postsynaptic, have relied on painstaking procedures, such as EM studies from synaptosomes or biochemical analysis. What is lacking is an approach for high-quality direct imaging of protein localization in samples that closely resemble *in vivo* conditions. Confocal microscopy of fixed hippocampal cell cultures should theoretically provide a means to observe protein involvement in synapse structure; however, for reasons specified above, the separation of synaptic components is beyond the resolution of confocal microscopy. Hence, we sought to apply the technique of image restoration to double-stained rat hippocampal cell cultures in order to push this resolution limit and better define synaptic protein distributions.

Synapsin I-Synapsin I Control

A double-stained specimen in which fluorescein (green) and Cy3 (red) secondary antibodies were both used to recognize primary antibodies to the same protein, Synapsin I, was used as a control set. Synapsin I is a protein known to be localized to the cytosolic surface of synaptic vesicles, hence should localize to the presynaptic side of the synapse. Because both the fluorescein and Cy3 labels are directed to the same protein, the overlap of the two channels should be exact both before and after image restoration. In reality, this control procedure serves as a calibration tool in two ways:

1) It can be used to quantify how much of an effect the different optics have in altering the channel alignment. The alignment of the two lasers, the focusing of their beam expanders and the different wavelengths of light could cause a refractive shift along the z-axis throughout the field. We computed the correlation of the 3-D images from both channels and found that an axial shift of 200 nm would result in optimal overlap (Pratt,

1991). We made this correctional shift for the data in Fig. 4.6, 4.7, and 4.8, which were all acquired in the same session.

2) It can be used to establish the minimum significant difference between images. The red and green channels in this control should ideally superimpose exactly to form a yellow image. The 3-D rendered images in Fig. 4.6 show that the superimposition is in fact very close both before and after image restoration. In particular, the synapses, which contain the proteins of interest in this study, show an almost exact overlap. However, it is not completely perfect, as small amounts of green are observable unaccompanied by red, both before and after image restoration. This uncertainty presumably arises from subpixel misalignment, imperfect staining and nonlinearities in image formation. Separations between two labeled protein distributions must be significantly greater than in this control in order to be judged as separate.

Fig. 4.6 3-D Rendering of Synapsin I-Synapsin I double-stained control before (left) and after (right) 200 iterations of image restoration. Green indicates fluorescein channel, red Cy3, and yellow overlap, with the panel showing the color arrangement. The white bar is 1 micron in size. Views are (a) from above, (b) zoomed in on the white boxed section of (a). The blue square shows an example of an ROI used in the quantitative comparison. The two channels show almost perfect overlap, so these images can be used as a control in our observation of separation in the other image sets.

Fig. 4.7 3-D Rendering of CaM Kinase II (fluorescein/green) and Synapsin I (Cy3/red) double-stain, with the same views as in Fig. 4.6. The two channels are much better separated compared to Fig. 4.6, especially after image restoration, indicating that CaM Kinase II is in the post-synaptic compartment while Synapsin I is in the pre-synaptic.

Fig. 4.6 Synapsin I / Synapsin I images before and after deconvolution

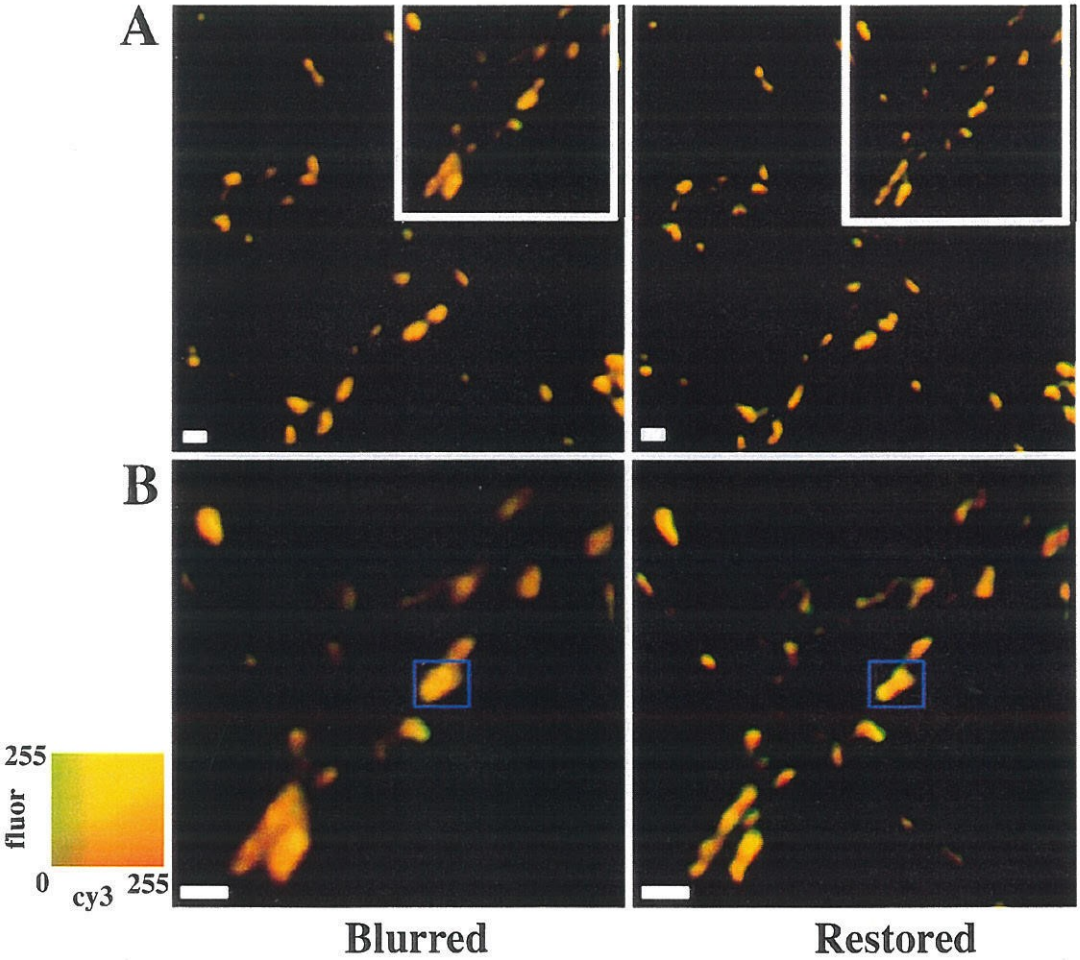

Fig. 4.7 CaM Kinase II / Synapsin I images before and after deconvolution

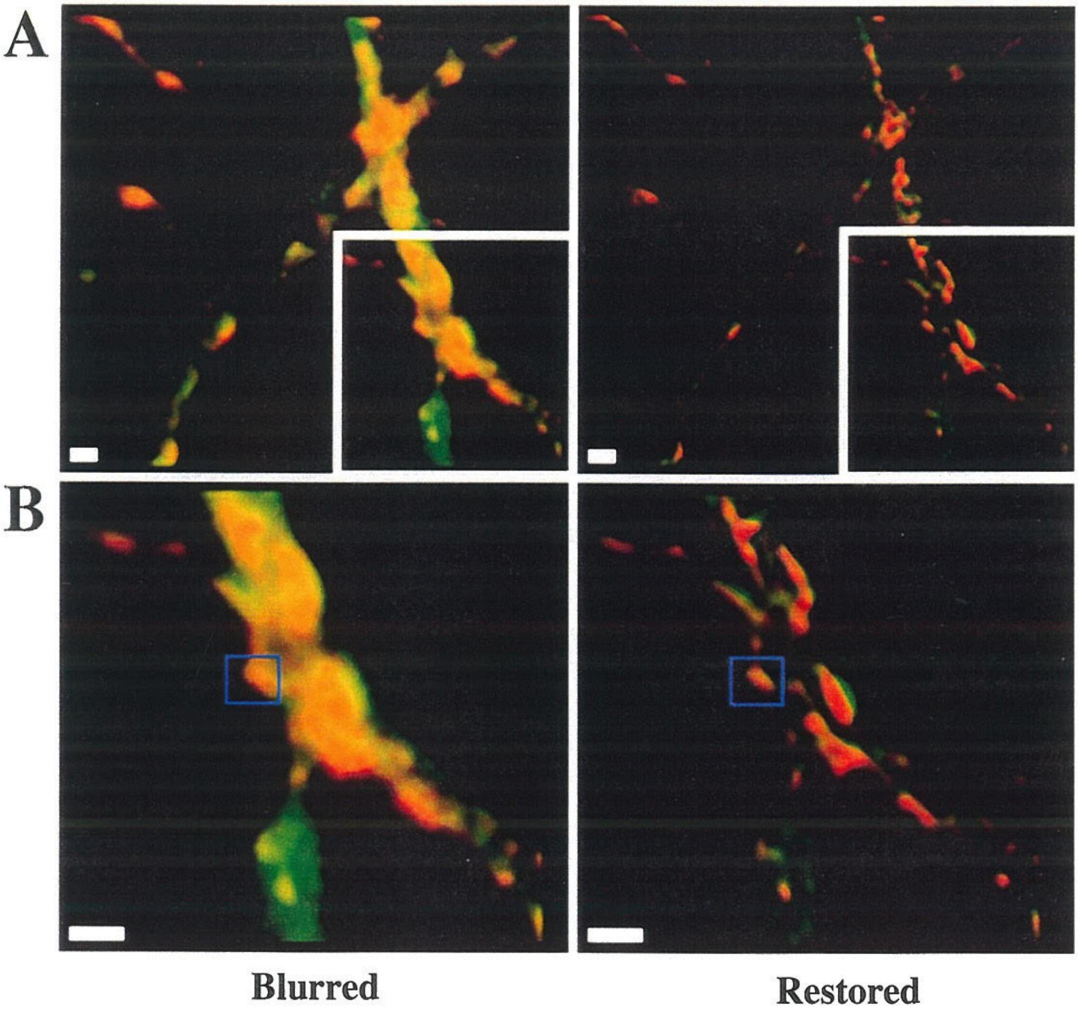

Fig. 4.8 PSD-95 / Synapsin I images before and after deconvolution

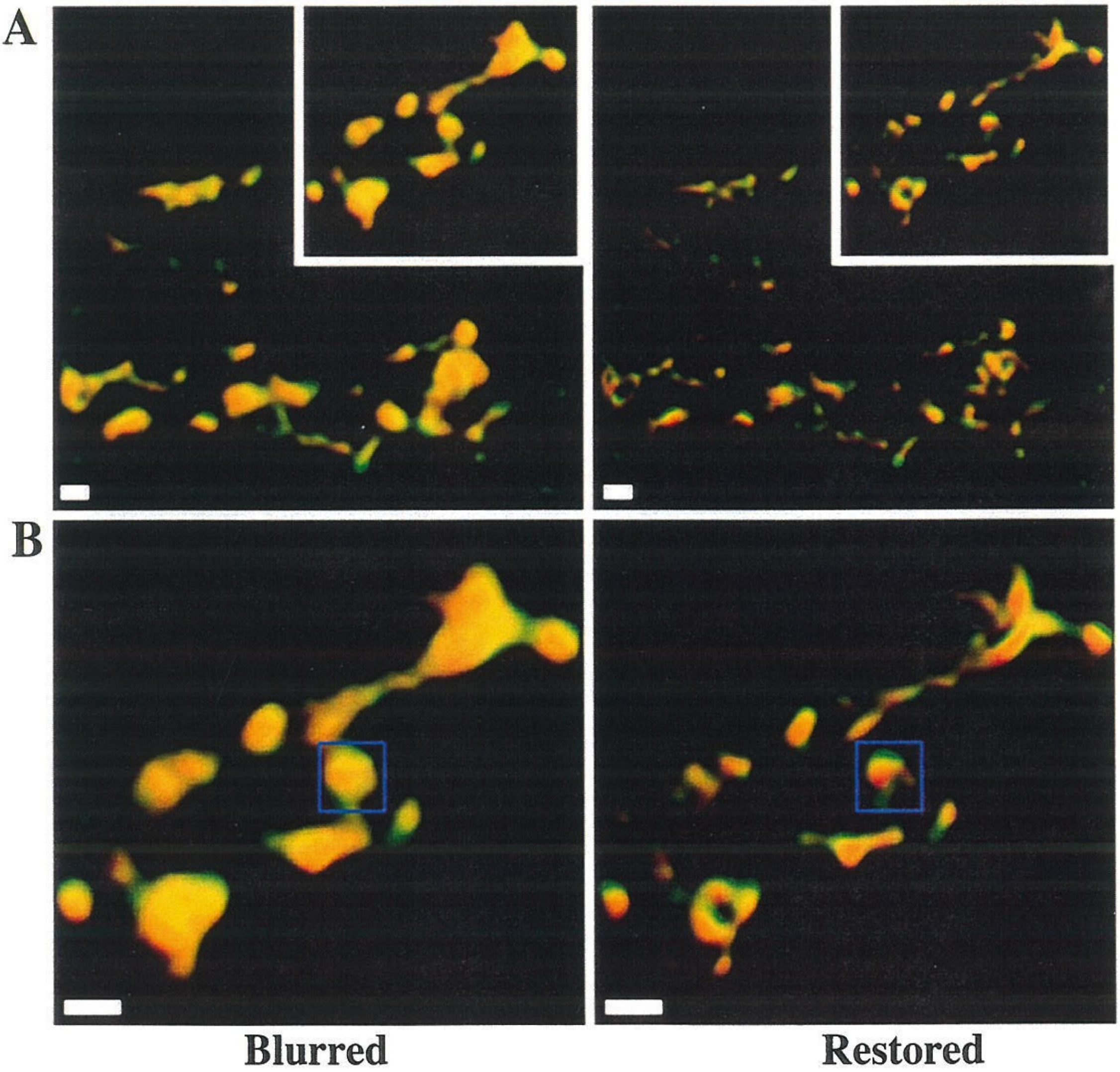

Blurred

Restored

Fig. 4.8 3-D Rendering of PSD-95 (fluorescein/green) and Synapsin I (Cy3/red) double-stain, with the same views as in Fig. 4.6. Again, the two channels are better separated compared to Fig. 4.6, especially after image restoration, but the separation is not as good as in Fig. 4.7 (synapsin I-CaM Kinase II). This suggests that the distance between PSD-95 and synapsin I is less than that between CaM Kinase II and synapsin I, that is, that PSD-95 is more restricted to the synaptic junction than is CaM Kinase II.

To make a quantitative comparison of synaptic staining, we numerically analyzed the overlap of the red and green staining at individual synapses both before and after image restoration. We selected regions-of-interest (ROIs) in the double-stained image which contained one synapse or an inseparable clump of synapses, and calculated the normalized dot product between the two channels both before and after image restoration. An example ROI is shown as the dotted square in Fig. 4.6, 4.7, and 4.8. If we denote A as one n-dimensional vector corresponding to the 3-D image of a synapse from one channel, and B as the vector from the other channel, the normalized dot product is $A \bullet B / (\| A \| \| B \|)$, that is the dot product divided by the product of the norms. Hence, a product of 1 indicates perfect overlap, whereas 0 indicates no overlap. With 19 synaptic ROIs in the synapsin I -synapsin I control, the mean of the normalized dot products was 0.970 ± 0.010. Thus, the overlap was nearly complete with a small amount of variation, which is attributable to the previously mentioned uncertainties inherent in image collection and alignment. Image restoration enhances the subtle differences between the channels in the control, resulting in a lower normalized dot-product with a greater standard deviation; (0.921 ± 0.029 for the same 19 synapses). Therefore, we can use this computation as a statistical tool in making comparisons within but not between the before and after image restoration categories. Table 1 summarizes such results for all data sets processed.

		Before Restoration	After Restoration
		Mean Normalized Dot Product	Mean Normalized Dot Product
	ROI number	(mean ± STD)	(mean ± STD)
Synapsin I	19	0.970 ± 0.010	0.921 ± 0.029
CaM Kinase II	19	0.960 ± 0.017**	0.828 ± 0.074 ***
PSD-95	25	0.971 ± 0.014*	0.891 ± 0.045 **

Tab. 4.1 A Quantitative Comparison of Image Superimposition with Synapsin I

(* $p > 0.1$; ** $0.001 < p \leq 0.01$; *** $p < 0.001$)

N indicates the number of synapses or synaptic regions sampled in each image. The mean and standard deviation of the normalized dot products of the two image channels for these regions were computed. The p-value is given for the one-tailed t-test comparing two normally distributed means (CaM Kinase II / PSD-95 with the synapsin I control) with unknown variances that are assumed equal.

CaM Kinase II-Synapsin I

CaM Kinase II, one of the post-synaptic enzymes, is thought to be activated by calcium entry through NMDA-glutamate receptors and be concentrated in postsynaptic spines (the postsynaptic component of the synapse which projects from the dendrite) and associated dendrites in the rat hippocampus. Fig. 4.7 contains rendered images of synapsin I in red and CaM Kinase II in green; yellow regions indicate overlap. In both restored and unrestored cases, the distinction between the two protein stains is clearly greater than that of the controls. Before restoration, the mean normalized dot product was 0.960 ± 0.017 for 19 ROI, significantly less than the synapsin I control ($p = 0.011$). After image restoration, the image is noticeably more distinct, and the mean dot product is

0.828 ± 0.074 ($p = 5.6 \times 10^{-6}$). The standard deviation of the dot product is much greater after image restoration indicating the distinct differences between the two labels of varying amounts increases after restoration. Thus, image restoration results in a visual and quantitative improvement in the comparison of synapsin I with CaM Kinase II.

PSD-95-Synapsin I

Fig. 4.8 shows a double-stain of Synapsin I in red and the protein PSD-95 in green. PSD-95 is a protein of the postsynaptic density that anchors NMDA receptors and perhaps other postsynaptic proteins (Cho *et al.*, 1992, Kornau *et al.* 1995, 1997). Immunogold electron microscopy of synaptosomes shows it is located almost exclusively at the postsynaptic density (Hunt et al., 1996). In our double-stained images, the distinction between the presynaptic marker (Synapsin) and PSD-95 is much less evident than that for CaM Kinase II; nevertheless, it is still significant. Before restoration, the mean normalized dot product was 0.971 ± 0.014 for 25 synapses ($p = 0.4$ in comparison with Synapsin I : Synapsin I). After image restoration, the mean dot product was 0.891 ± 0.045, ($p <0.01$) The difference is not as great as that between CaM Kinase II and Synapsin I, suggesting that PSD-95 occupies a location much closer to Synapsin I than does CaM-Kinase II. Only with image restoration can the subtle distinction between Synapsin I and PSD-95 become visually apparent and statistically significant.

4.5 IMAGE DECONVOLUTION OF TWO-PHOTON MICROSCOPY

Simulation

From the previous chapters TPLSM has shown to have many advantages over CLSM such as low photobleaching and phototoxicity. However, the resolution of TPLSM is degraded due to long excitation wavelengths. Therefore, it is ideal to combine TPLSM and deconvolution techniques to investigate biological systems non-invasively with high lateral and axial resolution.

To investigate the improvement our deconvolution procedure can achieve with TPLSM, we employed the same deconvolution procedure with TPLSM. These images were convolved with the TPLSM-acquired PSF, and the deconvolution program was utilized to resolve the blurred images to two-voxel images. The results show that before restoration, the smallest distances at which two-voxel images can be resolved are about 500 nm laterally and 1440 nm axially; however, after restoration, the lateral resolution is improved from 500 nm to 320 nm, and the axial resolution from 1440 nm to 900 nm (see Fig. 4.9).

Application to hippocampal cell images

Because of its reduced photobleaching, TPLSM is ideal for visualizing fluorescein-tagged synapsin in presynaptic compartments. Due to the resolution limit, TPLSM can not completely resolve the finest details of the 3-D images, so the image-deconvolution techniques were applied to these images in an attempt to improve the resolution.

Fig. 4.10 shows the hippocampal cell image comparison between the images before and after deconvolution. The cell culture, stained with fluorescein, was imaged with our TPLSM with a Zeiss 63X oil (NA 1.4) objective at 850 nm. Blurring was reduced and many details that were previously invisible appeared. The results show that this technique can improve the resolution and visibility in TPLSM. Combining deconvolution techniques with TPLSM, we are able to observe biological systems with less photobleaching and higher resolution. In the future, the PSF images of TPLSM in deep tissue will help improve the image resolution and reduce optical aberration in highly scattered media and provide valuable information about biological structures and dynamics in deep tissue.

Fig. 4.9 Deconvolution of fluorescent bead images

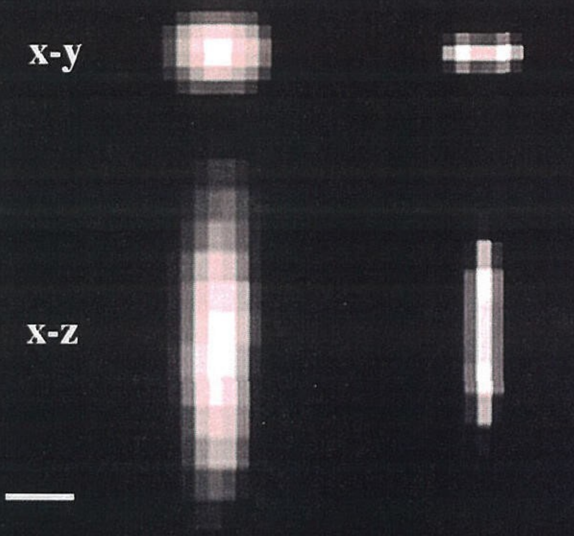

Blurred Restored

Fig. 4.10 Deconvolution of hippocampal cell images

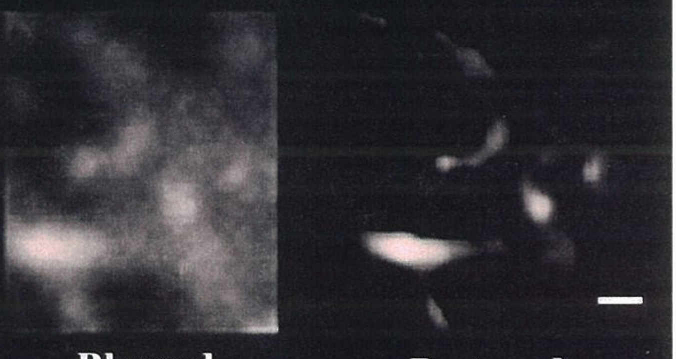

Blurred Restored

Fig. 4.9 Two-voxel images before and after restoration. The blurred images (left) are the convolution of the PSF of TPLSM and two voxels. The restored images (right) were obtained by deconvolving the blurred images with the PSF. The distances between the two voxels are 240 nm laterally (x-y) and 540 nm axially (x-z). The scale bar is 500 nm long.

Fig. 4.10 Fluorescein-tagged synapsin in presynaptic compartments of cultured hippocampal neurons before and after restoration. The restored image (right) was obtained by deconvolving the acquired image with the 3-D PSF. The scale bar is 1000 nm long.

4.6 COMPARING DECONVOLUTION TECHNIQUES OF CONFOCAL AND TWO-PHOTON MICROSCOPY

	Resolution Improvement	
	Before Deconvolution	After Deconvolution
CLSM	400 nm (lateral) 1400 nm (axial)	200 nm (lateral) 400 nm (axial)
TPLSM	500 nm (lateral) 1440 nm (axial)	320 nm (lateral) 900 nm (axial)

Tab. 4.2 Resolution comparison of CLSM and TPLSM before and after image deconvolution.

Table 4.2 shows that CLSM, after deconvolution, provides better resolution than TPLSM. This is an ideal case which applies only to the cell/tissue surface. TPLSM is believed to render better resolution when imaging deeper into the tissue due to less scattering of longer excitation wavelengths. It also shows that deconvolution techniques can provide up to three-fold resolution improvement for CLSM. However, CLSM suffers from the signal loss due to more photobleaching than TPLSM, which may not depict the point spread function as precisely as TPLSM. Thus, deconvolution techniques with TPLSM should provide more accurate depiction of the original image than that with CLSM. The quantitative comparison is yet to be investigated.

4.7 DISCUSSION

In this chapter we described how we utilized image restoration to increase the resolution of confocal microscopy, and by doing so opened a window to applications formerly beyond the resolution of light microscopy. We tested the method on synthetic and real control data sets, finding a practical resolution improvement of up to 200 nm laterally by 400 nm axially. This algorithm, like all that solve inverse problems, requires good initial data: the PSF must be carefully measured with several beads to minimize restoration artifacts, and the sample to be restored must have a reasonable SNR so that the algorithm has a good starting point. With these requirements met, this technique can be used for a wide range of high resolution 3-D imaging applications, including other proteins of the hippocampus and other parts of the brain, slice preparations from adult tissue, and even *in vivo* preparations.

Restoration of double-stained images poses the particular problems of channel alignment and quantitative image comparison. We addressed the alignment problem with a standard correlation procedure, and the quantitative comparison by focusing on the elements of interest in the image, namely, the synapses. Thus, we were able to show visually and quantitatively the differences in synaptic distributions of three proteins in rat hippocampal culture synapses. The conclusion of this work is that deconvolution of light microscopy images can be applied to study very small structures such as synapses. Specifically, the data shows that PSD-95 is more restricted to the synaptic junction than is CaM Kinase II, possibly suggesting the structural importance of PSD-95 in the postsynaptic cleft. Both are primarily localized at the synapse itself, but CaM Kinase II is concentrated at a greater mean distance from the synaptic junction. The qualitative conclusions agree with the previous EM findings, showing the reliability of this method.

The biological impact of this method of imaging is better visualization of protein distributions, with resulting implications for function. We have shown that it delivers more direct high-resolution evidence on the localization of proteins with respect to the synapse. This method offers the promise of *in vivo* high-resolution imaging using fusion proteins with the fluorescent protein GFP, for example. Because this is not possible via electron microscopy, this approach should offer invaluable insights into the dynamic nature of biological systems. Future applications include other proteins of the synapse, and subpixel restoration methods.

REFERENCES

Agard, D.A., Hiraoka, Y., Shaw, P.J., and Sedat, J.W. 1989, "Fluorescence microscopy in three dimensions," *Methods Cell Biol.* **30**: 353-378

Carrington, W.A., Lynch, R.M., Moore, E.D.W., Isenberg, G., Fogarty, K.E., and Fay, F.S. 1995, "Superresolution Three-Dimensional Images of Fluorescence in Cells with Minimal Light Exposure," *Science* **268**: 1483-1487

Carrington, W.A. 1990, "Image restoration in 3D microscopy with limited data," *SPIE* **1205:** 72-83

Carrington, W.A., Fogarty, K.E., and Fay, F.S. 1990, "3D Fluorescence Imaging of Single Cells Using Image Restoration," In *Noninvasive Techniques in Cell Biology* (Foskett and Frinstein, Eds.), pp. 53-72. A.R. Liss, New York

Cho, K.O., Hunt, C.A., and Kennedy, M.B. 1992, "The Rat Brain Postsynaptic Density Fraction Contains a Homolog of the Drosophila Discs-Large Tumor Suppressor Protein," *Neuron* **9**: 929-942

Conchello, J.-A., Kim. J.J., and Hansen, E.W. 1994, "Enhanced three-dimensional reconstruction from confocal scanning microscope images. II. Depth discrimination versus signal-to-noise ratio in partially confocal images," *Applied Optics* **33** (17): 3740-3750

Hiraoka, Y., Sedat, J.W., and Agard, D.A. 1990, "Determination of three-dimensinoal imaging properties of a light microscope system: Partial confocal behaviour in epifluorescence microscopy," *Biophys. J.* **57**: 325-333

Hosokawa, T., Bliss, T.V.P., and Fine, A. 1994, "Quantitative Three-Dimensional Confocal Microscopy of Synaptic Structures in Living Brain Tissue," *Microscopy Research and Technique* **29**: 290-296

Hunt, C.A., Schenker, L.J., and Kennedy, M.B. 1996, "PSD-95 is Associated with the Postsynaptic Density and Not with the Presynaptic Membrane at Forebrain Synapses," *Journal of Neuroscience* **16**(4): 1380-1388

Kennedy, M.B. 1989, "Regulation of Synaptic Transmission in the Central Nervous System: Long-Term Potentiation," *Cell* **59**: 777-787

Kornau, H.C., Seeburg, P.H., and Kennedy, M.B. 1997, "Interaction of ion channels and receptors with PDZ domain proteins," *Current Opinion in Neurobiology* **7**:368-73

Kornau, H.C., Schenker, L.T., Kennedy, M.B., and Seeburg, P.H. 1995, "Domain Interaction Between NMDA Receptor Subunits and the Postsynaptic Density Protein PSD-95," *Science* **269**:1737-40

Pratt, W.K. 1991, "Image Detection and Registration," in *Digital Image Processing, 2nd edition.* pp. 651-673. John Wiley & Sons, Inc., New York

Schafer, R.W., Mersereau, R.M., and Richards, M.A. 1981, "Constrained Iterative Restoration Algorithms," *Proceedings of the IEEE.* **69** (4): 432-450

Shaw, P.J., and Rawlins, D.J. 1991, "The Point-Spread Function of a Confocal Microscope: Its Measurement and Use in Deconvolution of 3-D Data," *Journal of Microscopy, The Royal Microscope Society.* **163**: 151-65

Shaw, P.J. 1995, "Comparison of Wide-Field/Deconvolution and Confocal Microscopy for 3D Imaging," in *Handbook of Biological Confocal Microscopy* (J. B. Pawley, Ed.) pp. 373-387. Plenum Press, New York

van der Voort, H.T.M., and Strasters, K.C., 1995, "Restoration of confocal images for quantitative image analysis," *Journal of Microscopy* **178** (2): 165-181

CHAPTER V

IMAGE DEGRADATION DUE TO BRAIN TISSUE SCATTERING

5.1. INTRODUCTION

In this chapter we report our investigation concerning the imaging of structural details at various depths within rat brain tissue to better understand the loss of resolution and contrast due in large part to light scattering. A target was imaged though various thicknesses of tissue; the normalized slope of transition between light and dark regions of the images was used as an effective resolution index (ERI=1 for non-scattering cases). The ERI improves dramatically as the wavelength is increased: 0.03 at 600nm, 0.3 at 850nm for a 270 μm-thick hippocampus slice. A comparable change was noted for a 270 μm-thick cortex slice (ERI = 0.06 at 600nm; 0.46 at 850nm). For a fixed wavelength, ERI decreases with thickness for hippocampus slices: from 0.67 at 220μm to 0.31 at 250μm and to 0.24 at 300μm (850nm illumination). Image contrast (defined as the ratio of the pixel value difference of light and dark regions to their average standard deviation) improves with longer wavelength: from 0.9 at 600nm to 9.5 at 850nm (270 μm-thick cortex slice); from 0.9 at 600nm to 4.6 at 850nm (270 μm-thick hippocampus slice). Despite regional differences in the transparency of brain at different loci, images were degraded less by scattering at longer wavelengths, arguing strongly for the use of near-IR wavelengths for microscopic imaging either with transmitted light or fluorescent emission for exploring deeper biological structures.

In the past few decades studies on the brain have been revolutionized by introducing advanced tools like x-ray computerized tomography (CT), positron emission tomography (PET), and magnetic resonance imaging (MRI). These provide not only three-dimensional (3-D) images of brain structure, but also valuable information on their dynamic activities for understanding signal transduction. For example, human brain mapping, which depicts the human brain regions that are activated when performing a specific task, has been made possible with a functional-MRI (Ellermann, J. et al. 1994), allowing further investigation of brain functions. However, these methods are either limited by the resolution and/or by radiation damage and by the length of time required to obtain a suitable image, which present obstacles to acquiring suitable images of structural details and subtle ion variations.

3-D optical microscopy, which has high time and spatial resolution and a non-invasive nature, can avoid these difficulties and make essential contributions to studies of the brain. The capabilities of optical methods have been greatly increased with the recent advances of 3-D fluorescence microscopy and new molecular probes. 3-D fluorescence microscopy, including confocal laser scanning microscopy (CLSM) and two-photon laser scanning microscopy (TPLSM), provides better time and spatial resolution than CT, PET, and MRI, and is capable of detecting less invasively small variations in concentrations or movements of molecules and ions in cells. With micro-injection and other loading techniques such as micro-iontophoresis, it becomes possible to explore dynamic mechanisms of biological systems with minimal damage. For example, increases in neural activity-dependent calcium ion concentration in astrocytes in brain slices was observed by using a confocal microscope (Dani, J.W. et al. 1992). The morphology of the microcirculation in the neocortex of the brain has been successfully acquired with confocal microscopy up to 250μm below the surface (Dirnagl, U. et al. 1992).

Recent developments in indicator dye and imaging techniques have resulted in an ever increasing interest in imaging cells and cellular processes within intact tissues.

Biological structures near a natural interface such as the surface of the brain, may not have the same functional capabilities as those deeper in the tissue. And if the tissue is cut to expose the deeper layers, the exposed region may no longer behave as it does in its normal environment. Therefore, it is essential to develop non-invasive imaging techniques in order to explore brain activities. To study dynamic mechanisms within the body of living tissue, it is desirable to image deeply enough into the tissue to be sure we are observing typical functional behavior. However, optical imaging becomes increasingly difficult for observations deep within tissue, and removing the surface layers surgically may introduce serious artifacts. For example, the cut tissue surfaces of developing CNS tissue contain an abnormal cellular arrangement which might lead to problematic conclusions vis à vis the intact brain (Damask, A.C. et al. 1984). When imaging deep within brain tissue with currently available fluorochrome, it has proved almost impossible to acquire useful optical images beyond 50-75μm beneath the surface except with the relatively slow image acquisition rates of confocal microscopy (Terasaki, M.et al. 1995).

Deep imaging within tissue (>50 μm) can suffer from several factors, including spherical aberration, absorption and scattering of light by the tissue components. Spherical aberration can be minimized by using water immersion objectives with low numerical aperture (NA) and no coverslip; thus reducing the refractive index mismatch (Hell, S. 1993). The optical signal decay caused by light absorption of a living tissue was found to be less severe than the decay due to light scattering (Cheong, W.F. 1990). Therefore, we chose to investigate this scattering problem so as to provide a useful background for future research on the brain. We explored image degradation in two regions of the rat brain: the rat hippocampus and the cortex. Hippocampus and cortex were chosen because their crucial roles in brain function have made them the major focus of experimental neuroscience. Hippocampus is a structure thought to be essential for formation of memory and its neurons exhibit a form of synaptic plasticity called long-term potentiation, or LTP

(Kennedy, M.B. 1989). Cortex contains a complex layered structure involved in signal processing and is responsible for most primary sensory processing (Nicholls, J.G. et al. 1992).

For this chapter we investigated the role of optical wavelength on the scattering effects when imaging at a range of depths within brain tissue. Particle scattering theory indicates that scattering properties of most materials are heavily wavelength-dependent. We have designed an imaging system for studying the resolution and contrast as a function of wavelength and brain slice thickness. Since most fluorescent probes are within the green-to-red emission spectral range, we focused our investigation on the wavelength range from green to near-IR. This will provide a background for future development of molecular probes to advance the research on deep optical imaging of living tissue.

5.2. THEORY OF TISSUE SCATTERING

The information on the optical properties of brain tissue becomes more important with the development of the use of optical techniques in diagnostic and therapeutic medicine (Patterson, M.S. et al. 1989). Many optical properties are related to brain energy metabolism and information about them is required to calculate the light distribution within the regions of interest. For example, changes in the optical absorption coefficient can be related to blood oxygenation and tissue metabolism (Cope, M. et al. 1989; Tamura, M. et al. 1989). On the other hand, accurate calculation of the light distribution can be critical during laser surgery or photodynamic therapy.

In order to understand the resolution and contrast as a function of light wavelength and tissue thickness, one has to know how photons transport in turbid media such as brain tissue. Transport theory (Bonner, R.F. et al. 1987; Gandjbakhche, A.H. et al. 1997) states that the radiance L(r,s) of light at position r traveling in a direction of the unit vector s is decreased by absorption and scattering but is increased by light that is scattered from s' directions into the direction s. The relationship can be described as

$$s \bullet \nabla L(r,s) = -\mu_t L(r,s) + \mu_s \int_{4\pi} p(s,s')L(r,s')d\omega'$$

where μ_t is the total attenuation coefficient (μa+μs), μa is the absorption coefficient, μs is the scattering coefficient, $d\omega'$ is the differential solid angle in the direction s' and $p(s,s')$ is the phase function, which describes the angular distribution for a single scattering event and is usually assumed to be a function only of the angle between s and s'. $p(s,s')$ can be treated as the probability density function for scattering from direction s' to direction s if the integral of the phase function is normalized.

$$\int_{4\pi} p(s,s')d\omega' = 1$$

The radiative transport equation, in general, does not have an analytical solution and is usually solved by Monte-Carlo simulation (Graaff, R. et al. 1993). However, an approximate solution can be obtained if scattering dominates absorption (Gandjbakhche, A.H. 1992). The radiative transport equation can be then simplified as

$$\nabla^2\Phi(r) - \kappa^2\Phi(r) + Q(r) = 0$$

where $\Phi(r)$ is the radiant energy fluence rate given by integrating the radiance over 4π solid angle

$$\Phi(r) = \int_{4\pi} L(r,s)d\omega$$

and the constant κ is an approximation of the actual measured effective attenuation coefficient μ when absorption is dominated by scattering

$$\kappa^2 = 3\mu_s[\mu_a + \mu_s(1-g)]$$

The source term *Q(r)* is generated by scattering of collimated normal irradiation (Schmitt, J.M. 1990)

$$Q(r) = -3\mu_s[\mu_a + \mu_s(1-g) + (\mu_s + \mu_a)g] \bullet (1 - r_s)F(r)\exp[-(\mu_s + \mu_a)z]$$

where F(r) is the irradiance $(w \bullet m^{-2})$.

The scatterers in brain tissue, which can be treated as scattering centers in liquid, undergo Brownian motion and create optical inhomogeneity in imaging. To understand the role that wavelength plays in this scattering problem, one can substitute the concentration fluctuation into the Rayleigh's formula to obtain an approximated solution

$$\frac{I_s}{I_i} = \frac{4\pi^2 n^2 (\delta V)(\partial n / \partial C)_{t,v}^2 \overline{(\partial C)^2}}{\lambda^4 R^2}$$

where *n* is refractive index; *C* is the solution concentration, and *R* is the radius of scatterers.

Resolution, an important measure of image quality, is defined as the smallest distance that two objects can be distinguished without ambiguity. Ernst Abbe (1873,1884) established the most commonly used relation between objective and condenser numerical aperture (NA) on image resolution.

$$d_{\min} = \frac{\lambda}{NA_{obj} + NA_{con}}$$

where $d_{\min}$ is the minimum spacing in a periodic grating that can just be resolved; λ is the light wavelength in vacuum; and NA_{obj} and NA_{con} are the numerical aperture of the objective and condenser.

Contrast, another important measure of image quality, was usually defined as

$$Contrast\_Transfer\_Function = \frac{I_{\max} - I_{\min}}{I_{\max} + I_{\min}}$$

where $I_{\max}$ and $I_{\min}$ are the maximum and minimum intensities, respectively. However, it does not always represent the image quality well, especially when comparing images with different background intensities. In this chapter we used effective signal-to-noise ratio to represent the contrast

$$Effective\_Contrast\_Function = \frac{\overline{I_{\max}} - \overline{I_{\min}}}{(N_l + N_d)}$$

where N_l and N_d are the noise at light and dark regions, respectively. This contrast definition avoids different background intensity and provides a fair comparison.

Although resolution and contrast have been considered as if they were independent parameters, we are primarily interested in "distinguishibility" of details in the image, which is somewhat arbitrary and is related to contrast. For example, the Rayleigh criterion for bright, point objects on a black background really assumes that the minimum visible contrast is 26% (Pawley, J. 1995). Therefore, a contrast degradation due to tissue scattering may cause the degradation of resolution as usually defined, yet provide a usable image for many purposes.

Abbe's equation shows that the resolution improves with shorter wavelengths while the simple particle scattering model shows that the non-scattered light is decreased as the fourth power of wavelength. Consequently, in a scattering medium the gain in resolution due to shortening the wavelength is overpowered by the loss due to scattering.

5.3. METHODS AND MATERIALS

Although there are many fluorescent probes available at a wide wavelength range, we chose to investigate the tissue optics problem with a transmitted light microscope because it has several advantages. In fluorescence microscopy, both backscattering of the illumination light and scattering of the fluorescent signals can blur the images of regions of interest (ROI). Using a transmitted light microscope, one can focus on one path without the complication of backscattering of the tissue and the results can apply to both illumination backscattering and fluorescent scattering signals.

Another reason why transmitted light microscopy rather than fluorescence microscopy was chosen is that different fluorescent probes have various absorption cross sections, extinction coefficient quantum yield (QY), photobleaching rates and Stoke's shift. These factors affect the contrast and resolution of the image and therefore complicate the problem. For example, fluorescein iodoacetamide, a widely-used dye easy to conjugate to many thiols, has absorption and emission wavelength peaks 491 nm and 515 nm, respectively, and extinction coefficient 0.0082. Fura-2, a calcium indicator, has absorption and emission wavelength peak 370 nm and 474 nm and extinction coefficient 0.003. If we illuminate these two dyes at their absorption wavelength peak (120 nm difference), the emission difference depends not only on scattering but also on the emission wavelength difference of 41 nm and the 200% extinction coefficient difference.

The fluorescent emission intensities for different fluorochrome vary considerably even with exactly the same wavelength and intensity of illumination. Therefore, the differences between the images acquired with these probes were partially due to characteristics of the probes such as the non-scattering factors. It is, therefore, difficult to make a fair comparison of images acquired at various wavelengths with fluorescence microscopy.

Since we wished to study the effect of light scattering by the tissue as a function of only two parameters, wavelength and tissue thickness, we used an experimental setup in which we could examine a target transilluminated with monochromatic light through various thicknesses of biological tissue. The monochromatic output from a monochromator (Oriel, 77250) illuminated by a quartz tungsten lamp was directed to the stage carrying the specimen by a fiber bundle. This monochromatic beam was reflected through the target by means of a prism (See Fig. 5.1). A diffuser between the prism and the target was used to make the illumination more homogeneous over the field. Gratings of known spacing were used as targets. The image of a target was focused by an Olympus 20x (NA 0.4) objective on an "aus-Jena" microscope, which in turn focused the image of the target onto a Hamamatsu 4880 CCD camera. The vertical movement of the microscope stage was measured by means of a Mitutoya micrometer.

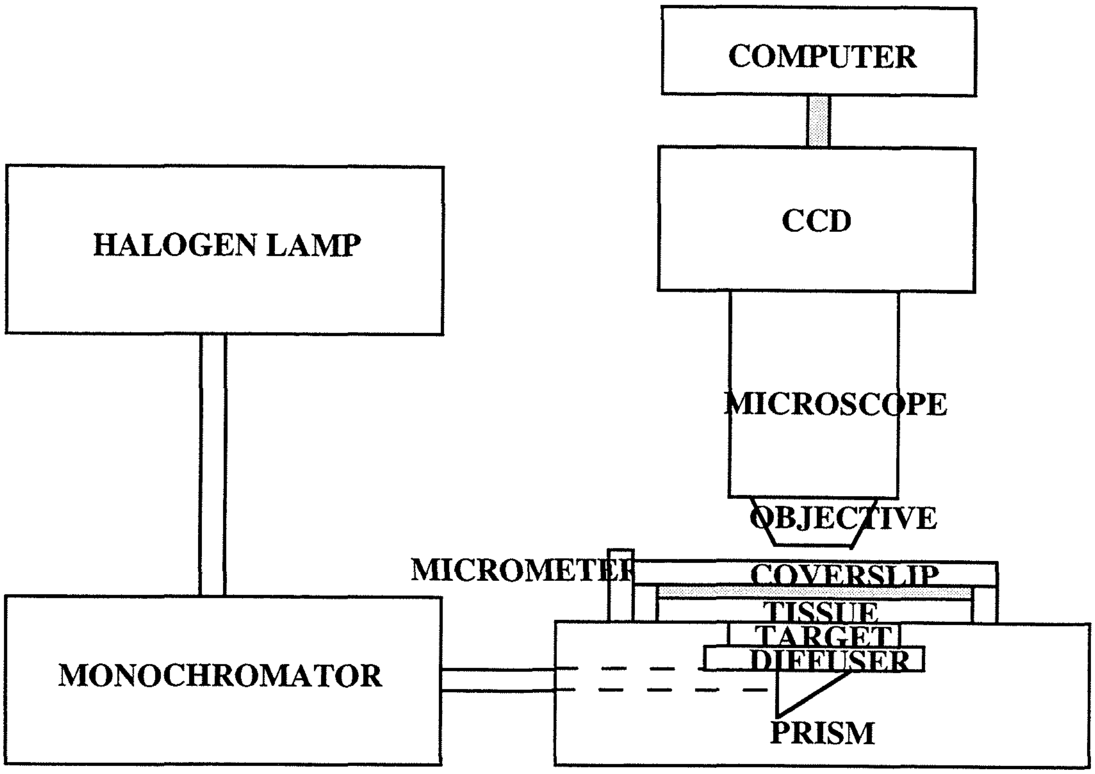

Fig. 5.1 The schematic figure of the setup of image degradation experiment.

The sections of hippocampal and cortical tissue were freshly cut from 45 day-old rats using established procedures (Kang, H. et al. 1996) and placed in hippocampus ringer solution before observation.

The wavelength of illumination light was varied from 600 nm to 850 nm at 50 nm interval using the monochromator. Target images were made at each wavelength with experimentally determined best focus. To prevent the slices from compressing under a coverslip, holes were drilled in a coverslip and the slices immersed with hippocampal ringer solution within the hole (Fig. 5.1). By successively imaging the graphite powder dusted on the top of the slice and the target on the bottom, the apparent thickness of the slice was measured with the on-stage Mitutoyo micrometer. The actual thicknesses of the slices were obtained by taking the product of the apparent thickness and the approximate refractive index 1.4.

For each data set, the same regions of interest were chosen for each series of wavelength to ensure that, for a given sample, the wavelength was the only parameter being changed. After a set of measurements at different wavelengths, the thickness of the tissue was again measured to ensure that it had not shrunk or swollen due to osmotic pressure.

In analyzing the data, a low-pass filter in the Metamorph 2.0 software package was first used to process the images to eliminate the high frequency noise. The effective contrast was then evaluated by taking the ratio of the average intensity difference between the light and dark regions in the image to the average of the standard deviation of the intensity in both regions, corrected for the noise associated with photon counting and the imaging instrument without tissue. These had been evaluated at different pixel values by changing the CCD exposure time without a specimen in the system.

The slope of the image profile was used as a measure of the ERI. For this we used the NIH image software 1.6. The profile within a rectangular area (20 pixels x 200 pixels) was obtained, yielding the average intensity of 20 pixels and spans of 200 pixels. Slopes were measured by taking two points with the center in the mid-point with 3-4 pixels separation. Nine slopes were taken for each image to obtain the statistics of the slopes. The slopes were then divided by the average pixel value. All the experimental data were divided by the normalized non-scattered slope (0.1) to get the effective resolution indices (ERI). The statistics, including the average and standard deviation, were calculated with Excel 5.0 software and plotted with Cricket Graph III v1.01.

5.4 MEASUREMENT OF IMAGE DEGRADATION

EFFECTIVE RESOLUTION INDEX

Fig. 5.2 shows the image quality as a function of wavelength of illuminating light. Fig. 5.3 shows the image quality at various thicknesses and brain regions (rat hippocampus and cortex). The longer wavelengths of illumination consistently improved image resolution (Tab. 5.1). The ERIs improved monotonically from 0.09 at 600 nm and to 0.67 at 850 nm for a 220 µm-thick hippocampus slice; ERIs improved from 0.05 at 650 nm to 0.16 at 750 nm and to 0.24 at 850 nm for a 300 µm-thick hippocampus tissue; however, the target image resolution at 600 nm, for a 300 µm-thick hippocampal slice, is too low to obtain an ERI. At the maximum wavelength of 850 nm, ERIs become progressively lower with increased tissue thickness: from 0.67 at 220 µm to 0.31 at 250 µm and to 0.24 at 300 µm. Note that all the ERIs were obtained by dividing by the non-scattering slope; therefore, ERI=1 represents the image resolution without tissue. Wavelength change showed that the image ERI at 600 nm illumination, for a 220-µm-thick slice, suffered from 90 percent degradation while the resolution at 850 nm suffered from only one-third degradation. At the same 850 nm illumination, the resolution suffered from one-third degradation at 220-µm to 70 percent at 250 µm and to three-quarter at 300 µm.

Fig. 5.2 The images of the target at different wavelengths (A) 600 nm (B) 650 nm (C) 700 nm (D) 750 nm (E) 800 nm (F) 850 nm. The tissue on the target is a 270 µm hippocampal slide. The outline boxes are sample regions for (1) slope measurements for ERI (2) contrast measurements for ECF.

Fig. 5.2 The images of the target at various wavelengths

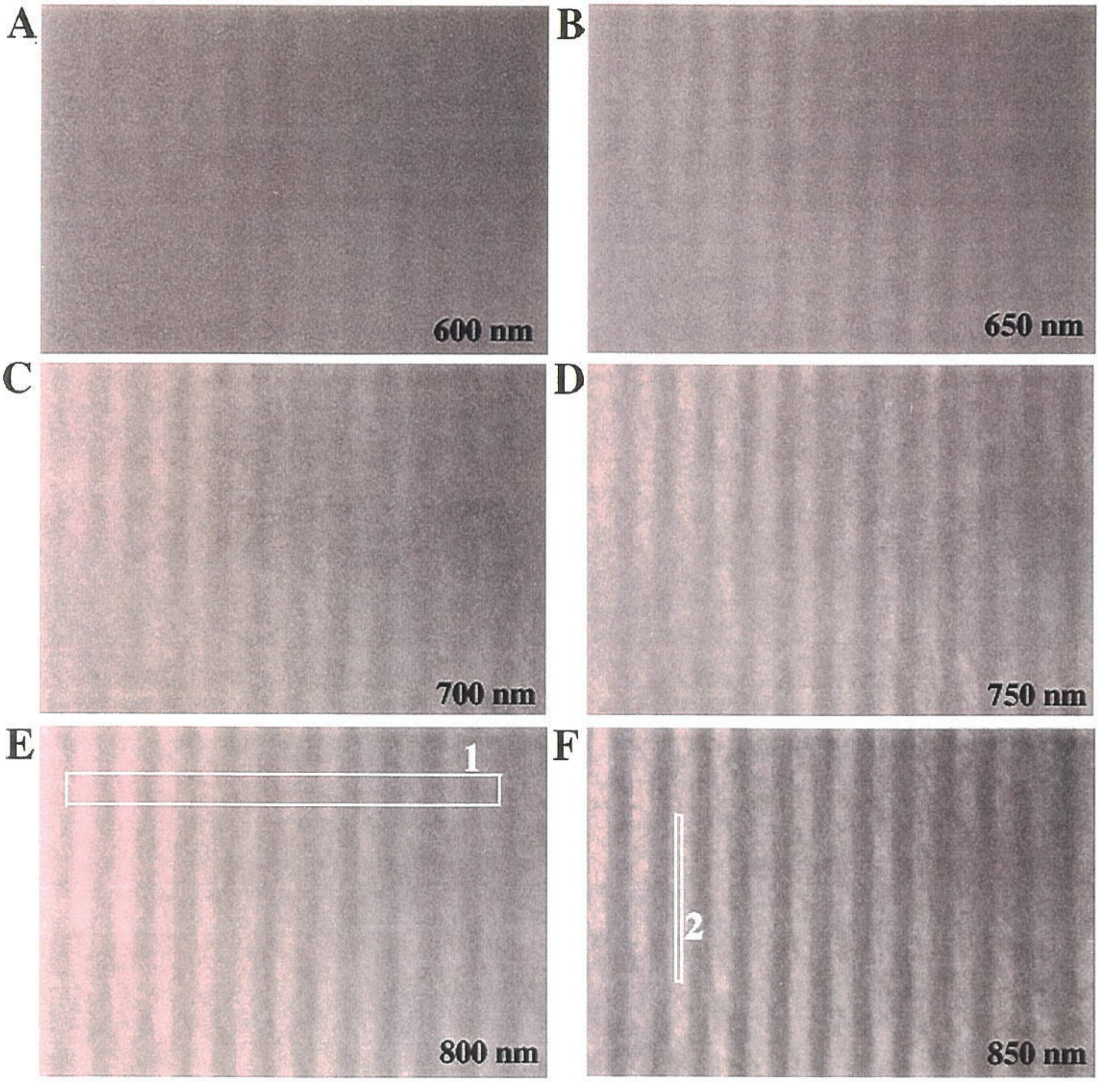

Compared to hippocampus tissue, cortex is more transparent throughout this wavelength range and has higher ERI, allowing us to explore at deeper levels of the cortex tissue. For a 270 μm slice at 850 nm, the image ERI suffered from 70 percent degradation for a hippocampus slice while it had only 50 percent loss for a cortex slice (Tab. 2). For a 370 μm-thick slice of cortex tissue, ERIs improve from 0.03 at 600 nm to 0.16 at 700 nm and to 0.21 at 850 nm. Hippocampus tissue with a similar thickness is almost opaque and the target lines can hardly be distinguished.

Fig. 5.3 The images of the target at different tissue thickness. (A) no tissue (B) 220 μm hippocampal slice (C) 250 μm hippocampal slice (D) 270 μm hippocampal slice (E) 360 μm cortex slice (F) 370 μm cortex slice. The wavelength used for obtaining the images is 750 nm.

Fig. 5.3 The images of the target at various tissue thickness

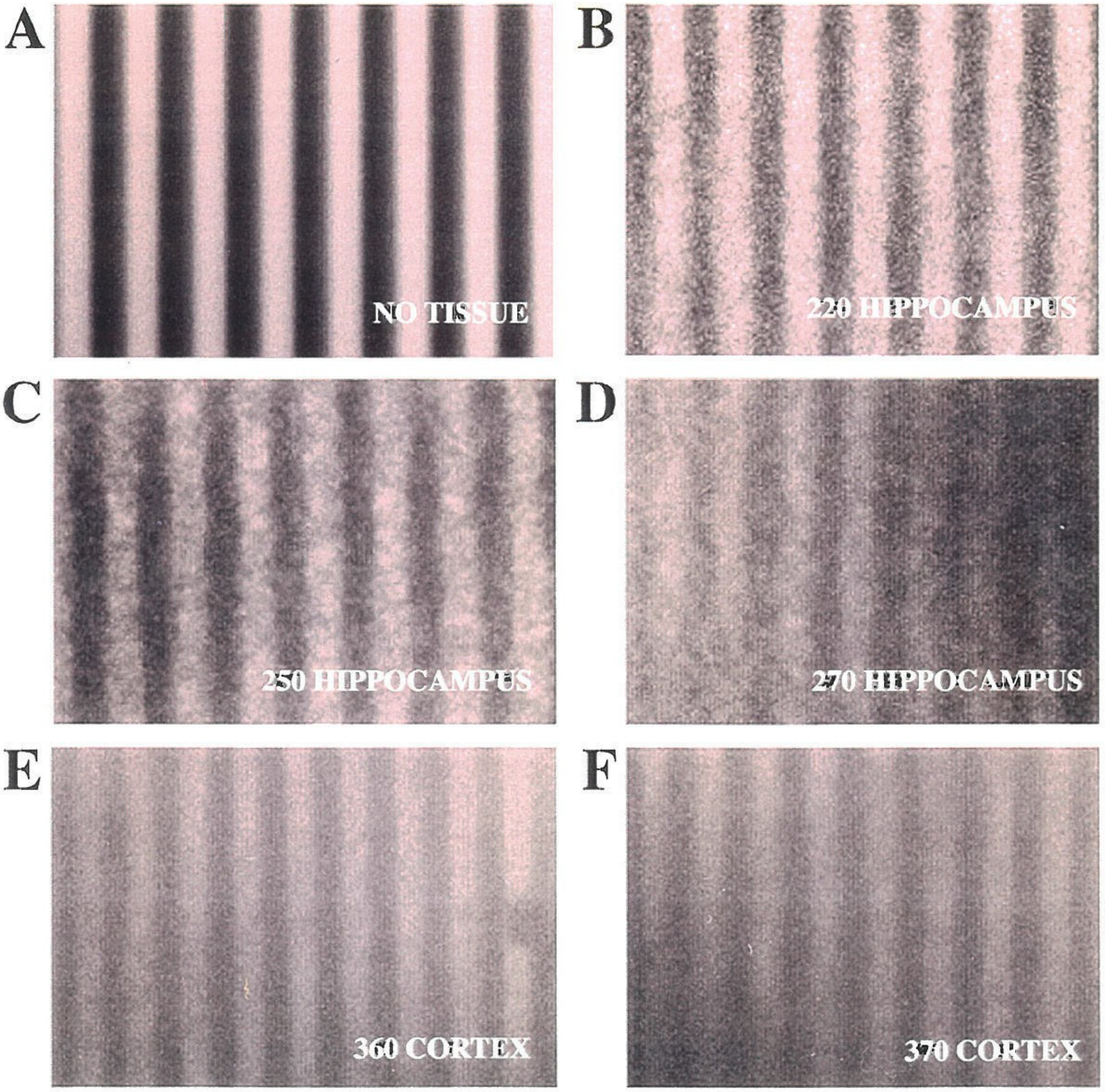

Hippocampus

	slice thickness				
wavelength	220μm	230μm	250μm	270μm	300μm
600 nm	0.09	0.14	0.08	0.03	n/a
650 nm	0.28	0.26	0.10	0.06	0.05
700 nm	0.39	0.35	0.19	0.12	0.12
750 nm	0.49	0.41	0.19	0.16	0.16
800 nm	0.58	0.53	0.25	0.24	0.19
850 nm	0.67	0.58	0.31	0.30	0.24

Tab. 5.1 Normalized effective resolution index (ERI) at different wavelengths for hippocampus slices with various thickness (ERI =1 for non-scattering cases).

Cortex

	slice thickness				
wavelength	250μm	270μm	290 μm	360μm	370μm
600 nm	0.06	0.06	0.06	0.06	0.03
650 nm	0.19	0.11	0.10	0.11	0.08
700 nm	0.34	0.20	0.12	0.14	0.16
750 nm	0.41	0.26	0.18	0.14	0.17
800 nm	0.48	0.40	0.34	0.21	0.18
850 nm	0.51	0.46	0.44	0.24	0.21

Tab. 5.2 Normalized effective resolution index (ERI) at different wavelengths for cortex slices with various thickness (ERI =1 for non-scattering cases).

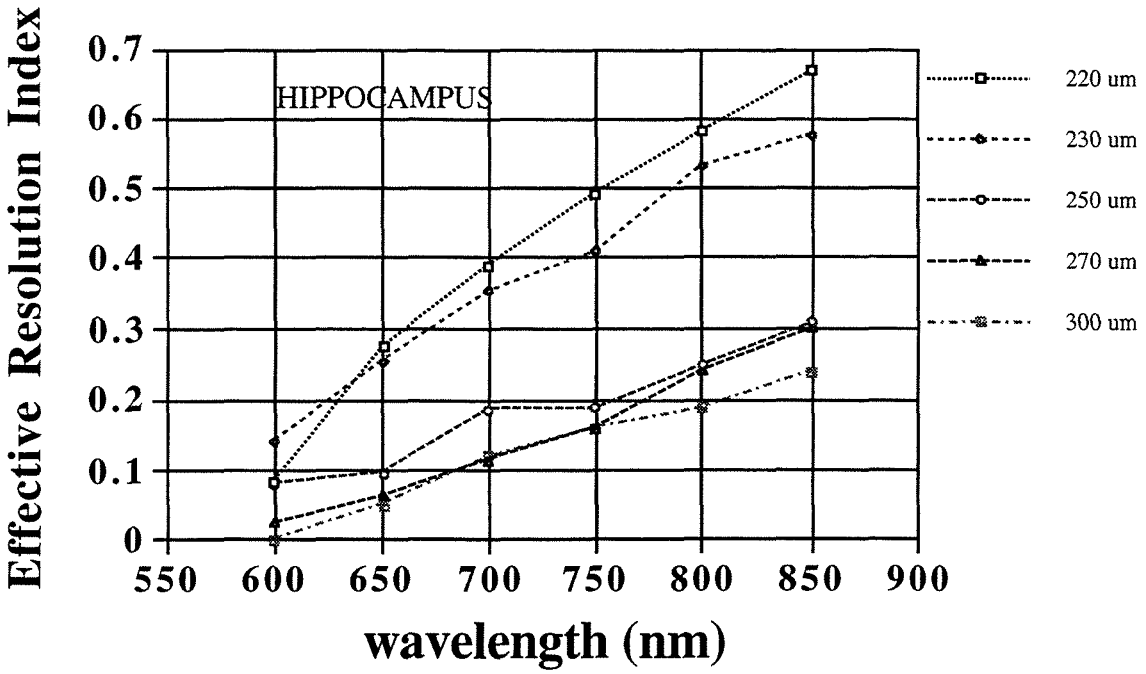

Fig. 5.4 Graph of normalized effective resolution index (ERI) at different wavelengths for hippocampus slices with various thickness (ERI =1 for non-scattering cases).

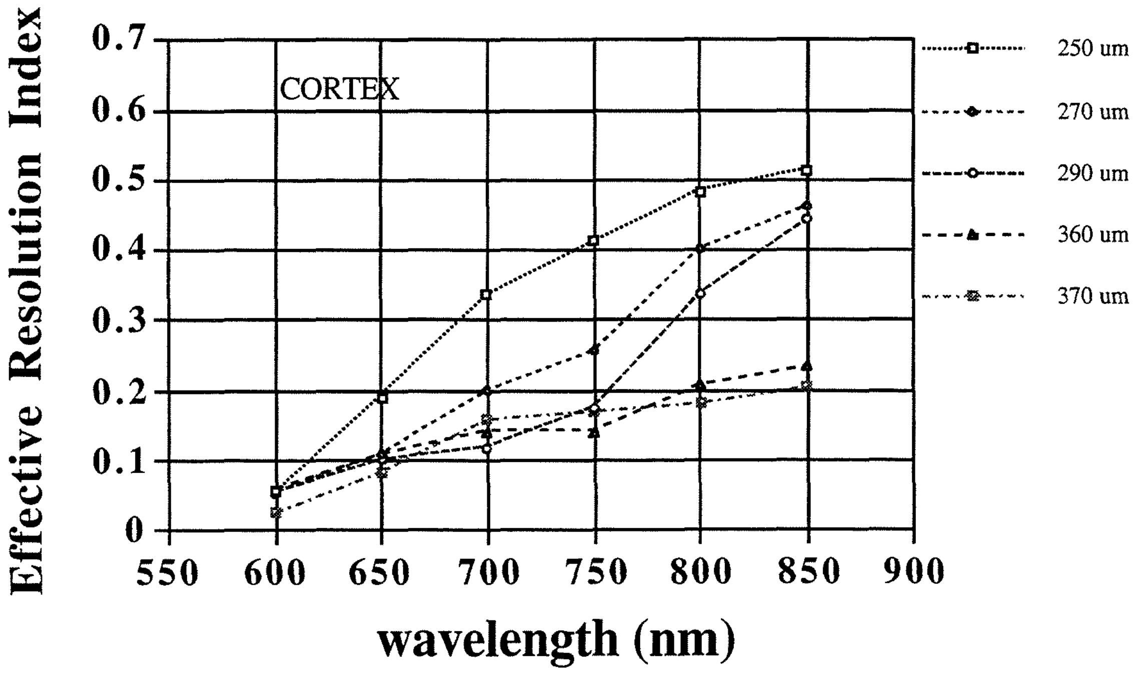

Fig. 5.5 Graph of normalized effective resolution index (ERI) at different wavelengths for cortex slices with various thickness (ERI =1 for non-scattering cases).

EFFECTIVE CONTRAST FUNCTION

The effective contrast functions (ECF) of target images also increased with illumination of longer wavelengths. For a 250 µm-thick hippocampus slice, ECFs improved from 1.45 at 600 nm to 2.38 at 700 nm and to 4.92 at 850 nm; for a 300 µm slice, ECFs improved from 0.6 at 650 nm to 1.28 at 750 nm and to 1.4 at 850 nm; however, the contrast function at 600 nm could not be obtained due to heavy scattering. For a fixed wavelength, ECFs degrade for thicker cortex slices. For example, at 850 nm illumination, ECFs degraded from 9.8 at 220 µm to 4.9 at 250 µm and to 1.4 at 300 µm.

Cortex slices are more transparent and therefore have higher ECFs. For a 250 µm-thick cortex slice, ECFs increased from 4.25 at 600 nm to 6.98 at 700 nm and to 9.32 at 850 nm; for a 370 µm slice, ECFs improved from 0.31 at 600 nm to 0.86 at 700 nm and to 1.14 at 850 nm. For all these data sets, ECFs increased monotonically with wavelength. For cortex slices illuminated at 800 nm, ECFs decreased from 8.73 at 250 µm to 3.65 at 290 µm and to 1.05 at 370 µm.

Image contrast and resolution, in general, degrade with greater tissue thickness, although there are small deviations from this degradation trend. These small deviations are believed to be artifacts brought by local structure and damaged surfaces due to cutting and should be greatly reduced if more measurements over different regions of hippocampus and cortex slices were taken.

Hippocampus

	slice thickness				
wavelength	220µm	230µm	250µm	270µm	300µm
600 nm	2.8	2.6	1.5	0.88	n/a
650 nm	4.9	3.9	2.0	1.4	0.60
700 nm	6.1	5.9	2.4	2.0	1.2
750 nm	7.8	6.5	3.0	2.8	1.3
800 nm	9.6	8.3	3.6	3.5	1.4
850 nm	9.8	8.4	4.9	4.6	1.4

Tab. 5.3 Effective contrast function at different wavelengths for hippocampus slices with various thickness.

Cortex

	slice thickness				
wavelength	250µm	270µm	290µm	360µm	370µm
600 nm	4.3	0.85	1.3	0.26	0.31
650 nm	6.2	2.4	2.4	0.61	0.35
700 nm	7.0	6.0	2.6	1.2	0.86
750 nm	7.9	7.3	2.8	1.2	0.86
800 nm	8.7	8.7	3.7	1.4	1.1
850 nm	9.3	9.5	4.4	1.5	1.1

Tab. 5.4 Effective contrast function at different wavelengths for cortex slices with various thickness.

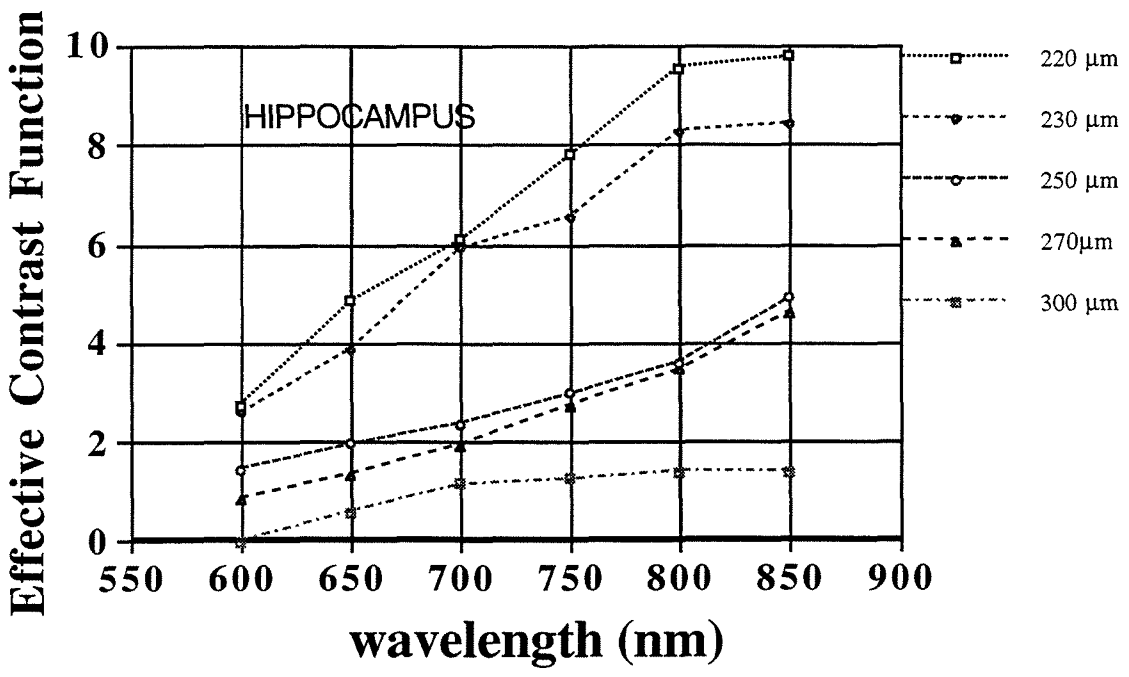

Fig. 5.6 Graph of effective contrast function at different wavelengths for hippocampus slices with various thickness.

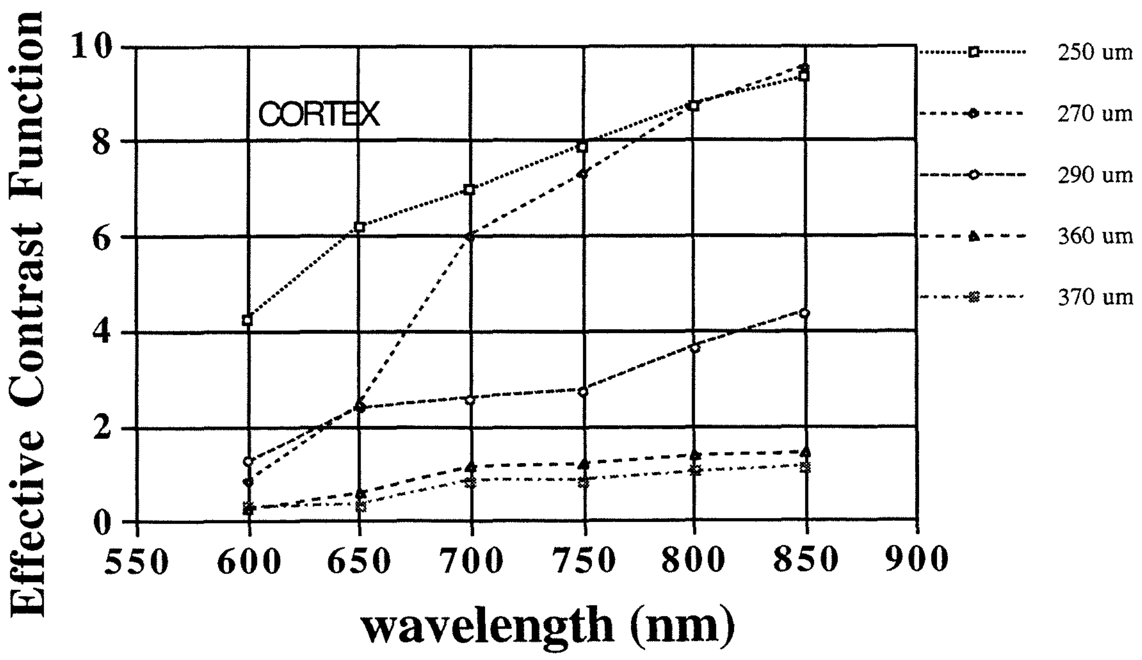

Fig. 5.7 Graph of effective contrast function at different wavelengths for cortex slices with various thickness

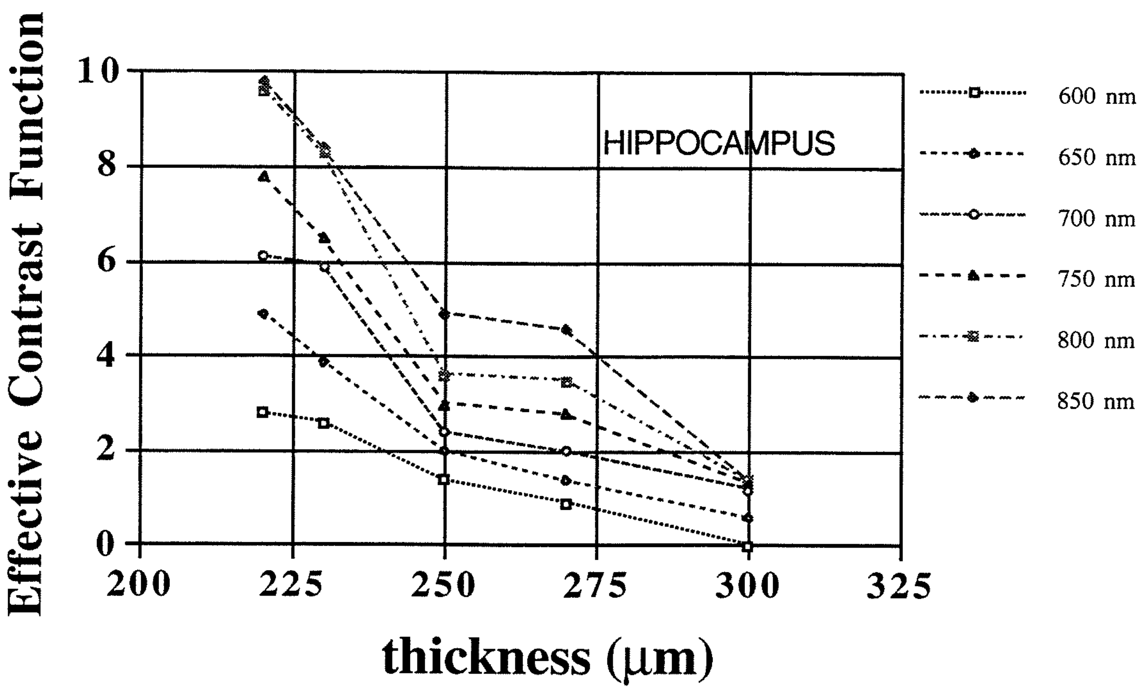

Fig. 5.8 Graph of effective contrast function as a function of thickness at various illumination wavelengths.

To investigate the effect of tissue thickness, the ECF and ERI of the hippocampus images were plotted as a function of depth from 600 to 850 nm (see Fig. 5.8 and 5.9). Both functions decrease monotonically with thickness, as expected. The ECF decreases by 85% while the ERI decreases by 65% from 220 μm to 300 μm at 850 nm. The results at other wavelengths also show that the ECF decays more than the ERI for a thicker tissue. These results imply that scattering may affect contrast more than resolution.

Moreover, to compare Rayleigh scattering theory and experimental data, logarithm values of the ECF of the hippocampus and cortex tissue were plotted as a function of logarithm values of wavelengths and fit the curves to find the slopes, which represents the dependence of ECF on wavelengths.

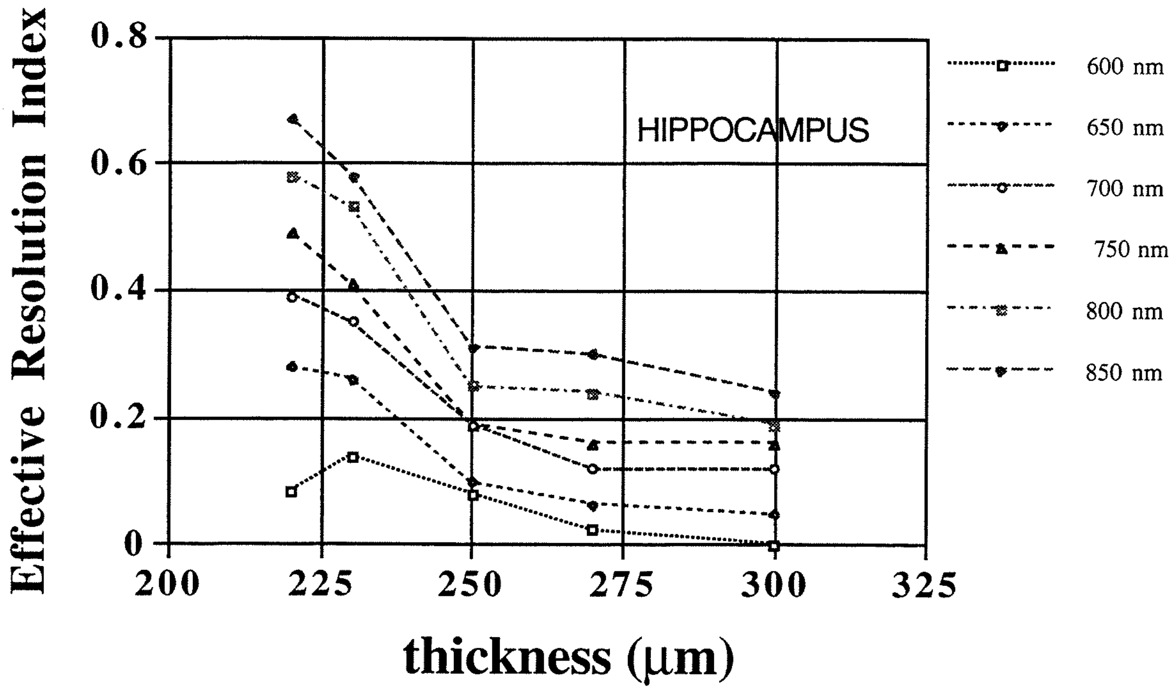

Fig. 5.9 Graph of effective resolution index as a function of thickness at various illumination wavelengths.

Fig. 5.10 and 5.11 show the results for the hippocampus and cortex, respectively. The slopes of hippocampal tissue range from 2.9 to 4.7 with an average of 3.6 while those of the cortex range from 2.1 to 6.8 with an average of 4.2. From Rayleigh scattering theory, the scattered intensity depends on the incident intensity to the fourth power. This comparison shows that the experimental data, in general, agree with Rayleigh theory. However, due to the lack of homogeneity of the hippocampal and cortex tissue, the variation of the slopes can be significant.

HIPPOCAMPUS

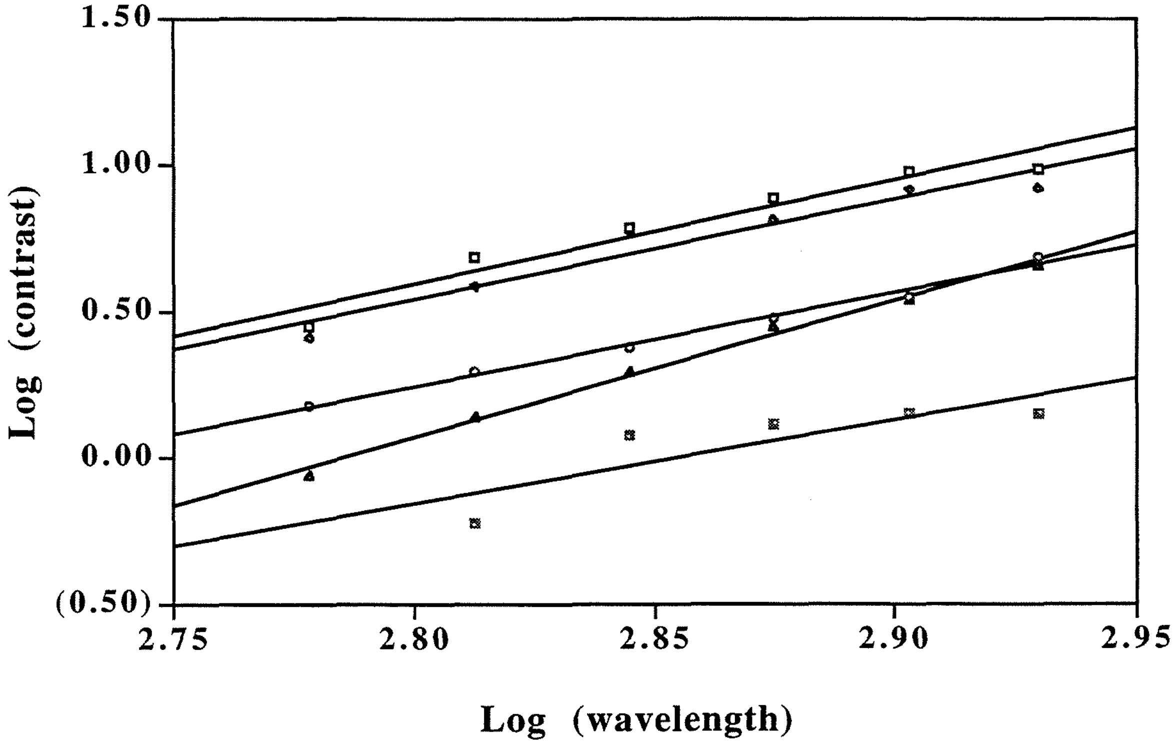

□	220 μm	$y = 3.548x - 9.339$	$r^2 = 0.936$
◆	230 μm	$y = 3.422x - 9.039$	$r^2 = 0.936$
○	250 μm	$y = 3.239x - 8.825$	$r^2 = 0.990$
▲	270 μm	$y = 4.683x - 13.039$	$r^2 = 0.994$
▨	300 μm	$y = 2.848x - 8.130$	$r^2 = 0.707$

Fig 5.10 Graph of the measured effective contrast function of hippocampal tissue. The coefficients of x indicate the power dependence of wavelengths.

CORTEX

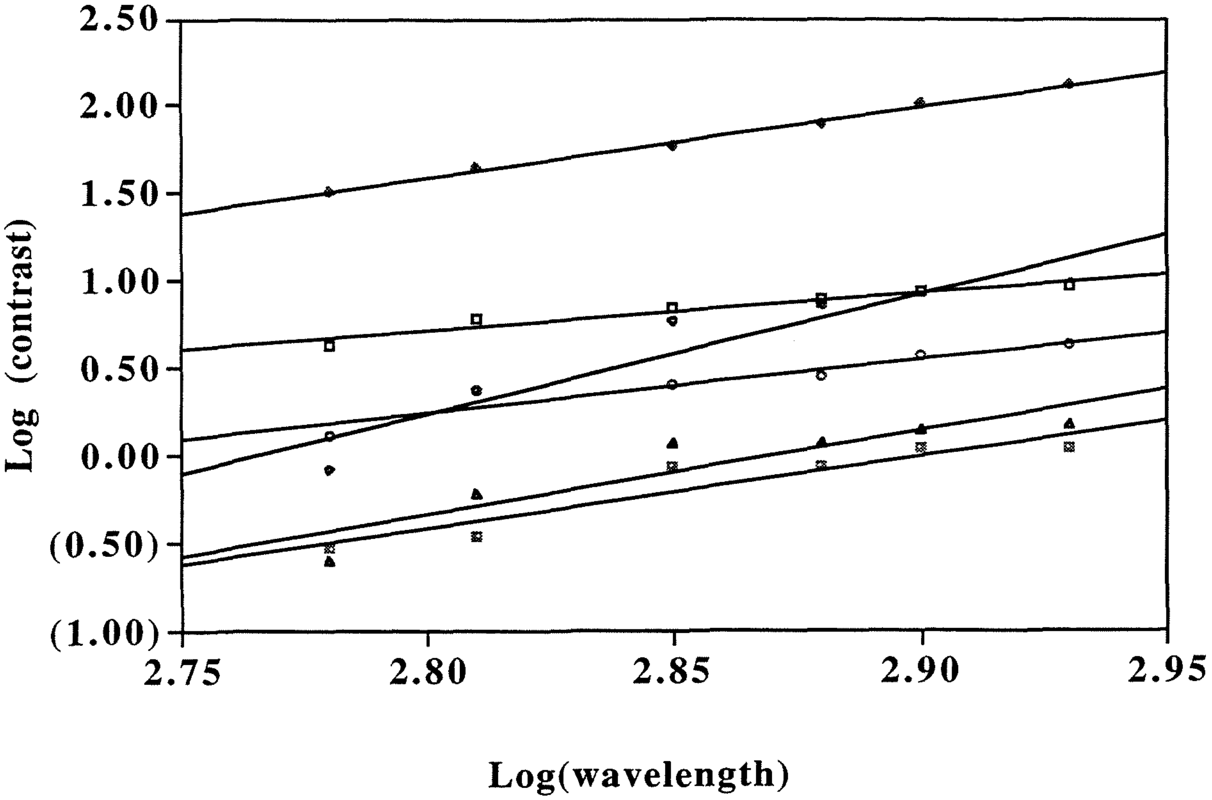

□	250 um	$y = 2.080x - 5.100$	$r^2 = 0.923$
◆	270 um	$y = 6.837x - 18.897$	$r^2 = 0.879$
○	290 um	$y = 3.067x - 8.339$	$r^2 = 0.892$
▲	360 um	$y = 4.783x - 13.724$	$r^2 = 0.833$
▨	370 um	$y = 4.136x - 11.992$	$r^2 = 0.883$
◆	theory	$y = 4.006x - 9.624$	$r^2 = 0.996$

Fig. 5.11 Comparison of the measured effective contrast function of cortex tissue and the Rayleigh scattering theory. The coefficients of x indicate the power dependence of wavelengths.

5.4. DISCUSSION

In this chapter we have shown that both the image resolution and contrast improve with illumination at longer wavelength These results reveal that imaging with long wavelengths is less affected by the scattering effects, so fluorescent probes with long emission wavelengths will be more useful for exploring deep biological structures and activities. Although fluorochrome with red or IR emission are not the most common used indicator, this study shows that near-IR fluorescent indicators have great advantage for deep tissue investigation.

The relationship between ERI and conventional definition of resolution needs further investigation, so that this study can be compared to other research of resolution of optical imaging. Besides, biological tissue is not homogeneous and usually has various structures at different regions. Because scattering effects depend not only on the sizes and types of the molecules but also the tissue structure, we need more data to get the ERI value statistics so as to relate them to the tissue structure to obtain a clearer understanding and predictive ability.

REFERENCES

Bonner, R.F., Nossal, R., Havlin, S., and Weiss, G.H., 1987, "Model for photon migration in turbid biological media," *J. Opt. Soc.Am. A* **4**:423-433

Cheong, W.F., Prahl, S.A., and Welch, A.J., 1990, "A Review of the Optical Properties of Biological Tissues," *IEEE J. Quantum Electronics*, Vol. **26** (12) 2166-2185

Cope, M., and Delpy, D.T., 1988, "System for Long-Term Measurement of Cerebral Blood and Tissue Oxygenation on Newborn Infants by Near Infrared Transillumination," *Med. Biol. Eng. Comput.* **26**: 289-294

Damask, A.C., and Swenberg, C.E., 1984, "Medical Physics - Synapse, Neuron, Brain," Vol. **3**: 232-287 Academic press, Orlando

Dani, J.W., Chernjavsky, A., and Smith, S.J., 1992, "Neuronal activity triggers calcium waves in hippocampal astrocyte netwroks," *Neuron* **8**: 429-440

Dirnagl, U., Villringer, A., and Einhaupl, K. M., 1992, "In vivo confocal scanning laser microscopy of the cerebral microcirculation," *J. Microsc.* **165**: 147-157

Ellermann, J., Garwood, M., Hendrich, K., Hinke, R., Hu, X., Kim, S., Menon, R., Merkle, H., Ogawa, S., and Ugurbil, K., 1994, "Functional Imaging of the Brain by Nuclear Magnetic Resonance," in *NMR in Physiology and Biomedicine* Robert J. Gillies Ed. 137-150 Academic press, San Diego

Graaff, R., Koelink, M.H., de Mul, F.F.M., Zijlstra, W.G., Dassel, A.C.M., and Aarnoudse, J.G., 1993, "Condense Monte Carlo simulations for the description of light transport," *Applied Optics* **32**: 426-434

Gandjbakhche, A.H., Bonner, R.F., Nossal, R., and Weiss, G.H., 1997,"Effects of multiple-passage probabilities on fluorescent signals from biological media," *Applied Optics* **36**: 4613-4619

Gandjbakhche, A.H., Bonner, R.F., and Nossal, R., 1992, "Scaling relationships for anisotropic random walks," *Journal of Statistical Physics* **69**:35-53

Hell, S., Reiner, G., Cremer, C., and Stelzer, E.H.K., 1993, "Aberrations in confocal fluorescence microscopy induced by mismatches in refractive index," *J. Microsc.* **169**:391-405

Kang, H., and Schuman, E.M., 1996, "A requirement for local protein-synthesis in neurotrophin-induced hippocampal synaptic plasticity," *Science* **273**:1402-1406

Kennedy, M.B. 1989, "Regulation of Synaptic Transmission in the Central Nervous System: Long-Term Potentiation," *Cell* **59**:777-787

Nicholls, J.G., Martin, A.R., Wallace, B.G., 1992, "From Neuron to Brain - A Cellular and Molecular approach to the Function of the Nervous System," 3rd Ed. Sinauer, Sunderland

Patterson M.S., Chance, B., and Wilson B.C., 1989, "Time resolved reflectance and transmittance for the non-invasive measurement of tissue optical properties," *Applied Optics* **28**:2331-2336

Pawley, J., 1995, "Fundamental Limits in Confocal Microscopy," in *Handbook of Biological Confocal Microscopy* J.B. Pawley 2nd Ed., 19-37 Plenum, New York

Schmitt, J.M., Zhou, G.X., Walker, E.C., and Wall, R.T., 1990, "Multilayer model of photon diffusion in skin," *J. Opt. Soc. Am. A* **7**:2141-2153

Tamura, M., Hazeki, O., Nioka, S., Chance, B., and Smith, D., 1989, "Simultaneous Measurements of Tissue Oxygen Concentration and Energy State by Near-Infrared and Nuclear Magnetic Resonance Spectroscopy," in *Chemoreceptors and Reflexes in Breathing*, S. Lahiri, Ed. Oxford U.P., New York

Terasaki, M., and Dailey, M.E., 1995, "Confocal Microscopy of living Cells," in *Handbook of Biological Confocal Microscopy* J.B. Pawley 2nd Ed., 327-346 Plenum, New York

CHAPTER IV

CONCLUSION

6.1 SUMMARY

The following points summarize the various aspects of two-photon laser scanning microscopy (TPLSM) discussed in my dissertation.

- TPLSM is capable of doing 3-D UV fluorescence imaging without special UV optics. Images of Drosophila chromosomes stained with DAPI were shown.

- Quantitative confirmation of two-photon excitation of our TPLSM was demonstrated. Emission intensity of TPLSM depends quadratically on excitation intensity.

- Overall fluorescence detection efficiency of our TPLSM was about 2%. Improving the quantum efficiency of the detector can increase its fluorescence collecting efficiency.

- TPLSM was shown to have less photobleaching and better penetration depth than CLSM. The photobleaching region of TPLSM was only the focal plane while that of CLSM extends to out-of-focus regions. Low NA objectives provide better penetration depths than high NA objectives.

- The field depth of TPLSM depends on the pinhole size (if any) and the NA of the objective. A small pinhole and a high NA decreases the field depth at the cost of low signal-to-noise ratio. TPLSM with a great pinhole (200 μm) provides good image quality with small field depth.

- The Point Spread Function of TPLSM is slightly larger than that of CLSM, at the same SNR. After image deconvolution, the resolution of both CLSM and TPLSM were improved by about 40%.

- Image deconvolution techniques were successfully applied to 3-D hippocampal culture cell images. Combining this iterative calculation with CLSM enables the identification of the positions of Synapsin I, CaM Kinase II and PSD-95. PSD-95 was shown to be closer to Synapsin I than CaM Kinase II.

- Images acquired at longer emission wavelengths have better penetration capability. Due to less tissue scattering, resolution and contrast of deep brain tissue images (> 200 μm) are improved from 600nm to 850 nm.

- Compared to hippocampus tissue, Cortex tissue is more transparent for 600-850 nm and therefore allows deeper tissue imaging.

6.2 OUTLOOK

The introduction of TPLSM has provided many insightful observations, especially in biological research. For example, *In vivo* dendritic calcium dynamics in neocortical pyramidal neurons was imaged with TPLSM to study the ion activity and action potential in rat primary vibrissa (Sm1) cortex (Svoboda, et al. 1997). Images of Green Fluorescent Protein (GFP) in Drosophila eyes was acquired with TPLSM to show the 3-D structure (Potter, et al. 1996). All these prove that TPLSM opens a new window to observe the dynamics and structures with much less perturbation.

Moreover, imaging with three or more photon excitation has been developed and applied to various studies. Imaging INDO-1 with three-photon excitation was done with a Ti-Sapphire laser at 885 nm to observe calcium activity (Gryczynaki et al. 1995). Four-photon-excited visible emission by serotonin solutions was observed with a Ti-Sapphire laser (Shear, et al. 1997). Although multi-photon excitation usually has a very small absorption cross section, the multi-photon images gain from the decrease of the further excitation volume and photobleaching regions.

There are still more aspects of TPLSM to be explored and more applications to investigate with TPLSM. For instance, synthesizing new fluorophores for multiphoton excitation is being developed. These fluorophores, with high two-photon absorption cross section and quantum efficiency, can substantially improve the image SNR.

Another important issue is to investigate the PSF of TPLSM in deep tissue (>200 μm), which helps understand the effects of optical aberration and scattering. These PSFs, helping TPLSM take advantage of its deep tissue imaging capability, can be applied to increase image resolution using deconvolution techniques.

Medical applications of TPLSM are also being explored. Taking advantage of its local activation property, TPLSM can be used to activate caged compounds to kill tumor cells (Wachter et al. 1998). The possibility of using a femto-pulse laser as a surgery tool was also discussed (Nathel 1998).

With the advance of technology and the decrease of its price, TPLSM will be used extensively in biological and medical research, provide exciting biological images and information, and help understand the dynamics and mechanism of the biological systems.

REFERENCES

Gryczynski, I., Szmacinski, H., and Lakowicz, J., 1995, "On the possiblilty of Calcium Imaging using INDO-1 with Three-Photon Excitation," *Photochemistry and Photobiology* **62** (4): 804-808

Nathel, 1998, "Overview of medical applications of ultrafast technology," *Proc. SPIE Photonic West* **3269** in press

Potter, S.M., Wang, C.M., Garrity, P.A., and Fraser, S.E., 1996,"Intravital imaging of green fluorescent protein using 2-photon laser-scanning microscopy," *Gene* **173** (1): 25-31

Shear, J.B., Xu, C., and Webb., W.W. , 1997, "Multiphoton-Excited Visible Emission by Serotonin Solutions," *Photochemistry and Photobiology* **65**(6): 931-936

Svoboda, K., Denk, W., Kleinfeld, D., and Tank, D.W., 1997, "In-vivo dendritic calcium dynamics in neocortical pyramidal neurons," *Nature* **385** (6612): 161-165

Wachter, E.A., Partridge, W.P.Jr., and Fisher, W.G., 1998, "Simultaneous two-photon excitation of photodynamic therapy agents," *Proc. SPIE Photonic West* **3269** in press